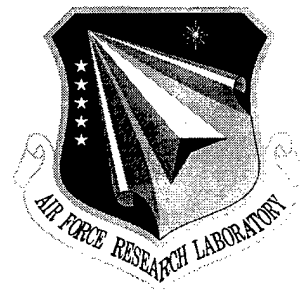


**AFRL-SN-RS-TR-1999-197**  
**Final Technical Report**  
**September 1999**



# **STAP PROCESSING MONOSTATIC AND BISTATIC MCARM DATA**

**MITRE**

**Probal Sanyal**

*APPROVED FOR PUBLIC RELEASE; DISTRIBUTION UNLIMITED.*

**AIR FORCE RESEARCH LABORATORY  
SENSORS DIRECTORATE  
ROME RESEARCH SITE  
ROME, NEW YORK**

**DTIC QUALITY INSPECTED 4**

**19991015 035**

This report has been reviewed by the Air Force Research Laboratory, Information Directorate, Public Affairs Office (IFOIPA) and is releasable to the National Technical Information Service (NTIS). At NTIS it will be releasable to the general public, including foreign nations.

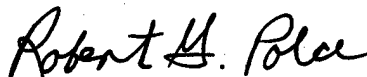
AFRL-SN-RS-TR-1999-197 has been reviewed and is approved for publication.

APPROVED:



GERARD J. GENELLO  
Project Engineer

FOR THE DIRECTOR:



ROBERT G. POLCE  
Chief, Rome Operations Office  
Sensors Directorate

If your address has changed or if you wish to be removed from the Air Force Research Laboratory Rome Research Site mailing list, or if the addressee is no longer employed by your organization, please notify AFRL/SNRT, 26 Electronic Pky, Rome, NY 13441-4514. This will assist us in maintaining a current mailing list.

Do not return copies of this report unless contractual obligations or notices on a specific document require that it be returned.

REPORT DOCUMENTATION PAGE			Form Approved OMB No. 0704-0188	
<small>Public reporting burden for this collection of information is estimated to average 1 hour per response, including the time for reviewing instructions, searching existing data sources, gathering and maintaining the data needed, and completing and reviewing the collection of information. Send comments regarding this burden estimate or any other aspect of this collection of information, including suggestions for reducing this burden, to Washington Headquarters Services, Directorate for Information Operations and Reports, 1215 Jefferson Davis Highway, Suite 1204, Arlington, VA 22202-4302, and to the Office of Management and Budget, Paperwork Reduction Project (0704-0188), Washington, DC 20503.</small>				
1. AGENCY USE ONLY (Leave blank)	2. REPORT DATE Sep 99	3. REPORT TYPE AND DATES COVERED Interim Sep 98 - May 99		
4. TITLE AND SUBTITLE  STAP PROCESSING MONOSTATIC AND BISTATIC MCARM DATA		5. FUNDING NUMBERS C - AF19628-99-C-0001 PE - 62204F PR - 762R TA - 00 WU - 00		
6. AUTHOR(S)  Probal Sanyal				
7. PERFORMING ORGANIZATION NAME(S) AND ADDRESS(ES)  MITRE Center for Air Force C2 Systems Bedford, MA		8. PERFORMING ORGANIZATION REPORT NUMBER  MTR 99B0000014		
9. SPONSORING/MONITORING AGENCY NAME(S) AND ADDRESS(ES)  AFRL/SNRT 26 Electronic Pky Rome, NY 13441-4514		10. SPONSORING/MONITORING AGENCY REPORT NUMBER  AFRL-SN-RS-TR-1999-197		
11. SUPPLEMENTARY NOTES  AFRL Project Engineer: Gerard Genello, SNRT, 315-330-3576.				
12a. DISTRIBUTION AVAILABILITY STATEMENT  Approved for public release; distribution unlimited.			12b. DISTRIBUTION CODE	
13. ABSTRACT (Maximum 200 words) Monostatic airborne radars have a problem detecting low and slow-flying airborne targets or slow-moving ground targets because of the severe ground clutter. Space-Time Adaptive Processing (STAP) algorithms have been found to be effective in suppressing the ground clutter and revealing the targets of interest. Newer surveillance systems, both airborne and space based, are likely to be bistatic, i.e., the transmitter and the receiver are to be housed in separate vehicles. Specifically, the transmitter is to be housed in an AWACS-type aircraft or a satellite and the receiver will probably be housed in a UAV. In either case, one is faced with the problem of the same ground clutter as in the monostatic case and thus there is need for bistatic clutter suppression algorithms. In 1995-1996, Air Force Research Laboratory, Rome Research Site (AFRL-RRS, formerly Rome Laboratory), collected a large amount of multi-channel, airborne radar measurement (MCARM) data, to help verify the efficacy of STAP in both monostatic and bistatic scenarios and if necessary, to develop newer algorithms for the bistatic case. This report documents the efforts by this author to apply and compare the application of STAP algorithms to several acquisitions from both monostatic and bistatic MCARM flights.				
14. SUBJECT TERMS  Monostatic, Bistatic, Space-Time Adaptive Processing (STAP), MCARM			15. NUMBER OF PAGES 156	
			16. PRICE CODE	
17. SECURITY CLASSIFICATION OF REPORT  UNCLASSIFIED	18. SECURITY CLASSIFICATION OF THIS PAGE  UNCLASSIFIED	19. SECURITY CLASSIFICATION OF ABSTRACT  UNCLASSIFIED	20. LIMITATION OF ABSTRACT  UL	

## **Abstract**

Monostatic airborne radars have a problem detecting low and slow-flying airborne targets or slow-moving ground targets because of the severe ground clutter. Space-Time Adaptive Processing (STAP) algorithms have been found to be effective in suppressing the ground clutter and revealing the targets of interest. Newer surveillance systems, both airborne and space based, are likely to be bistatic, i.e., the transmitter and the receiver are to be housed in separate vehicles. Specifically, the transmitter is to be housed in an AWACS-type aircraft or a satellite and the receiver will probably be housed in a UAV. In either case, one is faced with the problem of the same ground clutter as in the monostatic case and thus there is a need for bistatic clutter suppression algorithms.

In 1995-1996, Air Force Research Laboratory, Rome Research Site (AFRL-RRS, formerly Rome Laboratory), collected a large amount of multi-channel, airborne radar measurement (MCARM) data, to help verify the efficacy of STAP in both monostatic and bistatic scenarios and if necessary, to develop newer algorithms for the bistatic case. This report documents the efforts by this author to apply and compare the application of STAP algorithms to several acquisitions from both monostatic and bistatic MCARM flights.

**KEYWORDS:** Monostatic, Bistatic, Space-Time Adaptive Processing (STAP), MCARM

## **Acknowledgments**

The Radar Signal Processing Branch (SNRT) sponsored this effort of the Sensors Directorate (SN) of the US Air Force Research Laboratory, Rome Research Site (AFRL-RRS). The author wishes to thank Mr. G. J. Genello, Branch Chief, SNRT, for providing the necessary funding. Thanks are also due to Mr. A. S. Margulies, the MITRE Project Leader, for allowing a free hand in performing the work and also reviewing this report.

The author gratefully acknowledges the prior works of Dr. W. L. Melvin, previously with AFRL-RRS and Dr. B. Himed and Mr. V. Cavo of RADC. These persons had initiated the organization and analysis of the MCARM database at AFRL-RRS and had greatly helped the author with gaining access to the data as well as very useful pieces of software for analyzing the data.

The author has had many useful discussions with Dr. M. C. Wicks, Dr. R. W. Brown, Mr. M. O. Little, and Mr. D. Mokry, all of AFRL-RRS, regarding the MCARM data and wishes to thank them for their generous help.

# Table of Contents

Section	Page
<b>1. Introduction</b>	<b>1-1</b>
<b>2. Monostatic MCARM Data – Flight #5</b>	<b>2-1</b>
2.1 The MCARM Receiver	2-1
2.2 The Flight Path and Flight Parameters	2-1
2.3 Acquisition #5-152	2-7
2.3.1 Iso-Range and Iso-Doppler Contours	2-8
2.3.2 Clutter and MTS Returns	2-10
2.3.3 FTS and EFA Algorithms Applied to Acquisition #5-152 with Angle Index 58	2-14
2.3.4 FTS and EFA Algorithms Applied to Acquisition #5-152 with Angle Index 90	2-16
2.3.5 JDL-mxn Algorithms Applied to Acquisition #5-152, Angle Index 58	2-20
2.4 Acquisition #5-575 – Looking for the Sabreliner	2-24
<b>3. Bistatic MCARM Data – Flight #9</b>	<b>3-1</b>
3.1 The Tethered Aerostat Radar System (TARS)	3-1
3.2 The Flight Path and Flight Parameters	3-1
3.3 Acquisition #9-110	3-5
3.3.1 Iso-Bistatic Range and Iso-Bistatic Doppler Contours	3-5
3.3.2 Clutter-Free MTS Returns in Acquisition #9-110	3-7
3.3.3 MTS Signal Plus Clutter in Acquisition #9-110	3-10
3.3.4 FTS Algorithm Applied to the Bistatic Acquisition #9-110	3-12
3.3.5 JDL mxn Algorithm Applied to the Bistatic Acquisition #9-110	3-14
3.4 Acquisition #9-133	3-20
3.5 Pseudomonostatic Acquisitions	3-22
3.5.1 Acquisitions 172, 173, 177-182	3-22
3.5.2 Adaptive Processing of Pseudomonostatic Acquisition #9-172	3-24
3.5.3 Adaptive Processing of Pseudomonostatic Acquisition #9-180	3-26
3.5.4 Adaptive Processing of Pseudomonostatic Acquisition #9-182	3-32
3.6 Wide-Bistatic-Angle Acquisitions	3-35
<b>4. Summary</b>	<b>4-1</b>
<b>List of References</b>	<b>RE-1</b>
<b>Appendix A. STAP Algorithms</b>	<b>A-1</b>
A.1 The FTS Algorithm	A-1

A.2 The EFA Algorithm	A-2
A.3 TheJDL mxn Algorithm	A-4
<b>Distribution List</b>	<b>DI-1</b>

## List of Figures

Figure	Page
2-1. The Northrop-Grumman BAC 1-11 Equipped with the MCARM Phased Array Antenna	2-1
2-2. Flight Path of Monostatic Flight #5 Overlaid on the DELMARVA Terrain	2-2
2-3. Part of the Flight Path of the BAC 1-11 on Monostatic Flight #5	2-3
2-4. Flight Parameters on Flight #5, Acquisitions 90 to 230	2-5
2-5. The Iso-Range Contours at Acquisition #5-152	2-9
2-6. The Iso-Doppler Contours at Acquisition #5-152	2-10
2-7. RDI Plot on Acquisition #5-152	2-11
2-8. MCARM Transmitter and MTS Pulse Width	2-12
2-9. Angle-Doppler Plot on Acquisition #5-152	2-13
2-10. Unadapted RDI, Acquisition #5-152, Angle Index 58	2-14
2-11. FTS Algorithms Applied to Acquisition #5-152, Angle Index 58	2-15
2-12. EFA Algorithms Applied to Acquisition #5-152, Angle Index 58	2-16
2-13. Unadapted RDI, Acquisition #5-152, Angle Index 90	2-17
2-14. FTS Algorithms Applied to Acquisition #5-152, Angle Index 90, Channels: 22; Support: (-100,+100); Guard Cells: $\pm 3$	2-17



2-15. FTS Algorithms Applied to Acquisition #5-152, Angle Index 90, Channels: 11; Support: (-28,+18); Guard Cells: $\pm 3$	2-18
2-16. FTS Algorithms Applied to Acquisition #5-152, Angle Index 90, Channels: 11; Support: (-11,+11)	2-18
2-17. EFA Algorithms Applied to Acquisition #5-152, Angle Index 90, Channels: 22; Support: (-99,+99); Guard Cells: $\pm 3$	2-20
2-18. JDL <sub>mx1</sub> Algorithms Applied to Acquisition #5-152, Angle Index 58; Channels: 22; Support Cells: (-20, +10); Guard Cells: $\pm 3$	2-21
2-19. JDL <sub>1xn</sub> Algorithms Applied to Acquisition #5-152, Angle Index 58; Channels: 22; Support Cells: (-20, +10); Guard Cells: $\pm 3$	2-22
2-20. JDL <sub>mxn</sub> Algorithms Applied to Acquisition #5-152, Angle Index 58; Channels: 22; Support Cells: (-20, +10); Guard Cells: $\pm 3$	2-23
2-21. JDL <sub>1x6 = (0*0)x(3*2)</sub> Algorithm Applied to Acquisition #5-152, Angle Index 58; Channels: 22; Support Cells: (-20, +10); Guard Cells: $\pm 3$	2-24
2-22. Flight Paths of BAC 1-11 and Sabreliner on Flight #5	2-24
2-23. Acquisition #5-575 – Looking for the Sabreliner	2-26
2-24. Angle-Doppler Plot, Range Cell #320, Acquisition #5-575	2-27
2-25. JDL-3x3 Algorithm Applied to Acquisition #5-575, Angle Index 70; Channels: 22; Support Cells: (-10, +10); Guard Cells: $\pm 3$	2-27
3-1. The TARS Aerostat Carrying the Bistatic Transmitter	3-1
3-2. Part of the Flight Path of Bistatic Flight #9	3-2
3-3. Flight Parameters on Flight #9, Acquisitions 50-230	3-3

3-4. MTS-Related Parameters on Flight #9	3-4
3-5. Iso-Bistatic Range and Iso-Bistatic Doppler Contours, Acquisition #9-110	3-7
3-6. The MTS Signal on Acquisition #9-110	3-8
3-7. RDI Plot, Acquisition #9-110	3-11
3-8. 3D RDI and Cell 33, Acquisition #9-110	3-12
3-9. Angle-Doppler Plot, Acquisition #9-110, Cell #31	3-12
3-10. FTS-Adapted RDI and Cell #33, Acquisition #9-110 (Channels: 11; Support Cells: $\pm 11$ ; Guard Cells: $\pm 3$ )	3-13
3-11. JDL 3x3 -Adapted RDI, Acquisition #9-110 (Channels: 22; Support Cells: -20,+10; Guard Cells: $\pm 3$ )	3-15
3-12. JDL mx1 -Adapted RDI, Acquisition #9-110 (Channels: 22; Support Cells: -20,+10; Guard Cells: $\pm 3$ )	3-16
3-13. JDL mx1 -Adapted Range Cell #33, Acquisition #9-110 (Channels: 22; Support Cells: -20,+10; Guard Cells: $\pm 3$ )	3-18
3-14. JDL 1xn -Adapted RDI, Acquisition #9-110 (Channels: 22; Support Cells: -20,+10; Guard Cells: $\pm 3$ )	3-19
3-15. Acquisition #9-133	3-21
3-16. Unadapted RDI Plots for Several Pseudomonostatic Acquisitions	3-23
3-17. Signal Versus Pulse Number for the same Pseudomonostatic Acquisitions as in Figure 3-16	3-23

3-18. JDL 3x3 -Adapted RDI, Acquisition #9-172 (Channels: 22; Support Cells: -20,+10; Guard Cells: $\pm 3$ )	3-25
3-19. FTS -Adapted RDI, Acquisition #9-172 (Channels: 11; Support Cells: -11,+11; Guard Cells: $\pm 3$ )	3-26
3-20. Pseudomonostatic Acquisition #9-180	3-28
3-21. RDI at Various Angle Indexes, Acquisition #9-180	3-29
3-22. STAP-Processing Acquisition #9-180 with Varying CSRs	3-31
3-23. RDI of Pseudomonostatic Acquisition #9-182	3-32
3-24. Signal Strength Versus Pulse Number in Pseudomonostatic Acquisition #9-182	3-33
3-25. JDL mx1 -Adapted RDI, Acquisition #9-182 (Channels: 22; Support Cells: 20,+10; Guard Cells: $\pm 3$ )	3-33
3-26. JDL 1xn -Adapted RDI, Acquisition #9-182 (Channels: 22; Support Cells: -20,+10; Guard Cells: $\pm 3$ )	3-34
3-27. Comparing JDL mx1 and JDL mx3 -Adapted RDI, Acquisition #9-182 (Channels: 22; Support Cells: -20,+10; Guard Cells: $\pm 3$ )	3-34
3-28. RDI, Wide-Bistatic Angle Acquisition #92	3-35
3-29. RDI, Wide-Bistatic Angle Acquisition #93 (Angle Index 80)	3-36
3-30. Comparing Signal Strength Versus Pulse Number in Acquisitions 92, 93 and 182	3-37

## List of Tables

<b>Table</b>	<b>Page</b>
2-1. Flight and Data Collection Parameters on Acquisition #5-152	2-8
2-2. MTS Parameters on Acquisition #5-152	2-8
2-3. Twelve Highest Peaks in Figure 2-6d	2-12
2-4. Target Parameters on Acquisition #5-575	2-25
3-1. Flight and Data Collection Parameters on Acquisition #9-110	3-5
3-2. MTS Parameters on Acquisition #9-110	3-6
3-3. The MTS Tones – Design Characteristics	3-9
3-4. Observed MTS Tones on Acquisition #9-110	3-10
3-5. Observed MTS Tones on Acquisition #9-110 (Normalized to the Central Peak)	3-10
3-6. Flight and Data Collection Parameters on Acquisition #9-180	3-27
3-7. MTS Parameters on Acquisition #9-180	3-27

## Section 1

# Introduction

A major problem faced by airborne radars when looking for low and slow-flying, low-cross-section, airborne targets and slow-moving ground targets is the severe ground clutter and possible jamming that mask these target returns. This is true in the case of both monostatic and bistatic airborne radars, and will almost certainly be true when the surveillance systems are expanded into space. With multi-channel antenna and receiver systems, it is possible to suppress the clutter to a large degree by adaptively processing the data. The Space-Time Adaptive Processing (STAP) algorithms are a class of adaptive algorithms that make use of the 'space' dimension and the 'time' dimension as their degrees of freedom to cancel the clutter while minimally affecting the desired signal. The 'space' dimension is represented by the multiple antenna elements and the associated receivers and the 'time' dimension is represented by the multiple pulses.

In 1995-96, the Air Force Research Laboratory, Rome Research Site (AFRL RRS, formerly Rome Laboratory) collected a large amount of multi-channel, airborne radar measurement (MCARM) data, in both the monostatic and bistatic modes. There are literally hundreds of coherent processing intervals (CPI) or acquisitions, with most of them containing a signal from a ground-based, stationary moving target simulator (MTS) that generated multiple tones to represent targets moving at different velocities. On one of the monostatic flights, a real target, a Sabreliner, was flown such that it was 'painted' by the MCARM radar. On some acquisitions, there are certain other targets of opportunity.

A large number of the monostatic acquisitions have been made available to the many researchers who have until now been using simulated data to verify their novel clutter suppression algorithms. The measured data has helped them to consolidate their claims for these algorithms. The bistatic data from this database has not been disseminated very widely until now.

With an unlimited access to the MCARM database, this author has made an attempt at taking a more comprehensive look at both the monostatic and bistatic clutter data, with the view to learn what the data shows rather than to use them to develop and verify new algorithms. This report is a documentation of that effort.

Section 2 of the report discusses the monostatic data from Flight #5, while the bistatic data from Flight #9 is discussed in Section 3. Section 4 contains the summary and conclusions. The STAP algorithms that were used are discussed briefly in the Appendix.

## Section 2

# Monostatic MCARM Data – Flight #5

## 2.1 The MCARM Receiver

The MCARM phased array antenna is housed in a flat radome mounted on the forward left side of the fuselage, ahead of the wings, of a BAC 1-11 aircraft. The MCARM aircraft is shown in Figure 2-1. The antenna has 2 rows of 16 antenna subarrays each, with each subarray containing 4 elements, followed by a corporate feed and a coherent receiver. During data collection, only an 11-over-11 section was used, thus generating 22 channels of data, with 11 degrees of freedom in azimuth and 2 degrees of freedom in elevation.

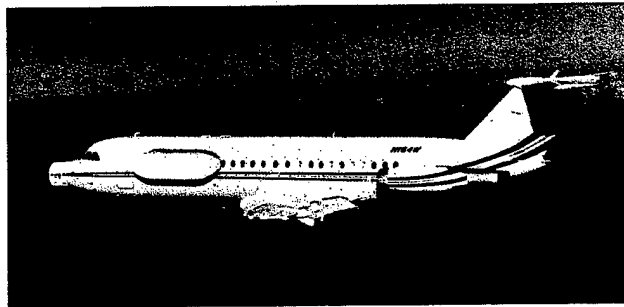


**Figure 2-1. The Northrop-Grumman BAC 1-11 Equipped with the MCARM Phased Array Antenna**

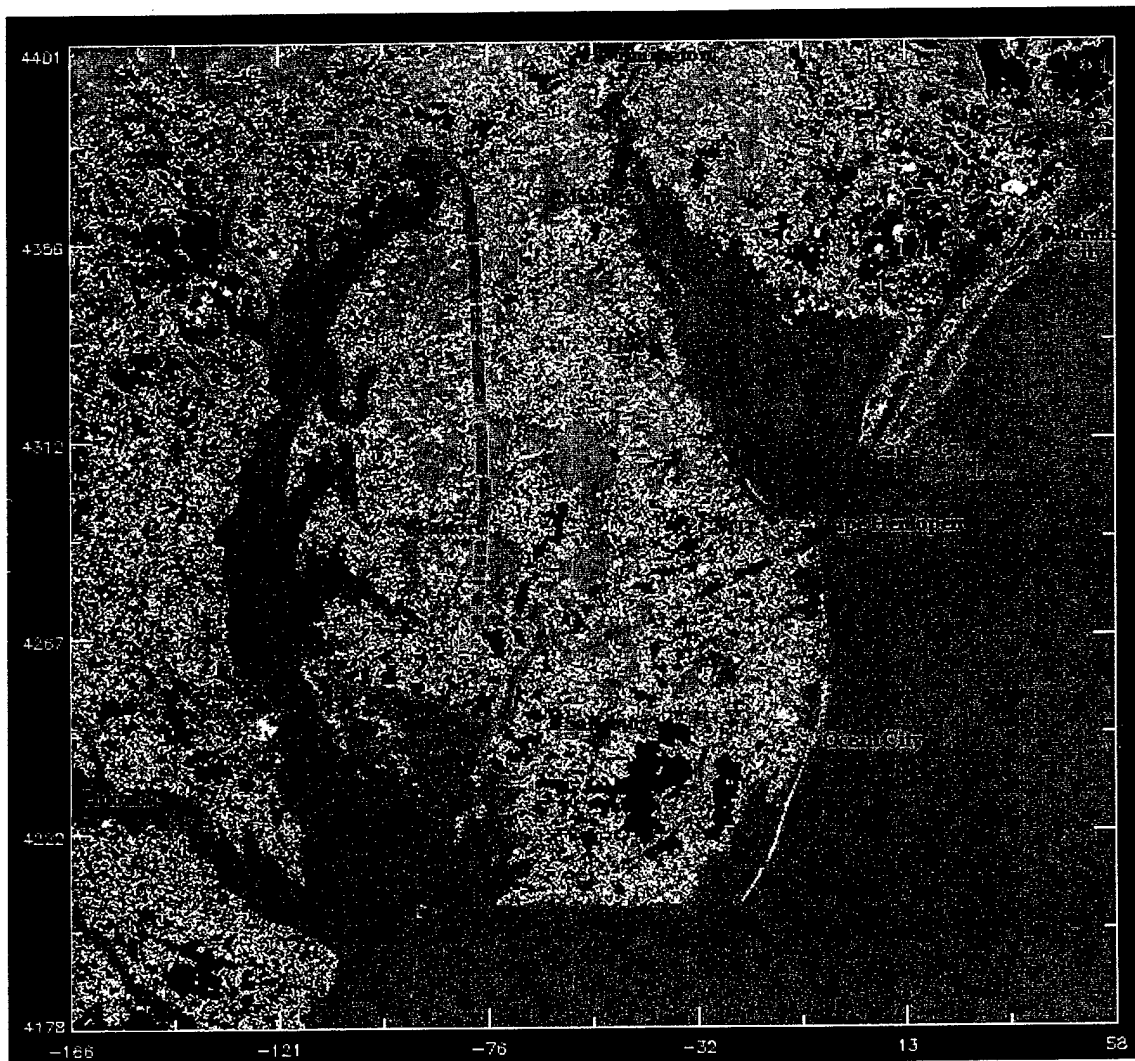
## 2.2 The Flight Path and Flight Parameters

Figure 2-2 shows the ground-track of the flight path of the BAC 1-11 aircraft on flight #5, overlaid on the DELMARVA terrain. The aircraft takes off from Baltimore–Washington International (BWI) airport and proceeds along the path shown.

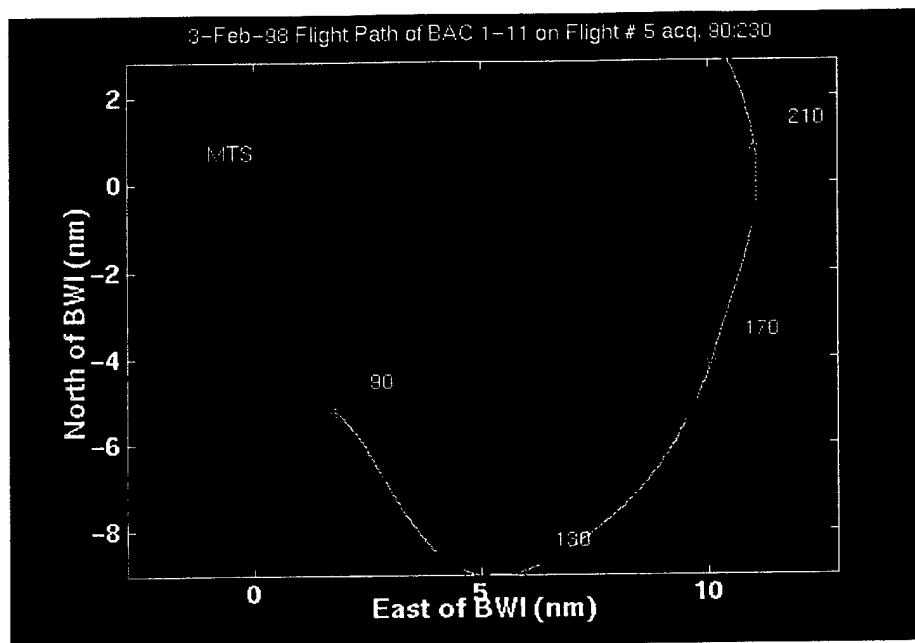
The numbers on the path are acquisition numbers associated with that location. Only some acquisition numbers are shown; there are many more acquisitions that are available in the database. The increasing acquisition numbers indicate the direction of flight. Recall that the MCARM array is on the left side of the fuselage and therefore it illuminates and receives returns from objects to the left of the aircraft.

Figure 2-3 shows the first part of the flight #5, clearly showing the position of the BWI airport and the MTS, which is located at the end of one of the runways. Each red hatch mark on the path indicates the position of the aircraft where an acquisition was made. The path

during acquisitions 90 to 230 are shown, with every 40<sup>th</sup> acquisition starting from the 90<sup>th</sup> being marked by a circle and also numbered.



**Figure 2-2. Flight Path of Monostatic Flight #5 Overlaid on the DELMARVA Terrain**



**Figure 2-3. Part of the Flight Path of the BAC 1-11 on Monostatic Flight #5**

The MTS is located near the BWI airport. For acquisitions 130-210, it is generally located to the left of the aircraft, allowing the ground around the MTS to be illuminated.

Figure 2-4 plots several flight parameters during these acquisitions.

Figure 2-4a plots the inertial navigation unit (INU) platform azimuth, where the platform azimuth is defined as the angle between the aircraft centerline and the platform x-axis. The platform x-axis is essentially pointed toward east, as shown by the platform wander angle in Figure 2-4c. Thus the platform azimuth angle indicates the orientation of the aircraft in azimuth with respect to the east.

The platform, and essentially the aircraft, roll angle is plotted in Figure 2-4b. The aircraft was in a sustained left turn during this portion of the flight and the roll angle is seen to lie between 0 and -10 degrees.

The angle between the true north and the platform x-axis is the platform wander angle and is shown in Figure 2-4c. This angle is seen to be close to 90 degrees all the time, indicating that the x-axis of the stabilized platform is pointed toward east.

The angle between the aircraft centerline and the aircraft velocity vector is the drift or the crab angle (by definition, they have the opposite signs), and is shown in Figure 2-4d.



Figure 2-4e plots the aircraft altitude. It is seen that several acquisitions were recorded while the aircraft was on the ground. The aircraft then takes off and quickly climbs to an altitude of about 7600-ft.

Figure 2-4f plots the ground speed. The unit of the recorded ground speed is supposed to be feet/sec, which can be converted into knots. Given the aircraft and MTS positions and the aircraft velocity, one can compute the expected Doppler shifts of the MTS tones, as we have done in Figure 2-4l. When this computed Doppler was compared to the observed Doppler for an acquisition in flight #9, a large discrepancy was observed. If, however, we assume the units of the recorded velocity to be knots then the computed and the observed Doppler shifts are seen to be in good agreement. We have, therefore, chosen to display the aircraft velocity assuming the units to be knots. Note that an agreement between the computed and the observed Doppler, or the lack of it, in no way affects the adaptive processing of the clutter/MTS signals, though it is critical when deciding which Doppler cell to search for a particular target. Since  $1 \text{ knot} = 1 \text{ nautical mile} / \text{hour} = 6,000 \text{ ft} / 3,600 \text{ sec} = 5/2 \text{ ft/sec} = 1.67 \text{ ft/sec}$ , the speed profile is reduced by a factor of 1.67 if we assume the recorded speed is indeed in ft/sec units.

Figure 2-4g plots the recorded transmit and receive azimuth angles and also the computed azimuth angle to the MTS on the ground. These angles are in the aircraft coordinate system, with the azimuth being measured clockwise from aircraft nose and thus a direction of 270 degrees points in a direction that is normal, i.e., broadside, to the antenna array. The transmit azimuth (x) is seen to be broadside during this portion of the flight. For the early portion, the transmit direction is shown to be about 255°, but in reality, the transmission was in broadside with a spoiled (~25°) beamwidth; the code for the spoiled beam was incorrectly interpreted as the pointing direction. While a spoiled beam was being used for transmission, the receive beam was alternately switched between broadside and  $\pm 10^\circ$  of broadside. After that, the receive (o) beam was also pointed broadside. During this portion of the flight, the MTS (+) also appears to be within  $\pm 10^\circ$  of the broadside of the antenna. Since the transmit beam is about 7.5°, the ground close to the MTS, if not the area immediately next to the MTS, is illuminated.

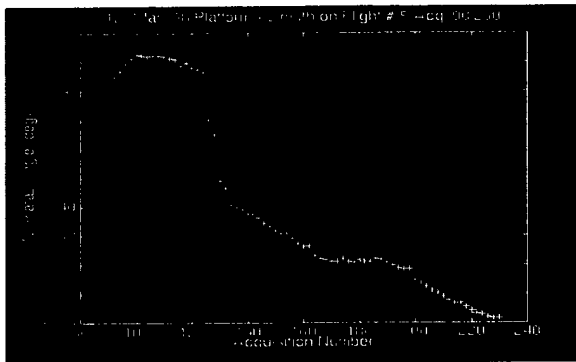
Figure 2-4h shows the aircraft roll angle as measured in the INU system, along with the computed MTS elevation angle in the aircraft coordinate system. After the aircraft has settled down, the aircraft is rolled slightly to the left while making a steady left turn, and the MTS elevation with respect to the array is almost zero. The elevation beamwidth of the array is about 13°.

Figure 2-4i plots the range, in nautical miles, to the MTS and Figure 2-4j shows the same information in terms of range cells (with sampling at 1.25 MHz, range cell width = 120 m). At a PRF of 1,984 Hz, the unambiguous range window is 630 range cells long. Thus the MTS, in about cell #180, is within the first unambiguous range window. If there is a triggering delay, its signals will appear farther away, i.e., in a cell with a higher number,

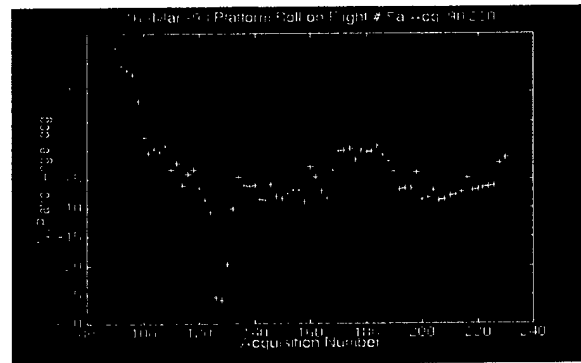
which can eventually foldover if the delay is large. During this flight, the MTS was in a free-running mode, i.e., it put out pulses at the same PRF as the MCARM radar but it was not synchronized to it.

Figure 2-4k plots the radial velocity of the MTS with respect to the MCARM aircraft. This radial velocity is computed based on the assumption that the unit of the recorded values of the velocity is knots and not fps.

Figure 2-4l plots the computed Doppler shifts of the MTS tones as received at the MCARM receiver. It should be noted that the Doppler shift of the MTS tones is proportional to the radial velocity and not twice the radial velocity. In case of the MTS, the signal originates in the MTS and traverses the distance only once to reach the receiver. In case of the skin or clutter returns, the signal traverses twice the distance between the radar and the object, i.e., from transmitter to the object and back to the receiver and thus the Doppler shift is proportional to twice the radial velocity. Therefore, the Doppler of the ground clutter from the immediate neighborhood of the MTS will be double that calculated for the MTS itself.

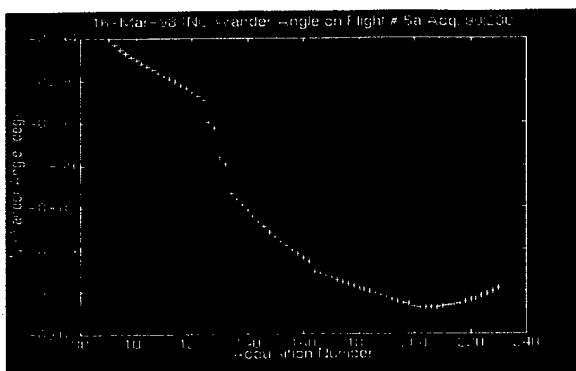


(a) Platform Azimuth

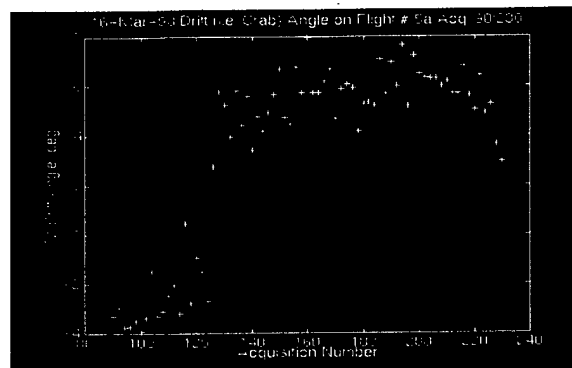


(b) Platform Roll

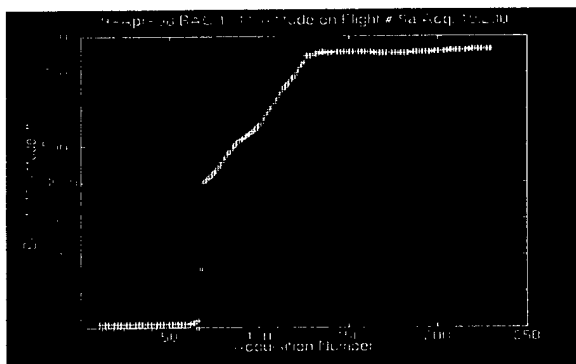
**Figure 2-4. Flight Parameters on Flight #5, Acquisitions 90 to 230**



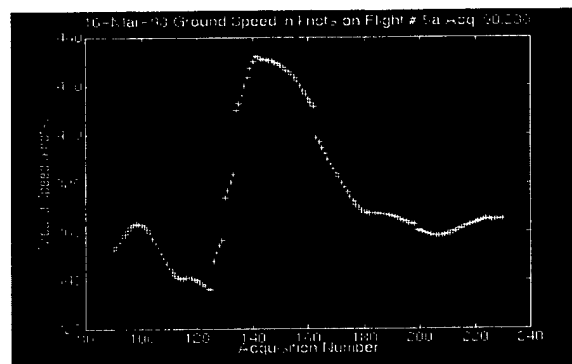
(c) Platform Wander



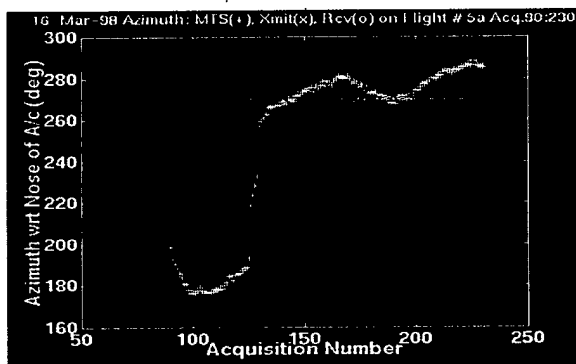
(d) Platform Drift



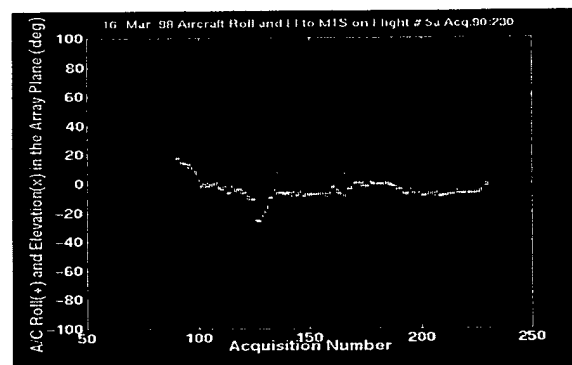
(e) Aircraft Altitude



(f) Aircraft Ground Speed

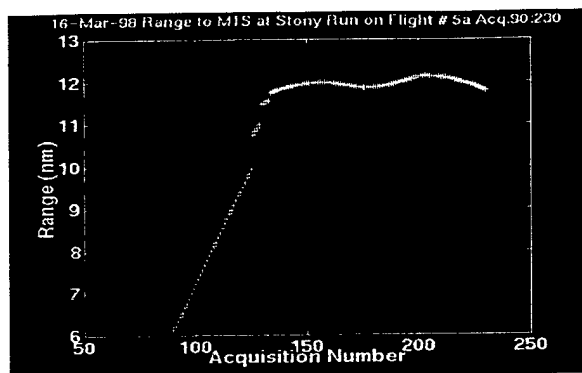


(g) Tx (x), Rx (o) and MTS (+) Angles

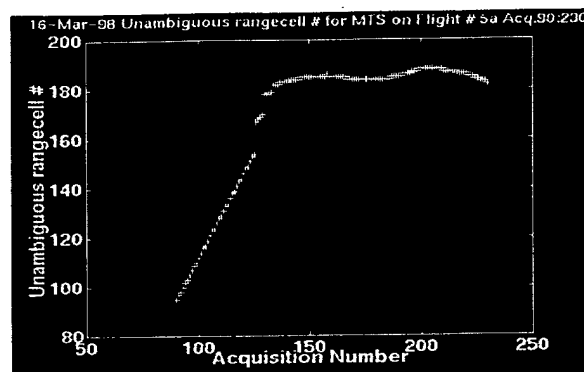


(h) A/C Roll and MTS Elevation Angles

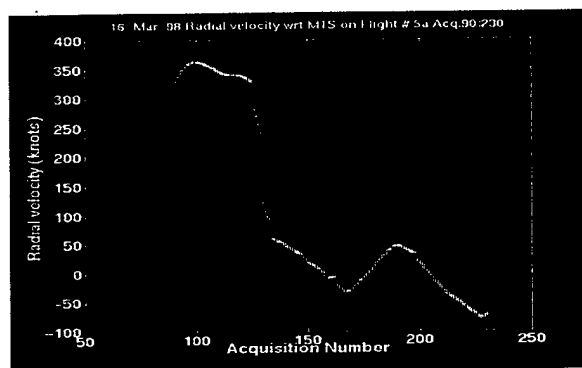
**Figure 2-4. Flight Parameters on Flight #5, Acquisitions 90 to 230 (Continued)**



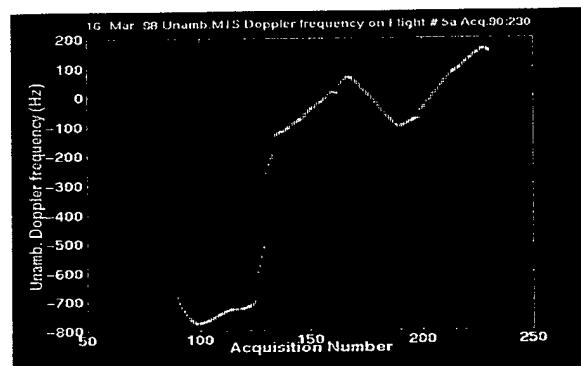
(i) Range to MTS



(j) MTS Rangecell



(k) Radial Velocity of MTS



(l) Doppler Shift of MTS Tones

**Figure 2-4. Flight Parameters on Flight #5, Acquisitions 90 to 230 (Concluded)**

## 2.3 Acquisition #5-152

On flight #5, we have looked at two acquisitions. One of them is acquisition #152, which is included in the flight path shown in Figure 2-3. On this acquisition, the MTS was located on the left side of the aircraft and the recorded data clearly shows the MTS tones that are not obscured by the ground clutter. Table 2-1 lists some of the flight and MTS parameters relevant to this acquisition. Table 2-2 lists some parameters relevant to the MTS for this acquisition.

**Table 2-1. Flight and Data Collection Parameters on Acquisition #5-152**

Parameter	Value
BAC 1-1 Altitude	7,556 ft, Range cell #39
Roll Angle	-7.5°
Pitch Angle	4.13°
Crab Angle	4.7°
Transmit Azimuth	270°(broadside)
Receive Azimuth	270°
Ground Speed	426.7 knots
PRF	1,984 Hz

**Table 2-2. MTS Parameters on Acquisition #5-152**

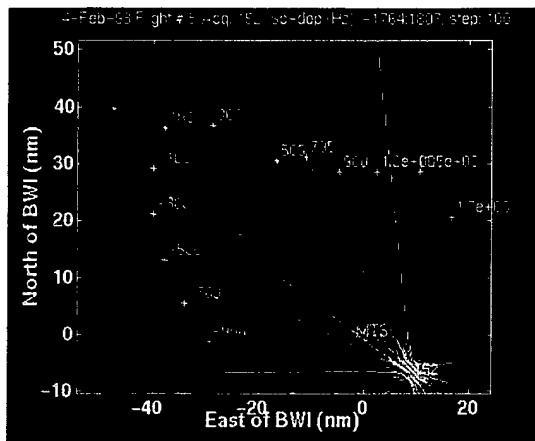
Parameter	Value
Range	11.97 nm, Range cell #185
Azimuth	275.2°
Radial Velocity	15.14 knots
Doppler Shift	-32.2 Hz
Mainlobe Doppler	-238 Hz

The MTS location corresponds to the range cell #185. As mentioned earlier, the MTS signal would show in a cell farther out because of response delays of the MTS. In this case, the MTS was actually free running, and the signal happens to appear in range cell #450.

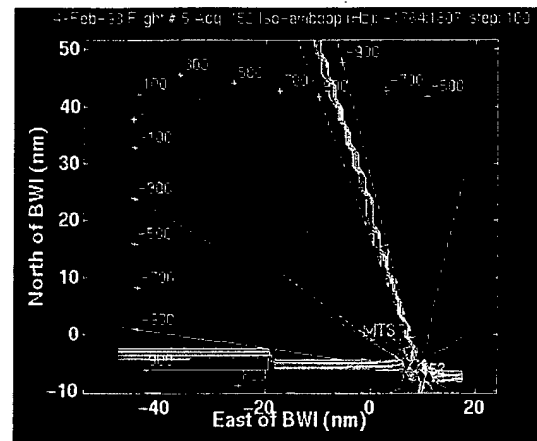
### **2.3.1 Iso-Range and Iso-Doppler Contours**

Figure 2-5a plots the iso-range contours relative to the position of the aircraft at acquisition #152 on flight #5. The range values are displayed in nautical miles. These contours are generated by computing range values at closely spaced grid points on the ground and then allowing a MATLAB contour-generating routine to compute the iso-range contours for the desired range values.





(a) Unambiguous



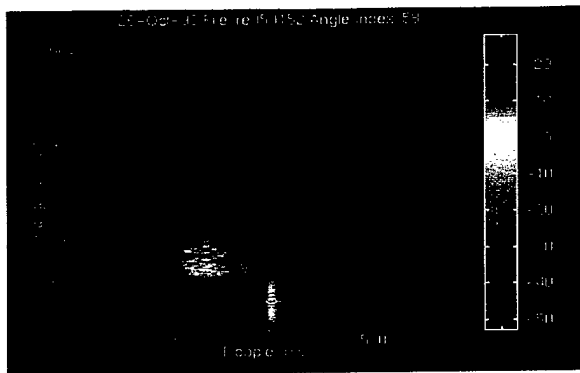
(b) Ambiguous

**Figure 2-6. The Iso-Doppler Contours at Acquisition #5-152**

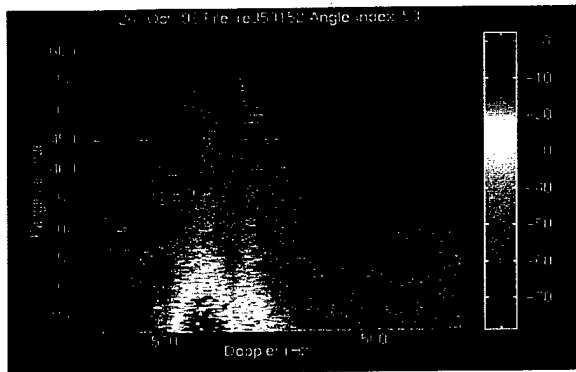
### 2.3.2 Clutter and MTS Returns

Figure 2-7 shows the range-Doppler intensity (RDI) plot for acquisition #5-152, at the angle index 58, which corresponds to the azimuth angle, about  $-275^\circ$ , of the MTS on the ground. Figure 2-7a covers almost all the range cells, namely from cell #1 to cell #625 (the range window contains 630 cells) and the complete Doppler window, namely from about  $-990$  Hz to  $990$  Hz (the Doppler window is  $\pm 992$  Hz). The scenario is dominated by the strong response in cell #68 at about  $0$  Hz. This happens to be the leakage from the transmitter into the receiver. Note that the range window clearly starts before the pulse is transmitted, and any range measurement based on range cell number of the response has to account for this fact.

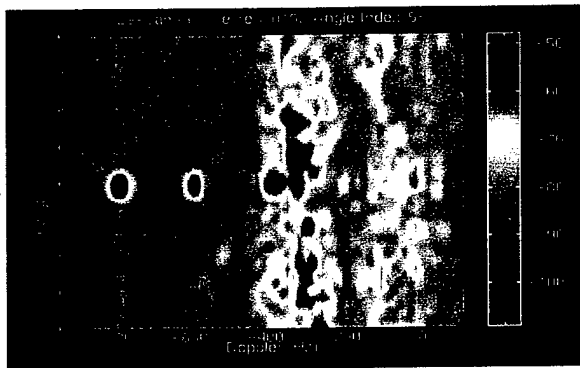
Figure 2-7b attempts to emphasize the rest of the return by starting from range cell #125. The strong returns from the near-in range cells from cell #125 to about cell #300 are clearly seen. One can also observe the MTS tones in range cell #450. Figure 2-7 c shows the RDI plot only for the cells 44-460, clearly showing a few of the MTS tones. Figure 2-7 d is a horizontal cut through cell #450 in the Figure 2-7c.



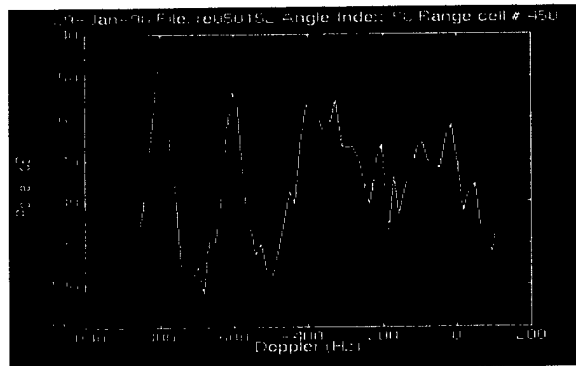
(a) Range Cells 1-625



(b) Range Cells 125-625



(c) Range Cells 440-460



(d) Cut Through Range Cell #450

**Figure 2-7. RDI Plot on Acquisition #5-152**

Table 2-3 lists the first 12 peaks in Figure 2-7d. The highest observed peak is at  $-806$  Hz, at a level of  $-48$  dB. Recalling that the MTS transmits five tones at the nominal frequencies of  $-800$ ,  $-600$ ,  $-400$ ,  $-200$ , and  $0$  Hz, we can expect to see 4 other tones at or close to these values. Indeed, we note tones at  $-604$ ,  $-403$ ,  $-201$ , and  $-15$ , which are close enough to the true values. Note that the order of the last 2 tones is switched in magnitude. The other observed peaks are spurious.

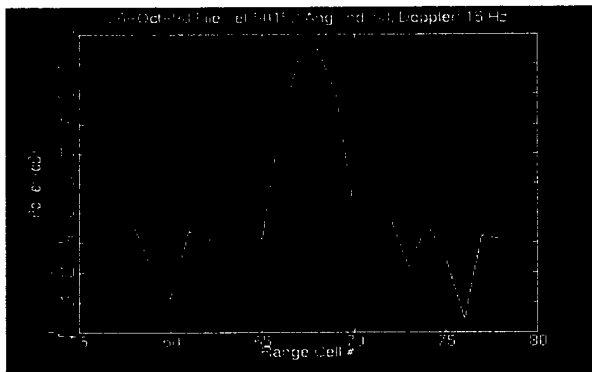
On the average, the observed tones are shifted by about 3 Hz from the nominal values. We had earlier calculated the expected Doppler shift to be about  $-32$  Hz, on the assumption that the recorded aircraft velocity units are knots and not fps as claimed in the report [1]. Clearly, the observed offset is much less than this computed value. The discrepancy may be due to an error in the recorded crab angle. Even if the units are actually fps, the expected Doppler shift becomes about  $-20$  Hz, which is still different from the observed value.



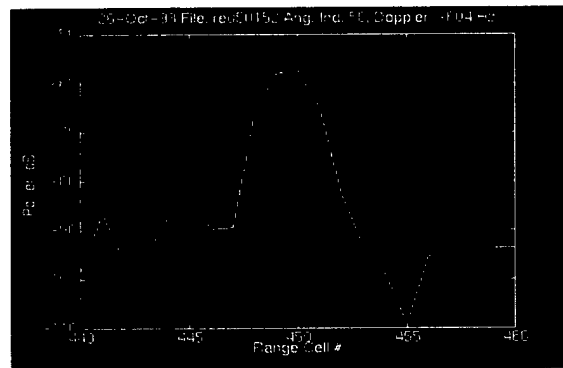
**Table 2-3. Twelve Highest Peaks in Figure 2-6d**

Peak #	dB	Freq. (Hz)	Corresponding Nominal MTS Tones
1	-48	-806	-800
2	-53	-604	-600
3	-55	-325	
4	-56	-403	-400
5	-61	-15	0
6	-65	-93	
7	-66	-201	-200
8	-66	-279	
9	-73	-170	
10	-75	46	
11	-77	-449	
12	80	186	

Figure 2-8 shows that the transmitter or the MTS pulses do not occupy only one cell, but several. This necessitates the use of guard cells when applying STAP algorithms.



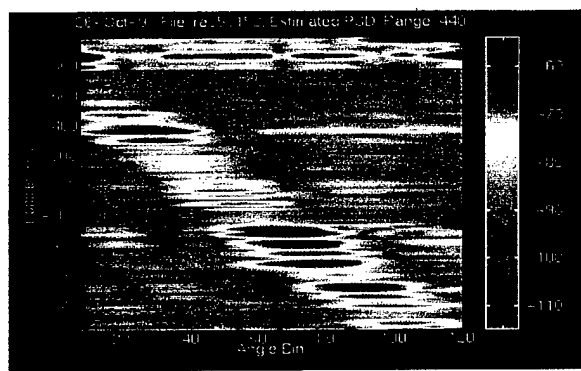
(a) MCARM Transmitter Leakage Pulse



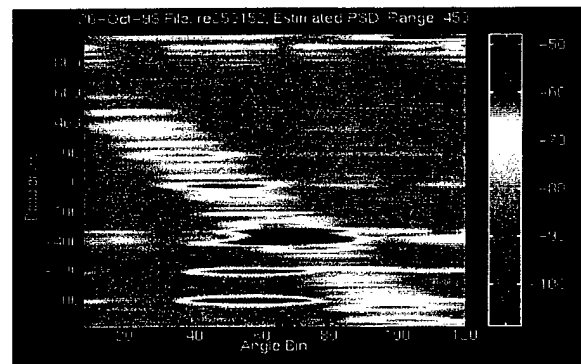
(b) MTS Pulse

**Figure 2-8. MCARM Transmitter and MTS Pulse Width**

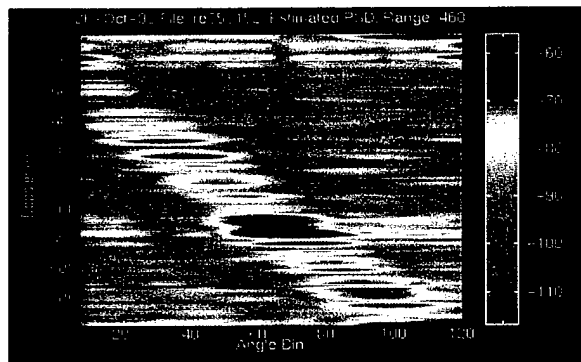
Figure 2-9 shows the angle-Doppler plots for 3 range cells; namely, cell #s 440, 450, and 460. The plot for cell #450 shows the presence of the tones, while the plots for the cells 440 and 460 do not display the tones. A vertical cut at angle index of 58 in Figure 2-9b produces the same list of peaks as in Table 2-3. Figure 2-9d is a horizontal cut at -604 Hz in Figure 2-9b, showing that the peak is at an index of 57, confirming that the MTS is indeed located at an angle index of about  $-275^\circ$ , as was computed earlier.



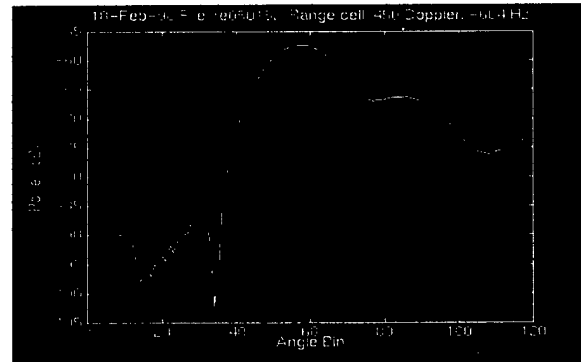
(a) Range Cell #440



(b) Range Cell #450



(c) Range Cell #460



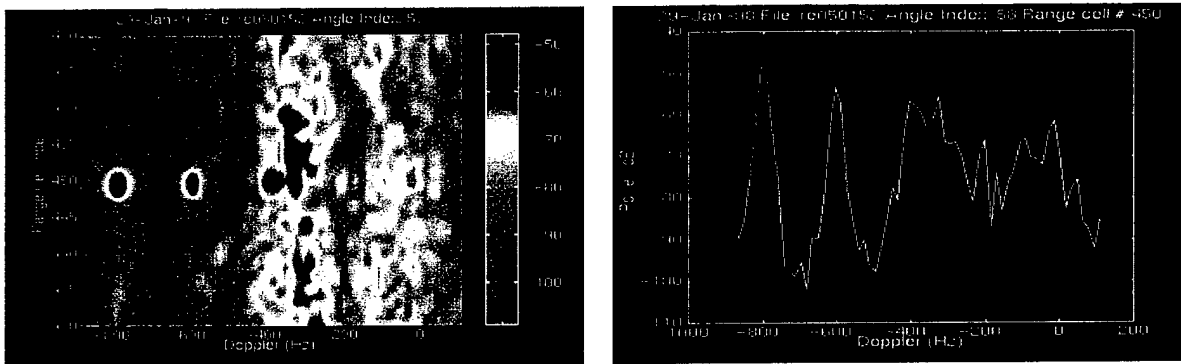
(d) Range Cell #450, Cut at -604 Hz

**Figure 2-9. Angle-Doppler Plot on Acquisition #5-152**

### 2.3.3 FTS and EFA Algorithms Applied to Acquisition #5-152 with Angle Index 58

Figure 2-10 shows the unadapted RDI plot for cells 430-470 with angle index 58, which is in the direction of the MTS; a cut through range cell #450 is shown in Figure 2-10b. The tones at the nominal frequencies of -800 and -600 stand almost in the clear, while the tones at the other 3 nominal frequencies of -400, -200 and 0 Hz are corrupted by clutter to various degrees. The results of applying various STAP algorithms should be compared to these 2 figures.

Figure 2-11a is the result of applying the Factored Time Space (FTS) algorithm (see Appendix A), using only one elevation row of the antenna, a 100-cell support and allows for 3 guard cells in the fore and three cells in the aft of the test cell. Of the 100 support cells, 50 are in the fore and 50 are in the aft of the test cell. The tones at -800, -600, -400, and 0 Hz are seen quite clearly. The tone at -200 Hz is also quite apparent, though it seems to be reduced in magnitude compared to the other tones.



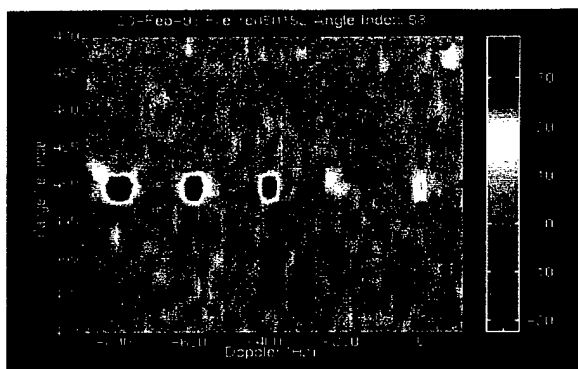
(a) Unadapted RDI

(b) Cut Through Cell 450

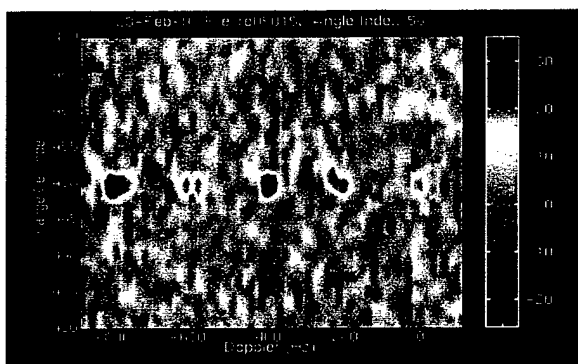
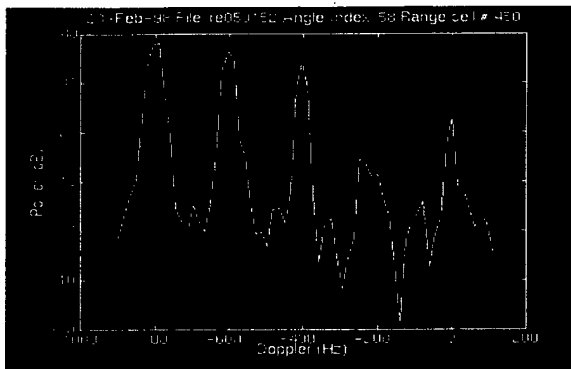
**Figure 2-10. Unadapted RDI, Acquisition #5-152, Angle Index 58**

The result of including both elevation rows, i.e., all 22 channels, without increasing the support, is shown in Figure 2-11b. The results appear to be worse than the 11-channel case.

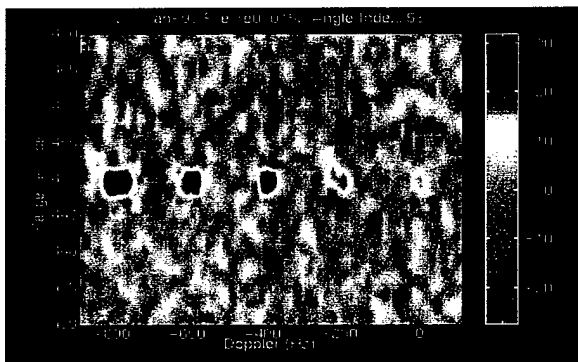
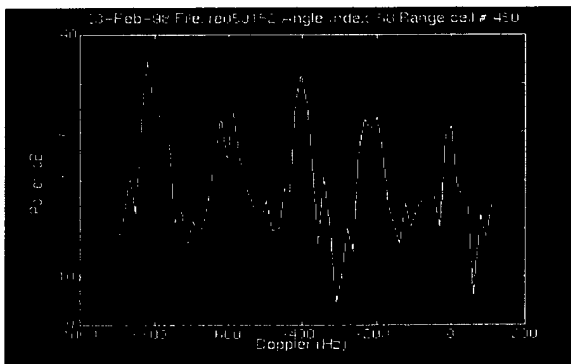
The result of increasing the sample support to 200 is shown in Figure 2-11c. All the tones are visible, though the peaks are tending to split. Note that the 200 range cells cover not only a swath that is  $200 * 120 = 24,000$  m wide in the immediate neighborhood of the test cell, it actually encompasses, because of the foldover in range, another 24 km from about 40 nm (~72 km) away.



(a) Channels: 11; Support:  $(-50, +50)$ ; Guard Cells:  $\pm 3$



(b) Channels: 22; Support:  $(-50, +50)$ ; Guard Cells:  $\pm 3$



(c) Channels: 22; Support:  $(-100, +100)$ ; Guard Cells:  $\pm 3$

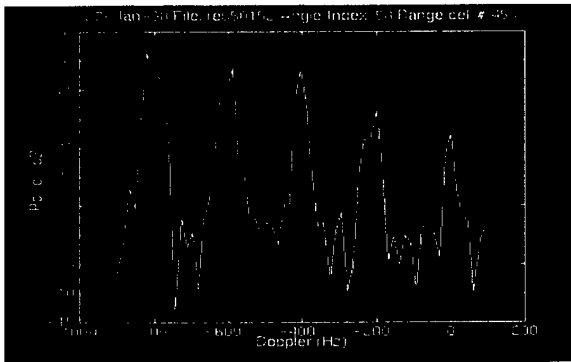
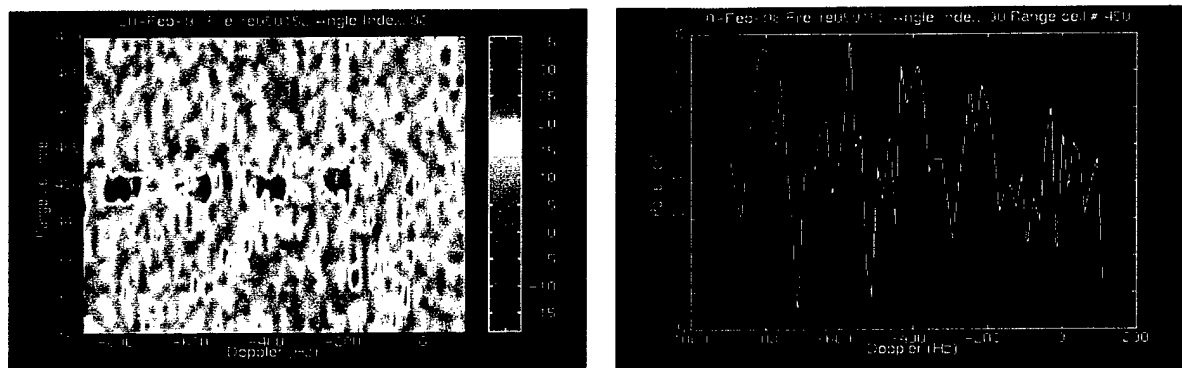


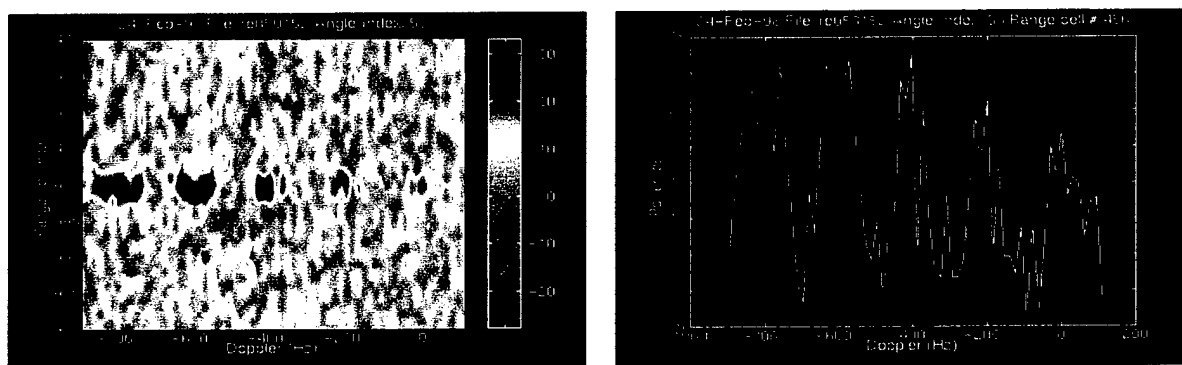
**Figure 2-11. FTS Algorithms Applied to Acquisition #5-152, Angle Index 58**

The results of applying the Extended Factored Algorithm (EFA) STAP algorithm (see Appendix A) are shown Figures 2-12a and 2-12b. The former uses only 11 channels, i.e., 1

row, with 66-cell support; the latter uses all 22 channels and 198-cell support. Neither result looks impressive.



(a) Channels: 11; Support: (-33,+33); Guard Cells:  $\pm 3$



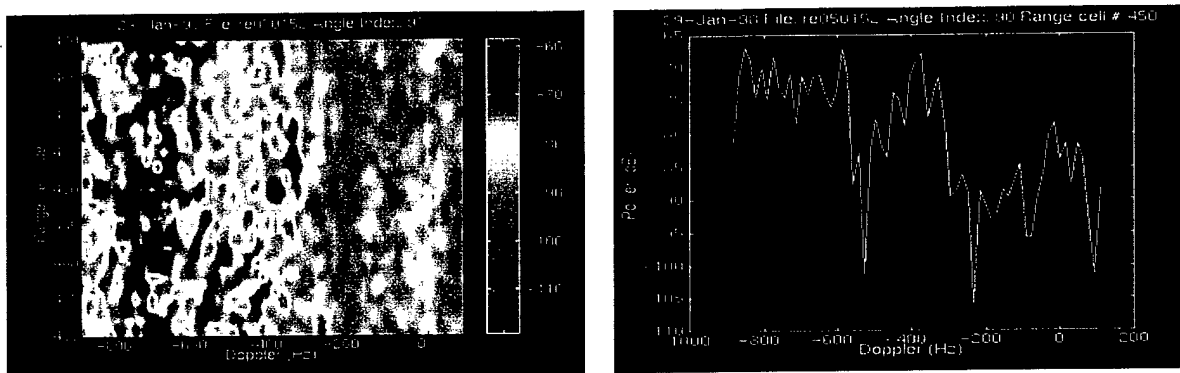
(b) Channels: 22; Support: (-99,+99); Guard Cells:  $\pm 3$

**Figure 2-12. EFA Algorithms Applied to Acquisition #5-152, Angle Index 58**

#### 2.3.4 FTS and EFA Algorithms Applied to Acquisition #5-152 with Angle Index 90

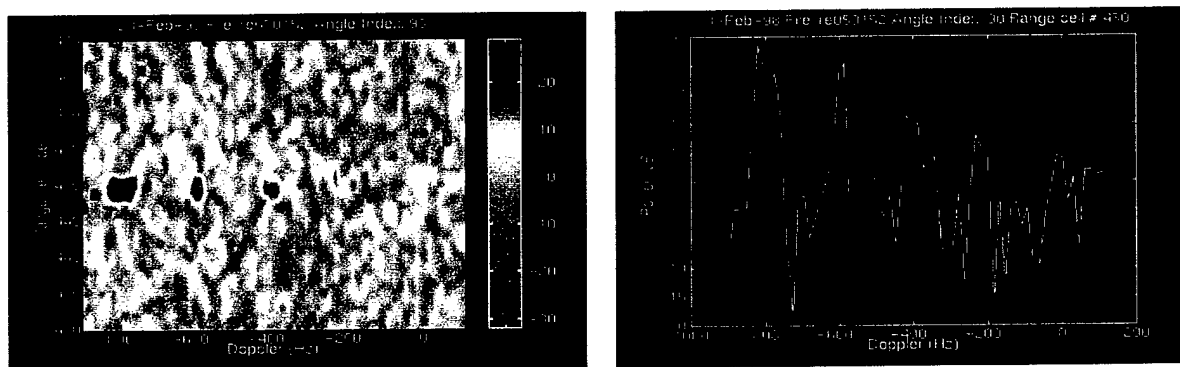
In Section 2.2.3, we used the angle index 58, which directed the receive beam almost at the MTS, and therefore at least two of the five tones were clearly visible outside the clutter. It is interesting to see how the results are affected if the pointing direction of the receive beam is now changed to point it more towards the tail of the aircraft, thus emphasizing the clutter at the more negative frequencies.

Figure 2-13 is the unadapted RDI plot for angle index 90. The clutter obscures most of the five tones at the nominal frequencies of -800, -600, -400, -200, and 0 Hz.



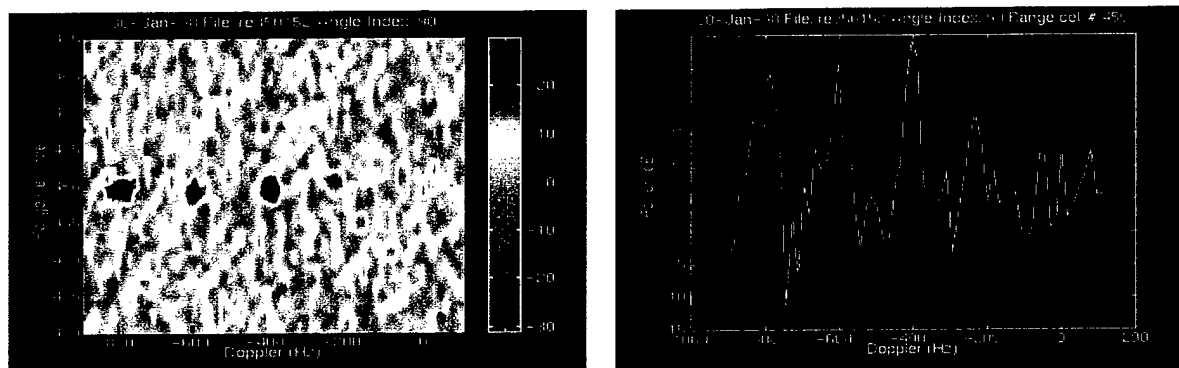
**Figure 2-13. Unadapted RDI, Acquisition #5-152, Angle Index 90**

Figure 2-14 is the result of applying FTS, using all 22 channels, 200-cell sample support and  $\pm 3$  guard cells. The adaptive process does bring out all the 5 tones, though the peaks appear to break somewhat.



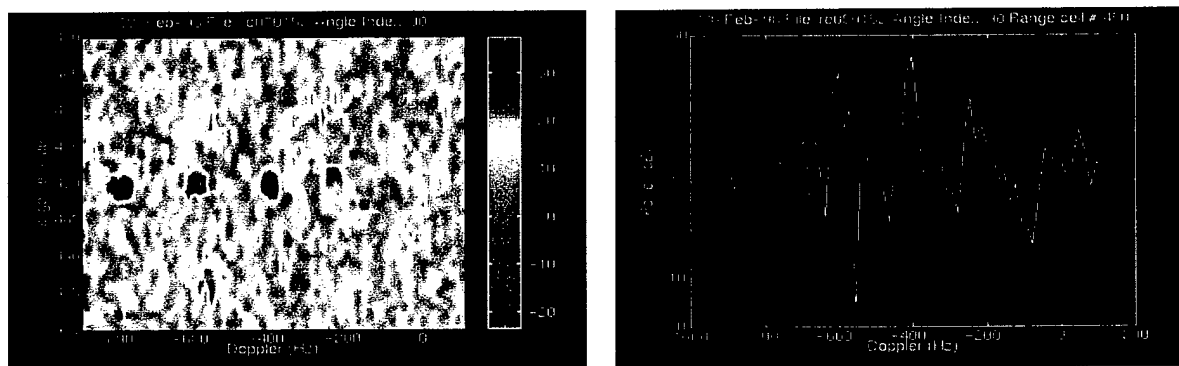
**Figure 2-14. FTS Algorithms Applied to Acquisition #5-152, Angle Index 90,  
Channels: 22; Support: (-100,+100); Guard Cells:  $\pm 3$**

Figure 2-15 shows the result with 11 channels, a 46-cell support and  $\pm 3$  guard cells. Again the 5 tones are visible, though the 0 Hz tone seems to be surrounded by clutter residues.



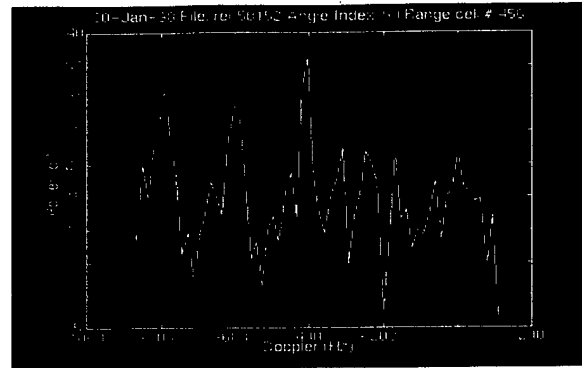
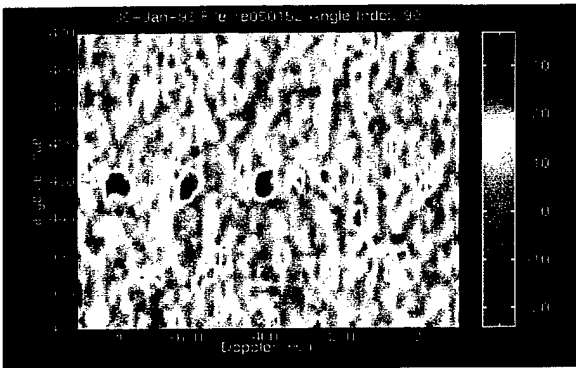
**Figure 2-15. FTS Algorithms Applied to Acquisition #5-152, Angle Index 90,  
Channels: 11; Support: (-28,+18); Guard Cells:  $\pm 3$**

Figures 2-16a to 2-16d show the results of using FTS with 11 channels, 22-cell support and  $\pm 10$ ,  $\pm 3$ ,  $\pm 2$ , and  $\pm 1$  guard cells, respectively. The first 3 tones are visible in all cases except the last, which allows for only one guard cell on either side.

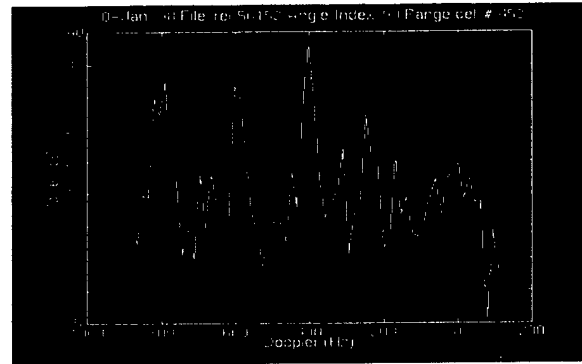
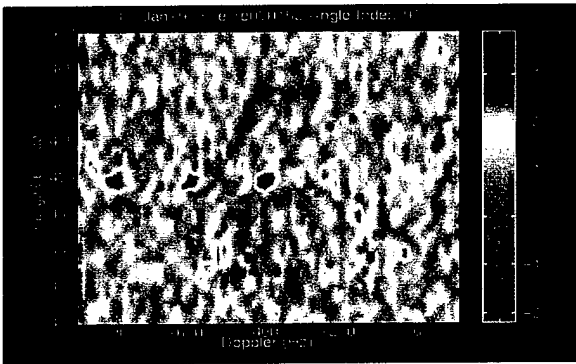


**(a) Guard Cells:  $\pm 10$**

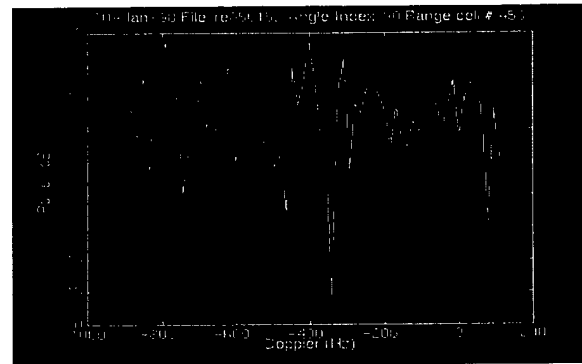
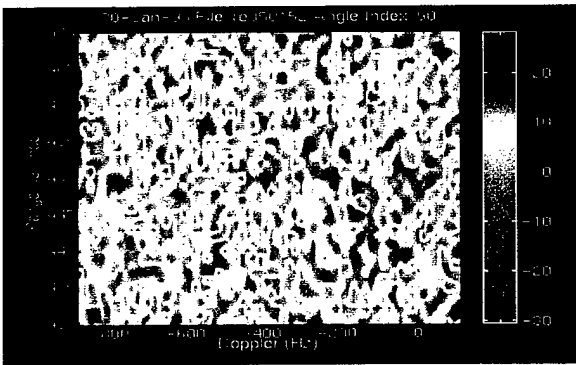
**Figure 2-16. FTS Algorithms Applied to Acquisition #5-152, Angle Index 90,  
Channels: 11; Support: (-11,+11)**



(b) Guard Cells:  $\pm 3$



(c) Guard Cells:  $\pm 2$



(d) Guard Cells:  $\pm 1$

**Figure 2-16. FTS Algorithms Applied to Acquisition #5-152, Angle Index 90, Channels: 11; Support: (-11,+11) (Concluded)**



Figure 2-17 presents the results of applying the EFA algorithm with all 22 channels and using a 198-cell support and  $\pm 3$  guard cells.

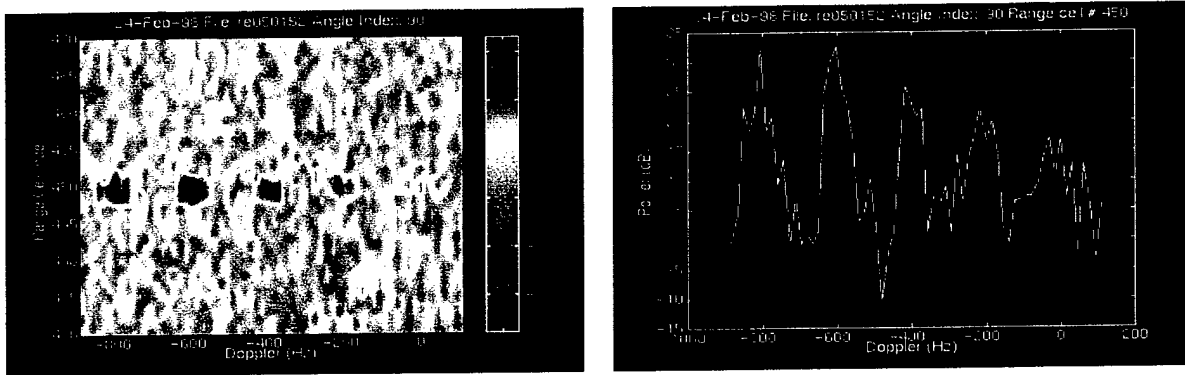


**Figure 2-17. EFA Algorithms Applied to Acquisition #5-152, Angle Index 90, Channels: 22; Support: (-99,+99); Guard Cells:  $\pm 3$**

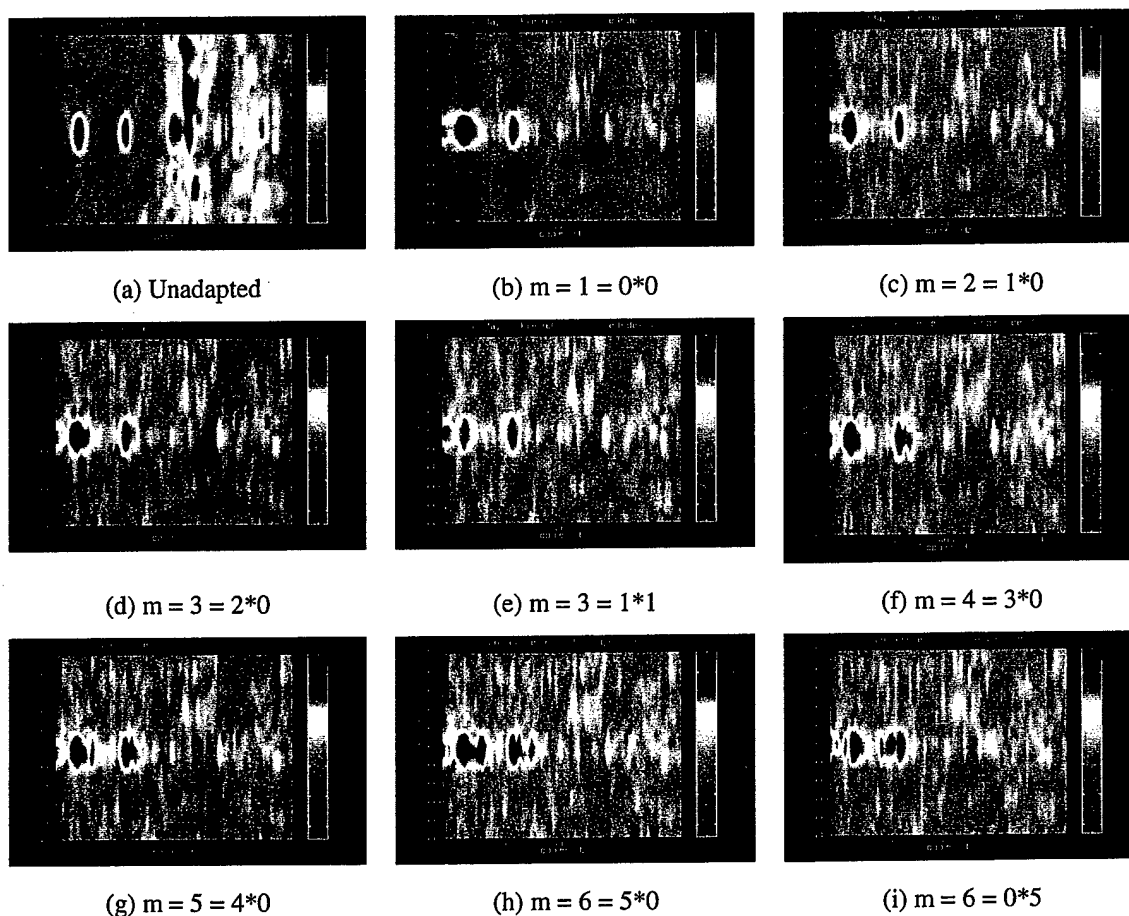
### 2.3.5 JDL-mxn Algorithms Applied to Acquisition #5-152, Angle Index 58

Figures 2-18, 2-19 and 2-20 show the results of applying the Joint Domain Localized (JDL)-mxn algorithm, described in Appendix A, to the acquisition #5-152 with angle index 58. The JDL-mxn algorithm uses mxn degrees of freedom in the Doppler-beam space, comprised of m Doppler bins and n beams or steering directions. The m Doppler bins and the n beams can be chosen in different ways. We have chosen to depict the choice as  $(m_1 * m_2) \times (n_1 * n_2)$ , where  $m = m_1 + 1 + m_2$  and  $n = n_1 + 1 + n_2$ , with  $m_1$  being the number of Doppler bins ahead of the selected Doppler bin and  $m_2$  being the number of Doppler bins following the selected bin. Similarly,  $n_1$  is the number of beams ahead of the selected beam and  $n_2$  is the number of beams following the selected beam. For all choices of m and n in this figure, the sample support comprises 20 range cells before and 10 range cells after the selected range cell, i.e., a total of 30 range cells. Also, in all cases,  $\pm 3$  guard cells are used.

Figure 2-18a is the unadapted RDI plot, covering only the range cells 440-460 and the frequency range -900 to 100 Hz. In this plot, the tones at -800 and -600 stand out in the clear; the tone at -400 seems to be visible, though the ground clutter is in the neighborhood; the tones at -200 and 0 Hz are not recognizable. The relative amplitudes of the tones are shown in Figure 2-6d.

Figure 2-18b is the result of applying JDL-  $(0*0) \times (0*0)$ , which, when simplified, is the JDL-1x1, i.e., the degrees of freedom in both the domains are unity. The tones at -800 and -600 Hz are still visible and the ground clutter is largely eliminated, but so are the tones at -400, -200, and 0 Hz.

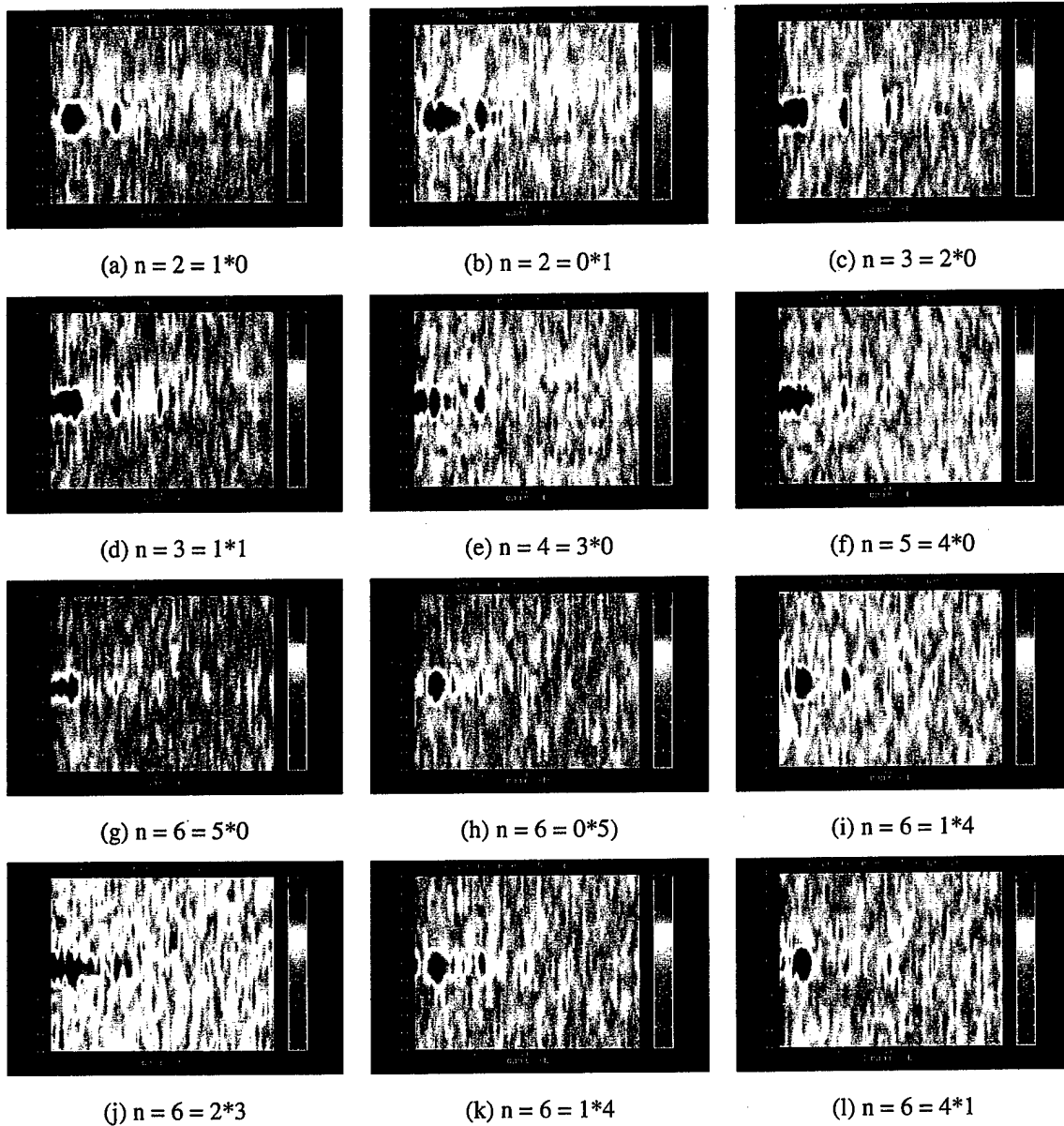
Figures 2-18c to 2-18i use degrees of freedom only in the Doppler domain, and in all these cases, we seem to have lost the lower three tones along with the clutter.



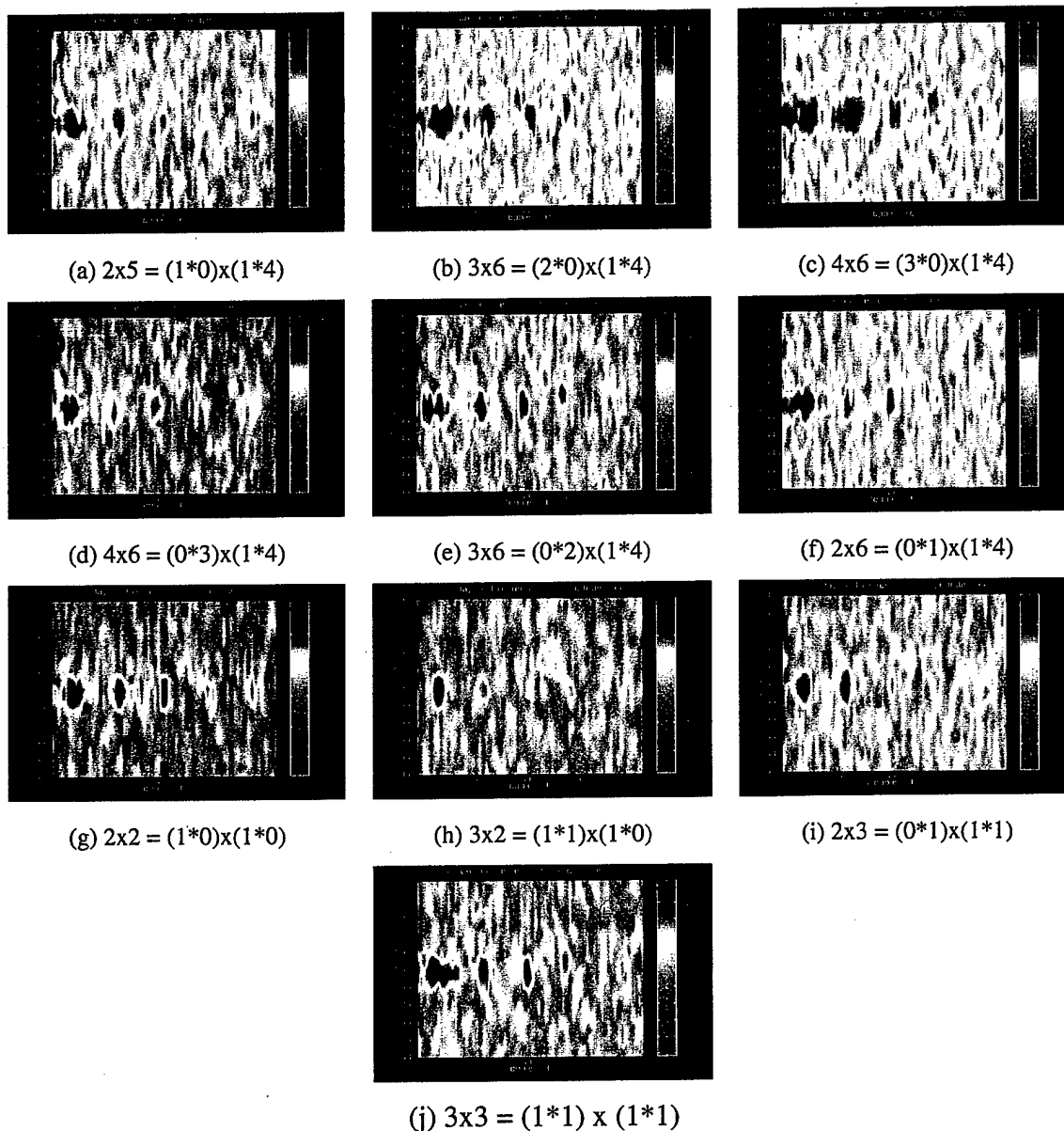
**Figure 2-18. JDL<sub>mx1</sub> Algorithms Applied to Acquisition #5-152, Angle Index 58;  
Channels: 22; Support Cells: (-20, +10); Guard Cells:  $\pm 3$**

Figure 2-19 is the result of applying the JDL 1xn algorithm to this acquisition. Figures 2-19a and 2-19b use 2 degrees of freedom in the beamspace domain, i.e., 2 beams. Now the tone at -400 Hz is clearly visible, with the tones at -200 and 0 Hz also faintly observable. Different degrees of freedom in the beamspace domain are tried in Figures 2-19c to 2-19l.

Figure 2-20 combines degrees of freedom in the beamspace domain with degrees of freedom in the Doppler domain.



**Figure 2-19. JDL\_1xn Algorithms Applied to Acquisition #5-152, Angle Index 58;  
Channels: 22; Support Cells: (-20, +10); Guard Cells:  $\pm 3$**



**Figure 2-20. JDL\_mxn Algorithms Applied to Acquisition #5-152, Angle Index 58;  
Channels: 22; Support Cells: (-20, +10); Guard Cells:  $\pm 3$**

Comparing these results, it appears that for this acquisition, JDL 1x6, (where 1x6 is selected as  $(0*0) \times (3*2)$ , shown in Figure 2-19k), seems to perform the best. This adapted RDI is repeated in Figure 2-21a and a cut through range cell #450 for this case is shown in Figure 2-21b.

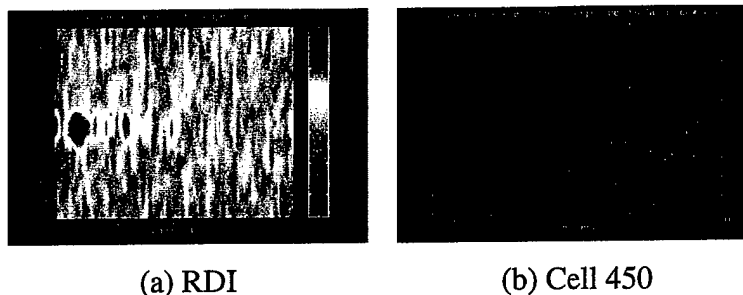


**Figure 2-21. JDL\_1x6 = (0\*0)x(3\*2) Algorithm Applied to Acquisition #5-152, Angle Index 58; Channels: 22; Support Cells: (-20, +10); Guard Cells:  $\pm 3$**

## 2.4 Acquisition #5-575 – Looking for the Sabreliner

Figure 2-22 shows a portion of the flight #5 flight path where the target aircraft, a Sabreliner, was also aloft and almost broadside to the MCARM antenna. This portion of the flight path is a continuation of flight path shown in Figure 2-3 and is included in Figure 2-2.

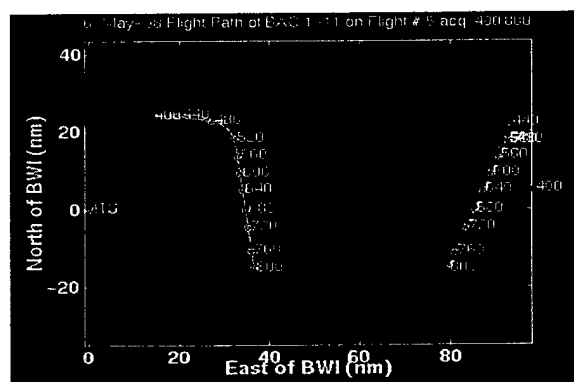


**Figure 2-22. Flight Paths of BAC 1-11 and Sabreliner on Flight #5**

Table 2-4 lists some of the parameters relevant to this acquisition. The target is at a range of 57.12 nm, or cell #882, which is in the second range ambiguity window (unambiguous range window is about 40 nm  $\approx$  630 range cells). The folded-over range cell should be  $882 - 630 = 253$ , but recall that the transmit pulse appears in range cell #68. Therefore, the target should appear in  $252 + 68 = 320$ .

The target's azimuth with respect to the BAC 1-11 aircraft is computed to be  $268.9^\circ$ , while the transmit and receive azimuth are both at  $270^\circ$ . Since the azimuth beamwidth is at

least  $7.5^\circ$ , it may be expected that the MCARM radar illuminates the target, and the MCARM antenna receives the skin returns.

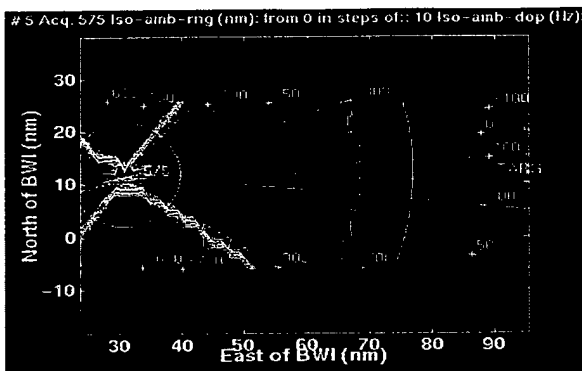
The aircraft was flying with a crab angle of  $-7.3^\circ$ . The relative velocity of the target with respect to the BAC 1-11 is computed to be  $-122.8$  knots, which translates to a Doppler shift of  $522.5$  Hz. Because of the crab angle, the mainbeam clutter Doppler is non-zero; it is computed to be  $219.1$  Hz. Recall that we have made the assumption that the recorded BAC 1-11 velocity is in units of knots and not fps. It is assumed that the Sabreliner velocity is recorded in the proper units (decimeters/sec). Since the difference in Doppler shift of the target return and the mainbeam clutter should only be a function of the target velocity, the computed difference of  $522.5 - 219.1 = 303.4$  Hz, is independent of the BAC 1-11 velocity, and independent of what units we chose for that velocity.

**Table 2-4. Target Parameters on Acquisition #5-575**

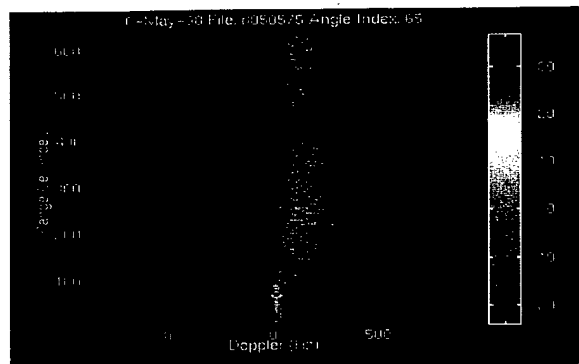
Parameter	Value
Range	57.12 nm
Range Cell	Absolute: 882; Ambiguous: 320
Target Azimuth	$268.9^\circ$
Transmit/Receive Azimuth	$270^\circ/270^\circ$
Crab Angle	$-7.3^\circ$
Radial Velocity	$-122.8$ knots
Target Doppler Frequency	$522.5$ Hz
Mainbeam Doppler Frequency	$219.1$ Hz

Figure 2-23a plots the iso-range and iso-Doppler contours for the ground clutter. The ground point of the target is shown. Note that the target range indicated by the range contours is valid, but the Doppler contours do not indicate the Doppler shift of the target skin return. The Doppler contours only indicate the Doppler shift of the ground clutter return.

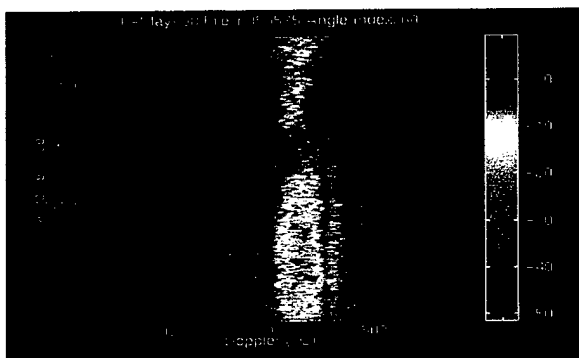
Figure 2-23b is a RDI plot for all the range cells and the complete Doppler window of  $\pm 992$  Hz. The strong return in range cell #68 at about 0 Doppler is, of course, the leakage pulse. Figure 2-23c repeats this plot for cells 150-630 only, thus suppressing the strong return in cell 68. The near in clutter return is quite strong, slowly fading toward the far ranges. Note that the very far ranges have folded over on to the near ranges. The mainbeam clutter Doppler seems to be centered on about 150 Hz and has a spread of about 200 Hz. Figure 2-23d shows a cut through cell 320 in Figure 2-23c.



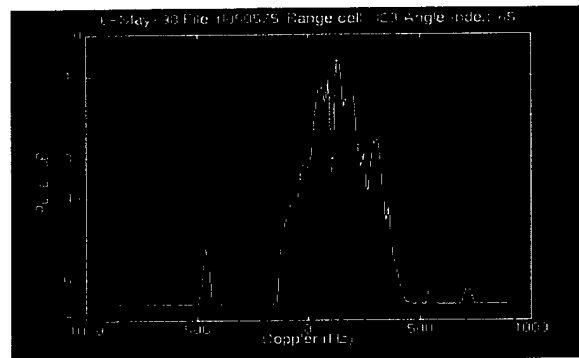
(a) Iso-range/iso-Doppler Plot



(b) RDI Plot, Cells 1-630, Angle Index 65



(c) RDI, Cells 150-630, Ang. Ind. 60



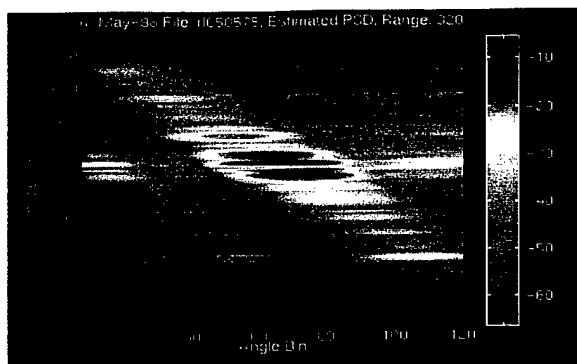
(d) Cut Through Cell #320 in (c)

### Figure 2-23. Acquisition #5-575 – Looking for the Sabreliner

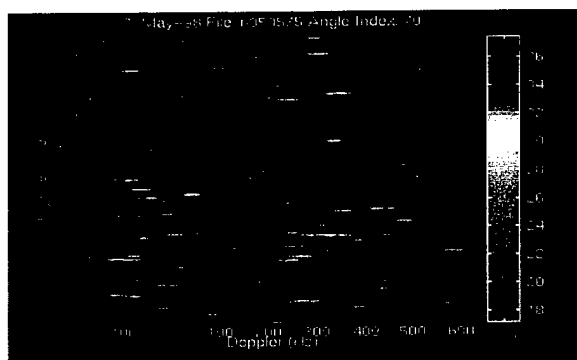
We have already noted that the target Doppler should be as much as 300 Hz above the clutter Doppler. Also, given the geometry, the target was being looked at from the side; thus, a large radar cross section (RCS) would have been seen. We are, therefore, surprised not to see a strong return in a range cell around cell #320, and in a Doppler bin around 522 Hz, or a little less.

Figure 2-24 shows the angle-Doppler plot for this acquisition. The linear clutter ridge is clearly seen.

Figure 2-25 shows the RDI plot after applying a JDL-3x3 clutter suppression algorithm to it. The angle index used is 70, the sample support is 20 range cells and 3 guard cells are allowed on either side. A relatively strong return is observed in a range cell around 300, at a Doppler of about 325 Hz. But it is not clear if this is the Sabreliner, which was expected in range cell around 320 with a Doppler at around 522 Hz. Our conclusion is that, for whatever reason, the Sabreliner was not evident in the data.



**Figure 2-24. Angle-Doppler Plot, Range Cell #320, Acquisition #5-575**



**Figure 2-25. JDL-3x3 Algorithm Applied to Acquisition #5-575, Angle Index 70;  
Channels: 22; Support Cells: (-10, +10); Guard Cells:  $\pm 3$**



### Section 3

## Bistatic MCARM Data – Flight #9

### 3.1 The Tethered Aerostat Radar System (TARS)

During the MCARM bistatic data collection, a copy of the MCARM waveform generator was used to excite the L-band transmitter of a TARS aerostat (Figure 3-1) that hovered in place at an altitude of about 10,000 feet and was tethered at the Horse Shoe Beach on the western coast of Florida, at a distance of about 51 nm from Gainesville. The TARS has a space-stabilized rotating parabolic dish, rotating at a 5 rpm rate, and is programmed to radiate only when the  $2.2^\circ$  main beam starts to pass over the MTS location.

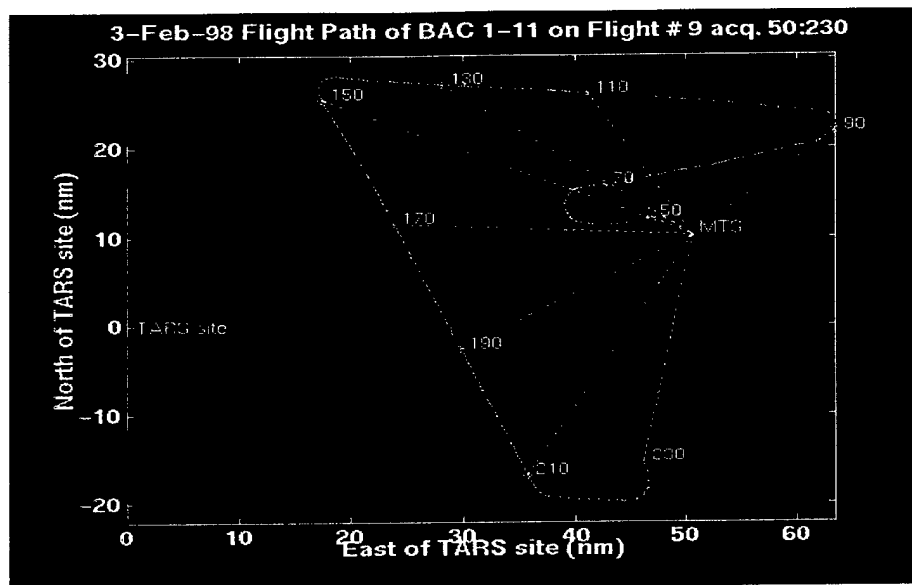


**Figure 3-1. The TARS Aerostat Carrying the Bistatic Transmitter**

The BAC 1-11 (see Figure 2-1) carries the MCARM radar, which is used only as a passive receiver on this flight. A sensor on the BAC 1-11 senses the sidelobes of the TARS' sidelobe radiation and alerts the MCARM radar, which then starts recording data. MTS transmits the exact same waveform as the TARS radar ( $f_0 = 1,240$  MHz, PRF = 23,148 Hz,  $1.6 \mu\text{s}$  dumb pulses), but is not synchronized to the TARS pulses. During each revolution of the TARS antenna every 12 seconds, the MCARM receiver records for about 100 ms, straddling the TARS beam-dwell time of about 70 ms. There were several hundred such bistatic acquisitions recorded on flight #9.

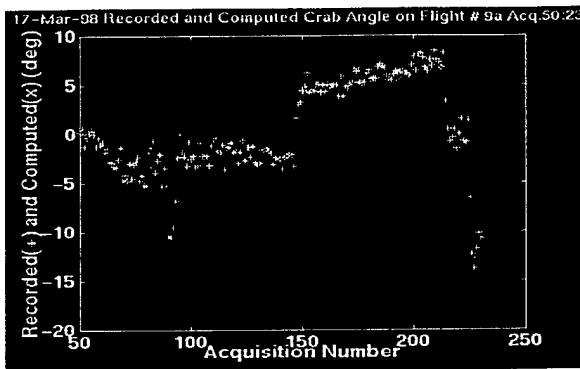
### 3.2 The Flight Path and Flight Parameters

Figure 3-2 shows the flight path during acquisitions 50-230 on flight #9. The BAC 1-11 takes off from the Gainesville airport in Florida and makes several counterclockwise loops around the MTS located near the Gainesville airport, thus presenting the left side mounted phased array antenna toward the MTS. Only one loop is shown. The increasing acquisition numbers indicate the direction of flight.

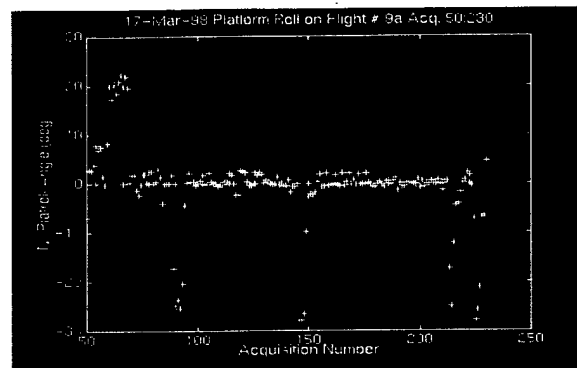


**Figure 3-2. Part of the Flight Path of Bistatic Flight #9**

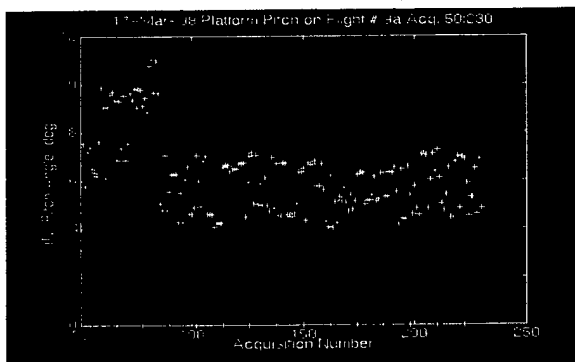
Figure 3-3 plots several flight parameters, namely, crab angle, roll angle, pitch angle, altitude, ground speed and TARS to BAC 1-11 range. The altitude is shown in ambiguous range cells. The ground-speed is shown based on the assumption that the units of the recorded velocity are knots and not fps as claimed in [1]. If the units are accepted to be fps, these numbers should be reduced by a factor of 1.67. Figure 3-4 plots some of the MTS-related parameters on Flight #9.



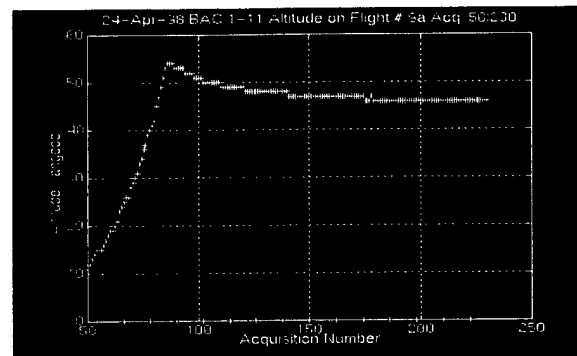
(a) Crab Angle



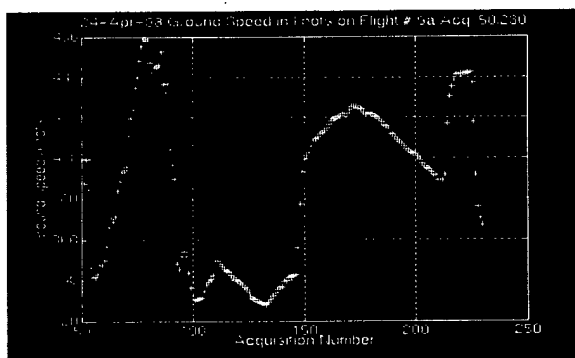
(b) Roll Angle



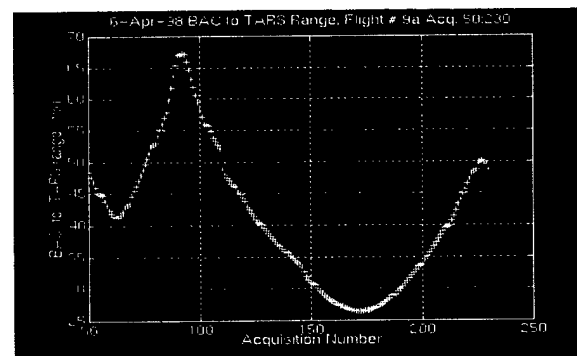
(c) Pitch Angle



(d) Altitude

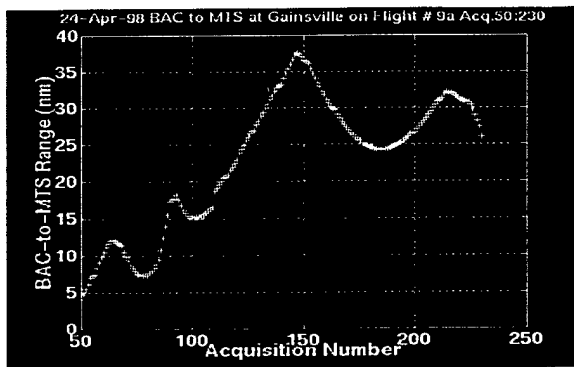


(e) Ground Speed

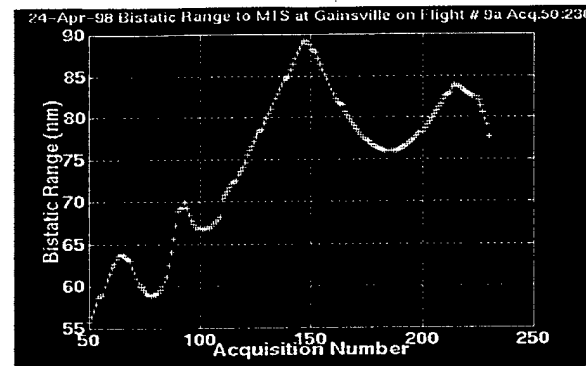


(f) TARS-to-BAC 1-11 Range

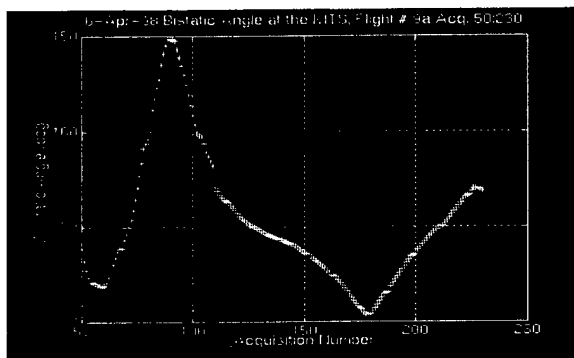
**Figure 3-3. Flight Parameters on Flight #9, Acquisitions 50-230**



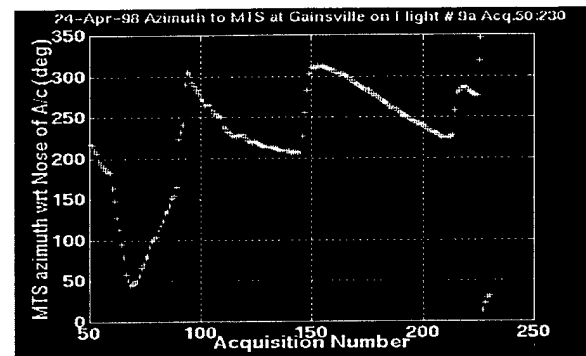
(a) BAC 1-11 to MTS Range



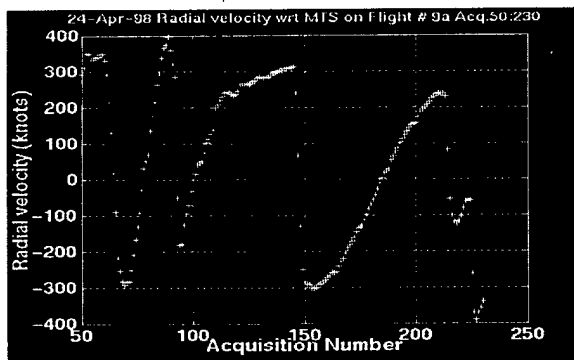
(b) Bistatic Range



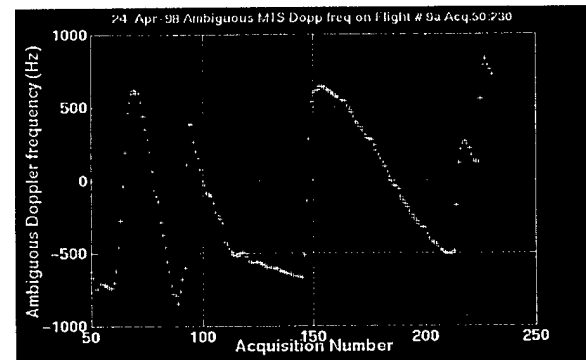
(c) Bistatic Angle



(d) Azimuth to MTS



(e) Apparent Radial Velocity of MTS



(f) Unambiguous Doppler

**Figure 3-4. MTS-Related Parameters on Flight #9**

### 3.3 Acquisition #9-110

#### 3.3.1 Iso-Bistatic Range and Iso-Bistatic Doppler Contours

Table 3-1 lists some of the flight parameters relevant to acquisition #9-110; Table 3-2 lists parameters pertaining to the MTS during this acquisition. Note that the TARS transmitter is located at a range of more than 51 nm from the target area, while the MCARM receiver is located at about 19 nm, i.e., the receiver is much closer to the target area than is the transmitter. The bistatic range is about 70 nm and the bistatic angle is about  $70^\circ$ . The PRF is 23,148 Hz. At the data sampling rate of 1.25 MHz, there are only 54 bistatic range cells of 240 m each in each pulse repetition interval, i.e., the range folds over every  $54 \times 240 = 12,960$  m or about 7 nm. The MTS azimuth is  $238.4^\circ$ , i.e., about  $27^\circ$  aft of the broadside of the antenna.

The effective radial velocity of the MTS is 199.8 knots, which translates to a Doppler shift of the MTS signals of  $-424.8$  Hz. Because the TARS transmitter is essentially stationary, the Doppler shift of the ground clutter depends on only the velocity of the BAC 1-11, without the doubling that occurs in the monostatic case. Thus the clutter Doppler for the MTS neighborhood has the same Doppler shift as the MTS and should be around  $-424$  Hz.

**Table 3-1. Flight and Data Collection Parameters on Acquisition #9-110**

Parameter	Value
BAC 1-1 Altitude	~10 kft, Range cell #39
TARS-BAC Range	48.7 nm
Roll Angle	$-0.24^\circ$
Pitch Angle	$4.08^\circ$
Crab Angle	$0.64^\circ$
Receive Azimuth	$270^\circ$
Ground Speed	344.7 knots
PRF	23,148 Hz
Range Cells per IPP	54

**Table 3-2. MTS Parameters on Acquisition #9-110**

Parameter	Value
TARS-MTS Range	51.67 nm
BAC-MTS Range	18.66 nm
Bistatic Range	70.33 nm, Range Cell 543
Ambiguous Range Cell	3
Bistatic Angle	70.53°
Azimuth	238.4°
Radial Velocity	199.8 knots
Doppler Shift	-424.8 Hz

Figure 3-5 shows the iso-bistatic range and iso-bistatic Doppler contours on the ground for acquisition #9-110. The bistatic range is the total range from the TARS transmitter to the point on the ground and from that point to the MCARM receiver. As in the monostatic case discussed in Section 2, we first compute the bistatic range for closely spaced grid points on the ground and then allow a MATLAB contour routine to find the contours at the desired values. In Figure 3-5a, the range contours are shown for the ranges at which they foldover into the primary 7-nm bistatic range window. The dotted line joining the TARS ground point with the BAC 1-11 ground point shows the approximate region on the ground that is illuminated by the narrow TARS beam, though we have not made any attempt to show the strength of illumination along this region. We may guess that the illumination is the strongest around the MTS and falls off in either direction. It appears that we can expect at least five or six foldovers in range and the data indeed shows about this number of foldovers.

Figure 3-5b shows the bistatic Doppler contours. The bistatic transmitter on the TARS is essentially stationary and hence the bistatic Doppler depends on the BAC 1-11 motion only and the Doppler contours appear to have the same nature and orientation as the monostatic Doppler contours. However, unlike the monostatic Doppler, the bistatic Doppler shifts are half the value because the transmitter-to-ground range is constant, with only the ground-to-receiver range being subject to change due to the BAC 1-11 velocity. And for the same reason, the shift for the MTS tones, unlike the monostatic case, is the same as that of the ground clutter in the MTS neighborhood. The MTS Doppler shift was computed to be about -424 Hz.

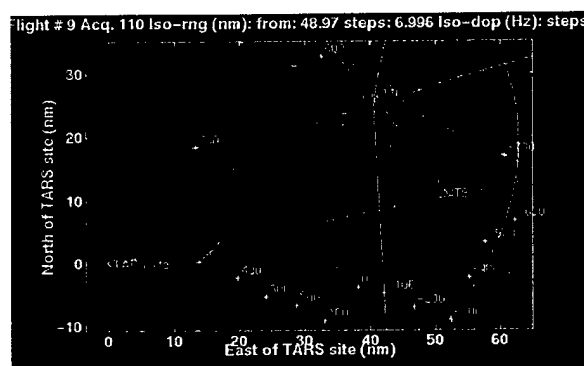
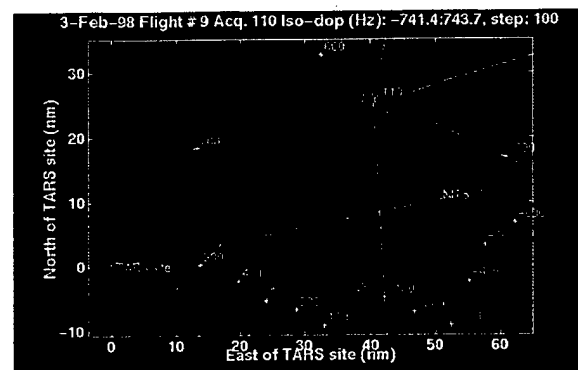
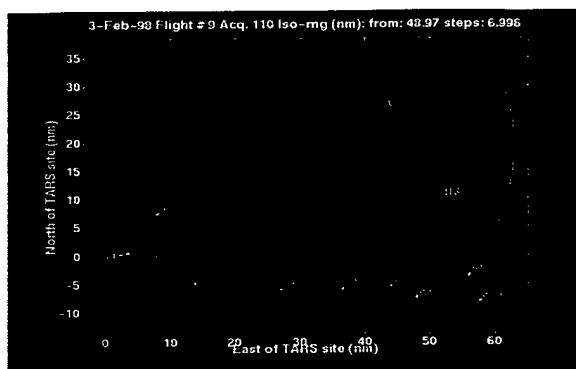


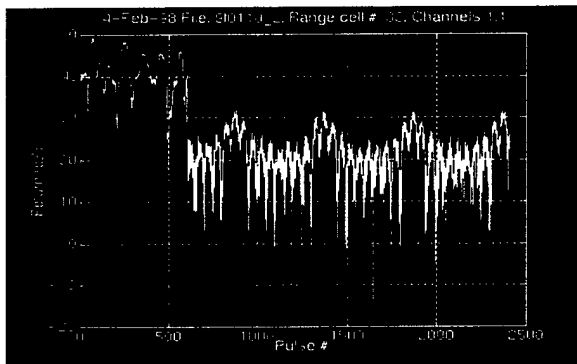
**Figure 3-5. Iso-Bistatic Range and Iso-Bistatic Doppler Contours, Acquisition #9-110**

### 3.3.2 Clutter-Free MTS Returns in Acquisition #9-110

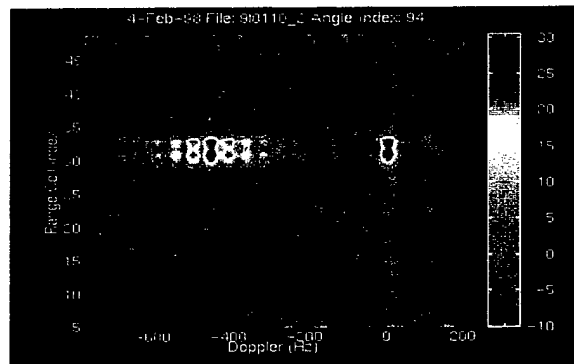
Figure 3-6 shows the nature of the MTS signal. Figure 3-6a plots the signal strength in cell #33 against the pulse numbers. Recall that the MCARM receiver starts recording when alerted by a sensor that the TARS is transmitting, which it does while its rotating beam dwells on the MTS location on the ground. The MCARM receiver can delay the start of its recording by a specified amount. It records for about 100 ms, which, at 23,148 Hz PRF, would record about 2,314 pulses. On flight #9, all of the CPIs actually have 2408 pulses included.

The TARS beam dwell time is about 70 ms and the TARS probably transmits a little longer than that, maybe 100 ms. But because of the delay introduced in the start of the recording, the CPI may record only a part of the transmissions. For the remainder of the CPI, it records only the MTS signals, which is in a free-running mode and transmits continuously.

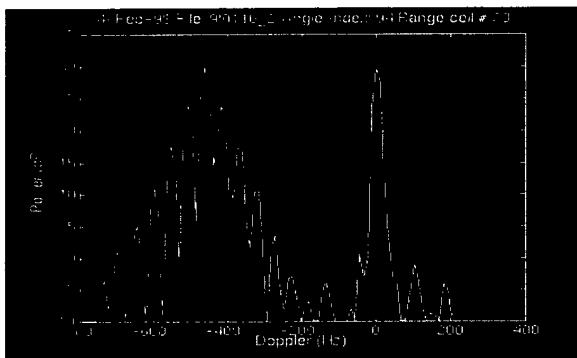
In this particular CPI, only the first 650 or so pulses contain clutter returns, after which the transmitter is turned off until the mainbeam returns to the MTS during the next revolution of the antenna. During the rest of the CPI, i.e., to pulse #2408, only MTS tones are recorded. The MTS signal happens to be in cell #33 in this CPI; actually the radar as well as the MTS pulses, which are nominally  $1.6 \mu\text{s}$  wide, occupy about three range cells.



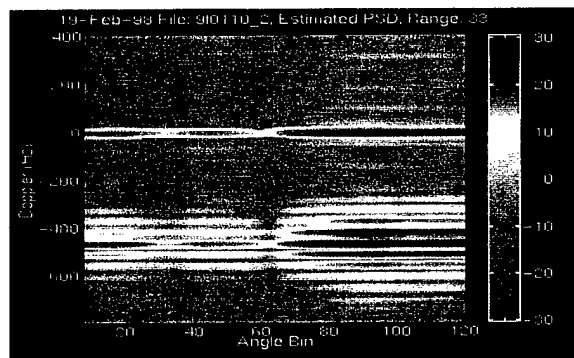
(a) Signal Strength Versus Pulse Number



(b) RDI Plot with MTS Only



(c) Cut Through Cell #33



(d) ADI Plot, Cell #33

**Figure 3-6. The MTS Signal on Acquisition #9-110**

Several observations may be made from Figure 3-6a. Firstly, the time-domain structure observed in the MTS signal is due to the beating of the many tones in the MTS signals. Secondly, the MTS signal is roughly 20 dB below the clutter in power level, i.e., the clutter-to-signal ratio (CSR) is about 20 dB. But because the clutter lasts for only about 650 pulses while the signal lasts for all 2408 pulses, the energy ratio is about 14 dB in cell #33 over the complete set of pulses. If pulses beyond 650 are considered, the clutter-to-signal ratio is 0 (i.e.,  $-\infty$  dB), while if only pulses from the first 650 pulses are considered, the ratio is



20 dB. By choosing the section of the CPI to be processed, we can vary the CSR between - $\mu$  and 20 dB.

Figure 3-6b shows the RDI plot with the MTS signal only, i.e., pulse 650 and higher. The dynamic range is set at 40 dB, leaving the background almost clear. (The same plot is repeated in Figure 3-10d with a dynamic range of about 60 dB, showing more of a speckled background). A horizontal cut through cell #33 of this plot is shown in Figure 3-6c. The 'Christmas Tree' structure of the tone cluster, with a tone offset by 500 Hz, is clearly observable. The nominal characteristics of the MTS tones are shown in Table 3-3 and observed characteristics are listed in Table 3-4. The observed tones are Doppler shifted by -463 Hz, which agrees quite well with the computed value of -424 Hz. In deed, this agreement between the observed and the computed Doppler in this acquisition prompted us to assume that the units to be used for the recorded velocity of the BAC 1-11 was knots, and not fps. Had we used fps as the units, the computed Doppler shift would have been about -253 Hz, which is quite different from the observed value of -463 Hz. The strong offset tone has been purposely included in the set of MTS tones, so that it is likely to stand out of the mainbeam clutter and enable the verification and location of the MTS tones when the main cluster is submerged in ground clutter.

The magnitude and frequency of the observed tones, normalized to the peak tone, is given in Table 3-5. Apparently, the tones are 45 Hz apart rather than the intended 50 Hz. The eleventh tone is a spurious picked up by the peak-finding routine that searched for the 12 highest peaks. This peak can be seen in Figure 3-6c.

Figure 3-6d shows the Angle Doppler Intensity (ADI) plot for the MTS-only case. Since there is no clutter, there is no 'clutter-ridge'. The tones are visible at almost all angles because of the significant sidelobes of the MCARM antenna. The peak of the response is seen to occur at an angle index of 94, which is close to the computed azimuth location of the MTS with respect to the MCARM antenna.

**Table 3-3. The MTS Tones – Design Characteristics**

#	1	2	3	4	5	6	7	8	9	10	11	12
dB	-30	-24	-18	-12	-6	0	-6	-12	-18	-24	-30	0
Hz	-250	-200	-150	-100	-50	0	+50	+100	+150	+200	+250	+500

**Table 3-4. Observed MTS Tones on Acquisition #9-110**

#	1	2	3	4	5	6	7	8	9	10	11	12
dB	1	5	11	17	24	30	23	17	10	3	0	29
Hz	-700	-644	-599	-553	-508	-463	-418	-372	-316	-271	-45	0

**Table 3-5. Observed MTS Tones on Acquisition #9-110  
(Normalized to the Central Peak)**

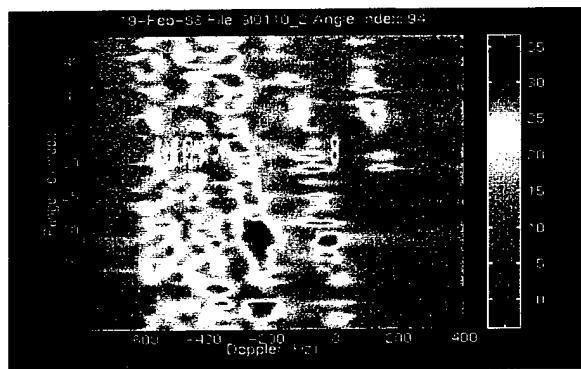
#	1	2	3	4	5	6	7	8	9	10	11	12
dB	-29	-25	-19	-13	-6	0	-7	-13	-20	-27	-30	-1
Hz	-237	-181	-136	-90	-45	0	45	90	147	192	418	0

### 3.3.3 MTS Signal Plus Clutter in Acquisition #9-110

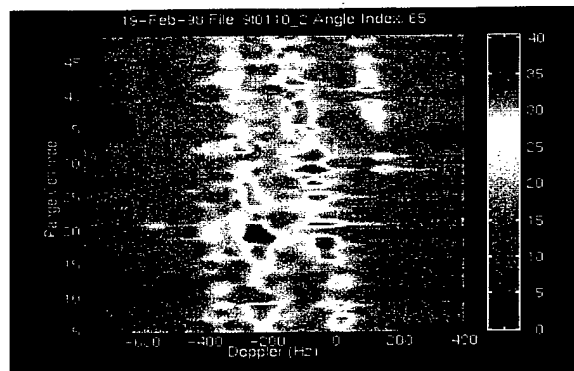
Figure 3-7 shows the RDI when all the pulses in acquisition #9-110 are used, i.e., now we have both clutter as well as the MTS tones, with a CSR of about 14 dB.

Figure 3-7a plots the RDI with an angle index of 94, i.e., the receive beam is pointed at the MTS. Since we already know that the MTS tones occur in cell #33, the outlines of the tones can be made out; otherwise, the tones are practically obscured by the clutter returns. It is clear that the long, narrow swath of ground illuminated by the TARS beam has folded over about five times, since we can see 5 distinct patches of clutter. The central patch appears to be the strongest for this angle index, and it more or less coincides with the main MTS tone cluster. Because of the clutter foldover, the MTS offset tone is also straddled by the clutter returns.

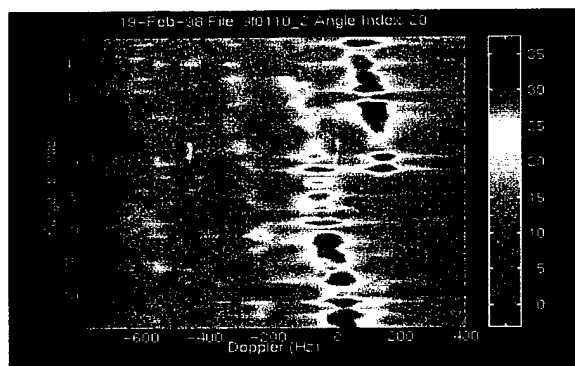
Figure 3-7b and 3-7c plots the RDI image for angle indexes 65 and 20, respectively. As expected, different portions of the clutter return are emphasized as the angle index is changed, with the emphasis moving toward the positive Doppler region as the pointing angle moves toward the nose of the aircraft (index 94: about 30° aft of broadside; index 65: broadside; index 20: about 45° fore of broadside).



(a) Angle Index = 94



(b) 65

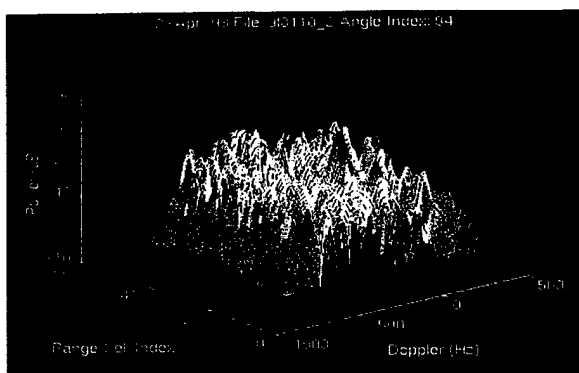


(c) 20

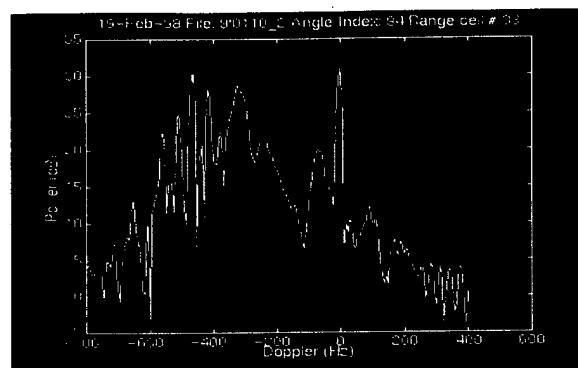
**Figure 3-7. RDI Plot, Acquisition #9-110**

Figure 3-8a is a 3D rendition of the plot in Figure 3-7a. Figure 3-8b is a cut through cell #33 in Figure 3-8a, showing that the MTS tones are noticeable even though corrupted by the clutter.

Figure 3-9 is the angle-Doppler plot for cell #31 of this acquisition. Note that the MTS signals have the same peak magnitude in cell 31 as in cell 33, and we happened to have produced the angle-Doppler plot for cell 31 rather than cell 33. Because of the range-foldovers, a smeared clutter ridge, rather than a well-defined clutter ridge, is observed. Note that there is no Doppler aliasing since the highest expected Doppler is less than 750 Hz for this acquisition, while the PRF is over 23 kHz.



(a) 3D RDI



(b) Cut Through Cell 33

**Figure 3-8. 3D RDI and Cell 33, Acquisition #9-110**

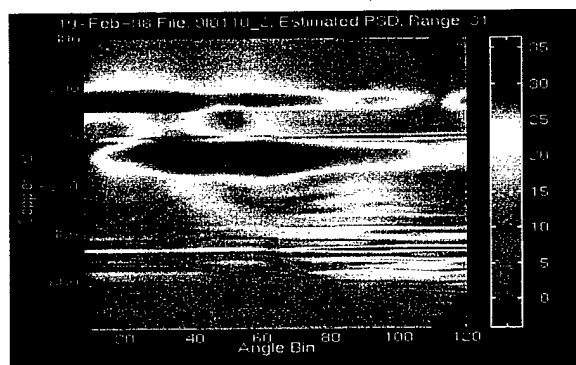
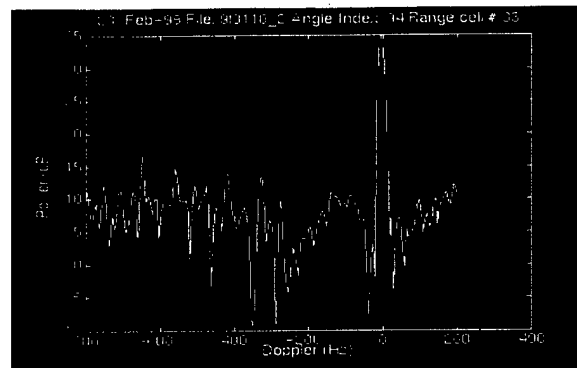
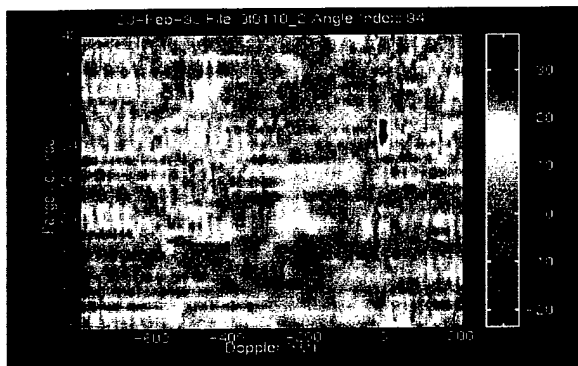


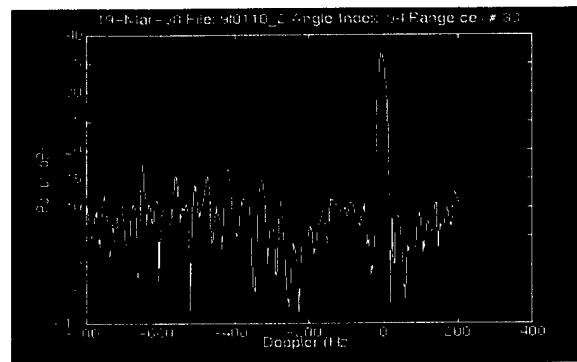
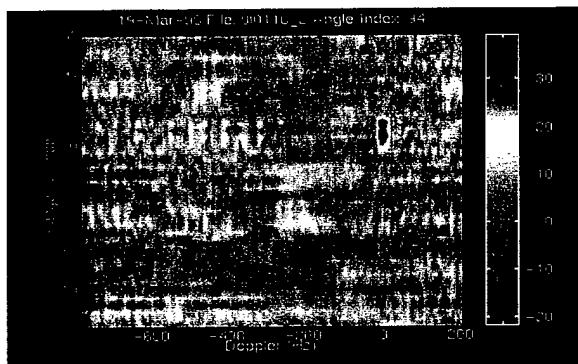
**Figure 3-9. Angle-Doppler Plot, Acquisition #9-110, Cell #31**

### 3.3.4 FTS Algorithm Applied to the Bistatic Acquisition #9-110

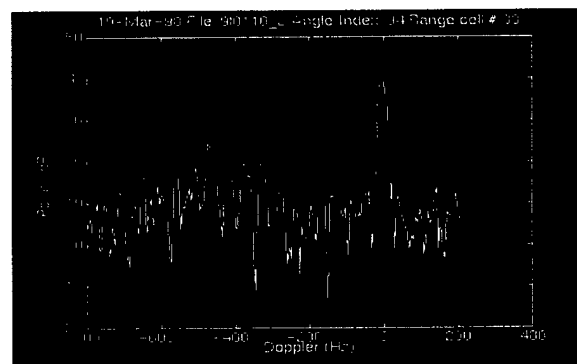
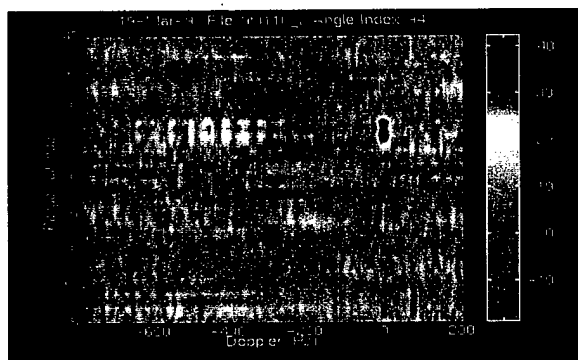
Figure 3-10 shows the result of applying the FTS algorithm to the bistatic acquisition #9-110. Only one row of the antenna, i.e., 11 channels, is used, supported by 22 range cells, and employing  $\pm 3$  guard cells. The support cells are nominally split into 11 fore and 11 aft, but when processing the lower or the higher ends of the range window, the split changes to accommodate the maximum number of cells available from the fore or aft while keeping the total support to 22 cells.



(a) All Pulses, CSR = 14.3 dB

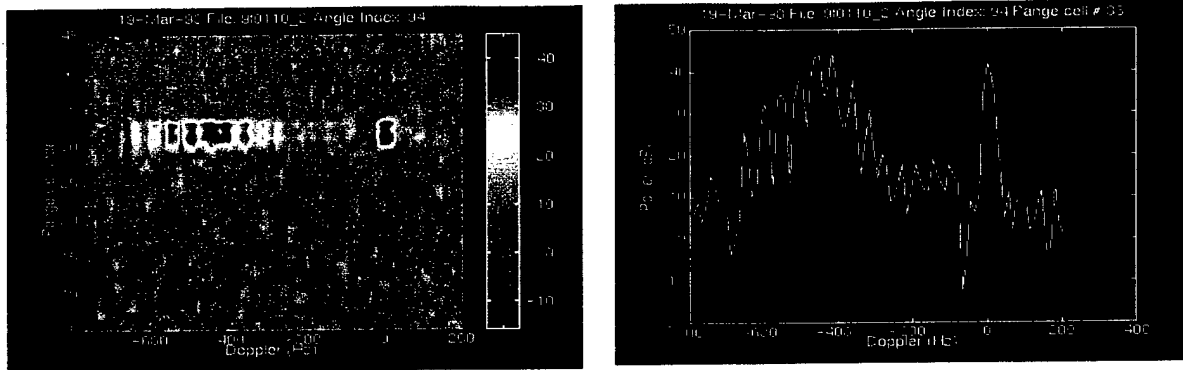


(b) Pulses > #162, CSR = 13.3 dB



(c) Pulses > #325, CSR = 11.93 dB

**Figure 3-10. FTS-Adapted RDI and Cell #33, Acquisition #9-110 (Channels: 11; Support Cells:  $\pm 11$ ; Guard Cells:  $\pm 3$ )**



(d) Pulses > #650, Clutter-free

**Figure 3-10. FTS-Adapted RDI and Cell #33, Acquisition #9-110 (Channels: 11; Support Cells:  $\pm 11$ ; Guard Cells:  $\pm 3$ ) (Concluded)**

Figure 3-10a shows the results when all the pulses are included, i.e., all the clutter is included. This produces a CSR of about 14.3 dB. It is observed that the adaptive processing has removed the clutter but has also suppressed the MTS tones that were obscured by the clutter, though the offset tone seems to have survived annihilation.

To check how the FTS would perform with different CSRs, we processed this acquisition, using different number of pulses. Figure 3-10b shows the result when pulses numbered higher than 162 are used. The CSR is about 13.3 dB. The tone cluster is still not clearly visible.

Figure 3-10c uses pulses higher than 325, resulting in a CSR of about 11.93 dB. The tones cluster is starting to become visible. Finally, Figure 3-10d disposes of all clutter by choosing only pulses #650 and up. With no clutter present, the tone cluster seems to have survived annihilation by the FTS adaptive process.

### 3.3.5 JDL mxn Algorithm Applied to the Bistatic Acquisition #9-110

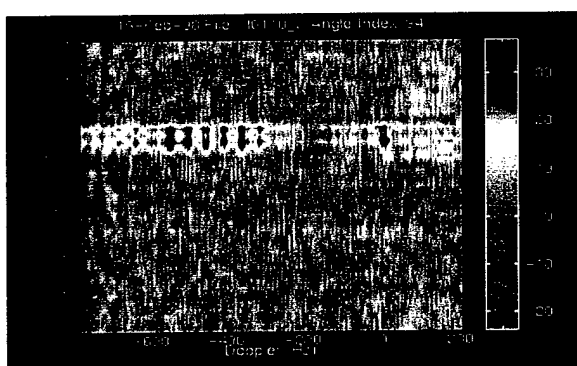
#### 3.3.5.1 JDL 3x3

Figure 3-11 shows the results of applying the JDL 3x3 algorithm to the acquisition #9-110. The JDL 3x3 algorithm uses 3 Doppler bins and 3 beams and we have chosen the test bin to be the central one in both the Doppler dimension and the beam dimension in these trials.

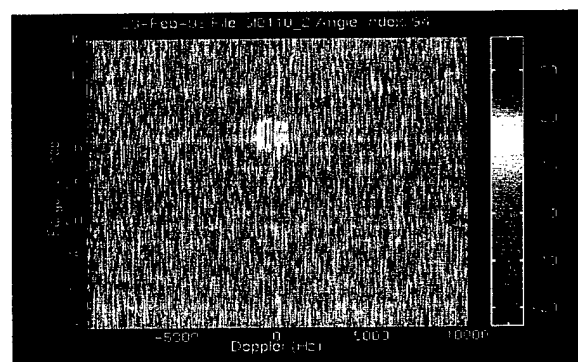
Figure 3-11a shows the adapted RDI plot for all the cells but with the Doppler extent limited to a range to show the MTS tones more clearly. All 22 channels and all 2408 pulses have been utilized. The sample support consists of 20 fore and 10 aft cells, i.e., a total of 30 cells, with  $\pm 3$  cells employed as guard cells. The 3x3 algorithm has 9 degrees of freedom and requires only a minimum of  $2 \times 9 = 18$  cells for support. When the test cell gets to one or the

other end of the 54-cell range window, the fore-aft split is changed to make use of as many cells as are available from the nearer end. The angle index is 94, i.e., the receive beam is pointed at the MTS. It is seen that all the tones are clearly visible. To assure ourselves that while the algorithm has suppressed the clutter without destroying the tones, it did not create artifacts in other regions of the total Doppler window, we have plotted the complete Doppler window in Figure b.

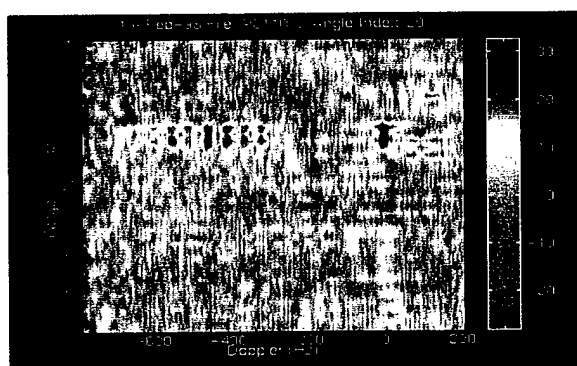
Figure 3-11a used the angle index 94, thus placing the main receive beam in the direction of the MTS. Would the performance degrade if the MTS tones come in through the sidelobes of the receive beam pattern? The complete Doppler window for this case is shown in Figure 3-11b to assure ourselves that no unexplained artifacts appear in the rest of the window.



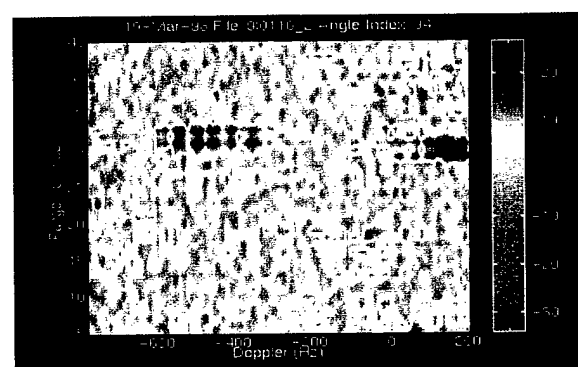
(a) All Pulses, Ang. Ind. 94, CSR = 14.3 dB



(b) Same as (a), Full Doppler Window



(c) All Pulses, Ang. Ind. 20, CSR = 14.3 dB



(d) Pulses  $\leq$  #1600, Ang. Ind. 94, CSR=16dB

**Figure 3-11. JDL 3x3 -Adapted RDI, Acquisition #9-110 (Channels: 22;  
Support Cells: -20,+10; Guard Cells:  $\pm$ 3)**

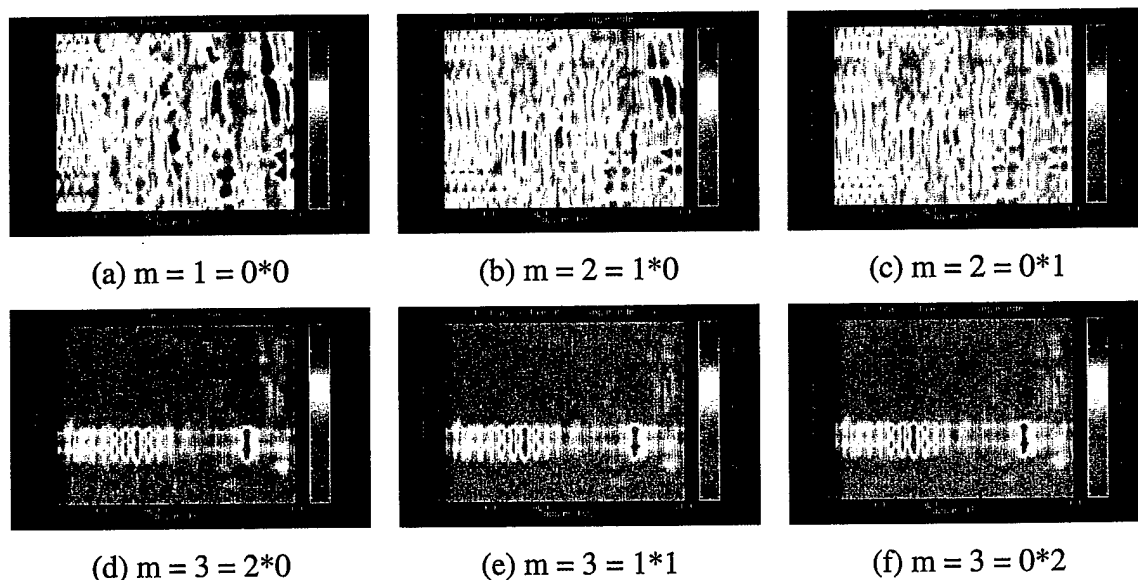
Figure 3-11c shows the performance with the angle index 20, where the main receive beam is pointed almost  $50^\circ$  away from the MTS. The tones are still clearly visible, though the clutter cancellation overall seems to be less.

In Figure 3-11a, all the 2,408 pulses were used, resulting in a CSR is about 14.3 dB. Figure 3-11d presents the results when the first 1600 pulses are used, resulting in a CSR of about 16 dB. The tones are still visible, though some artifacts beyond the offset tone now appear.

The above results were obtained with the JDL  $3 \times 3$  algorithm. We next present some results from this bistatic acquisition with other values of the degrees of freedom (DOF) of the JDL algorithm.

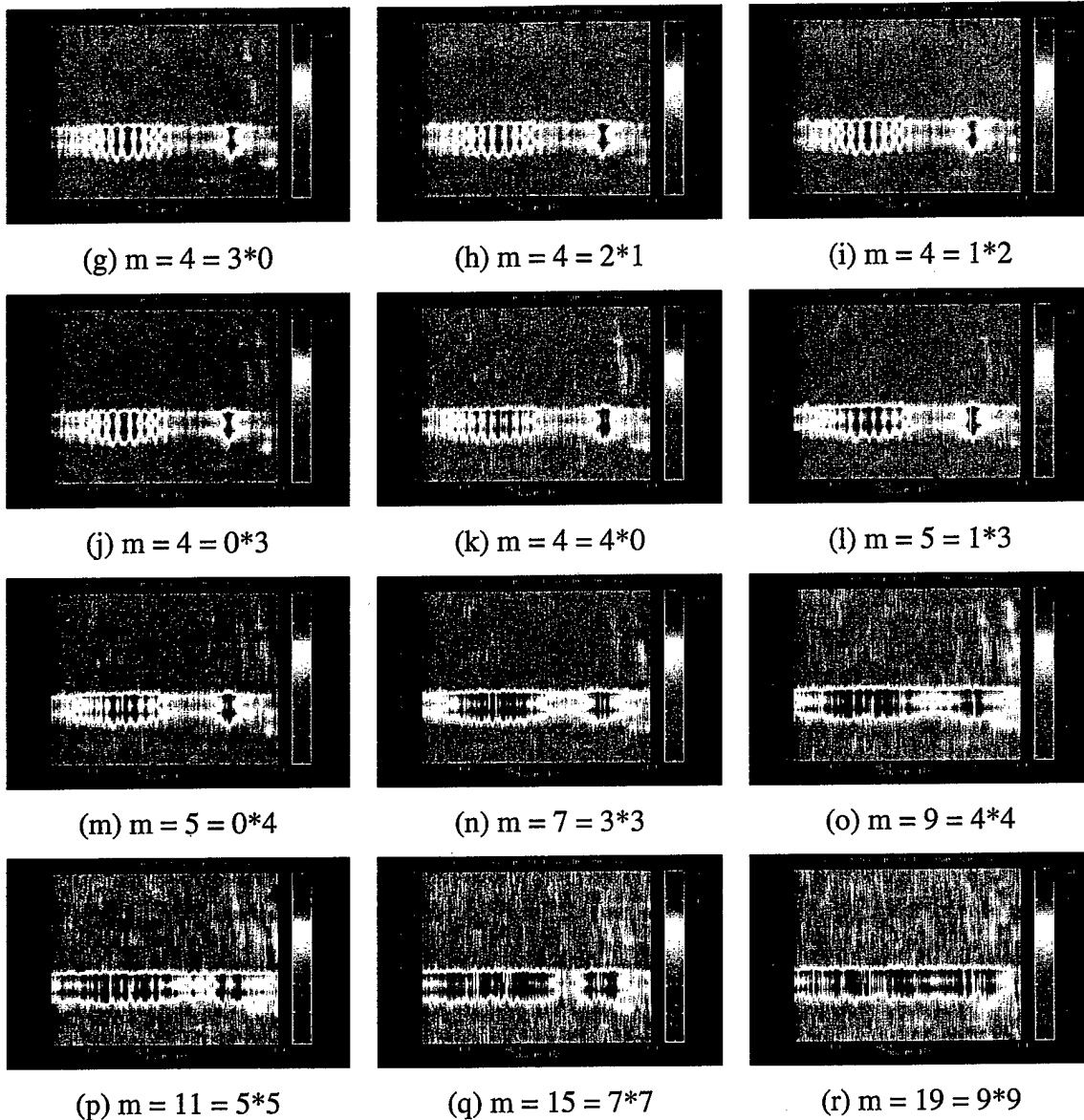
### 3.3.5.2 JDL $m \times n$

Figure 3-12 shows results of applying the JDL  $m \times 1$  algorithm, where different values for  $m$ , the DOF in the Doppler space, have been used, while holding  $n$ , the DOF in the beam space, to unity. As before, the cell support is 30, with  $\pm 3$  cells being used as guard cells. The angle index is 94, i.e., the receive beam is pointed at the MTS.



**Figure 3-12. JDL  $m \times 1$  -Adapted RDI, Acquisition #9-110 (Channels: 22; Support Cells: -20,+10; Guard Cells:  $\pm 3$ )**





**Figure 3-12. JDL mx1 -Adapted RDI, Acquisition #9-110 (Channels: 22;  
Support Cells: -20,+10; Guard Cells:  $\pm 3$ ) (Concluded)**

It is seen from Figure 3-12 that with a DOF of unity in the beam space, all DOF of 2 to about 7 in the Doppler domain seems to produce good performance. With higher DOF in the Doppler domain, the performance seems to degrade in the sense that the tones start to smear together though they still allow the particular cell to be 'detected' as containing the signal tones.

Figure 3-13 presents the cuts through range cell #33 of the JDL mx1 – adapted RDI plots in Figure 3-12.

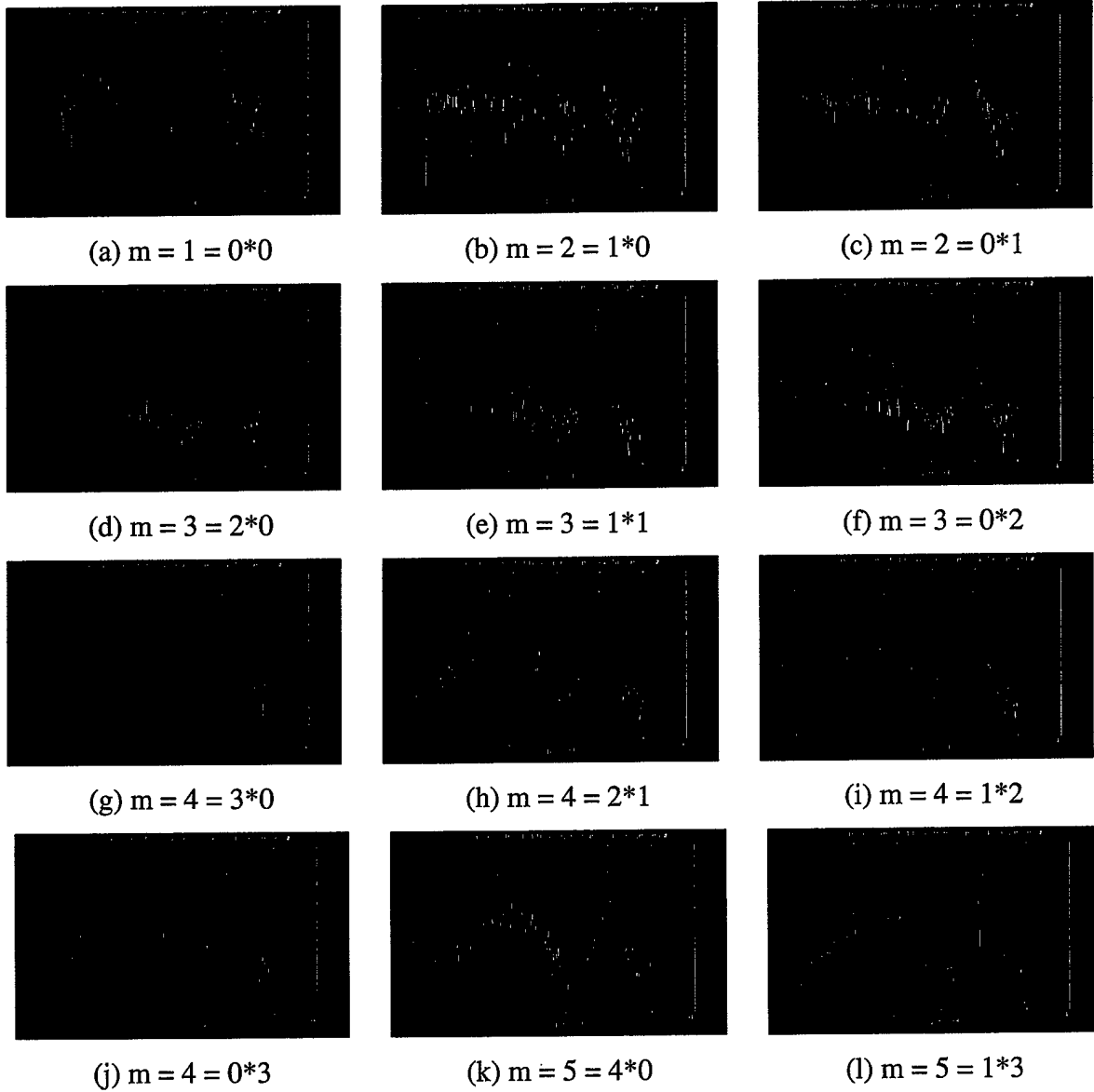


**Figure 3-13. JDL mx1 -Adapted Range Cell #33, Acquisition #9-110 (Channels: 22;  
Support Cells: -20,+10; Guard Cells:  $\pm 3$ )**

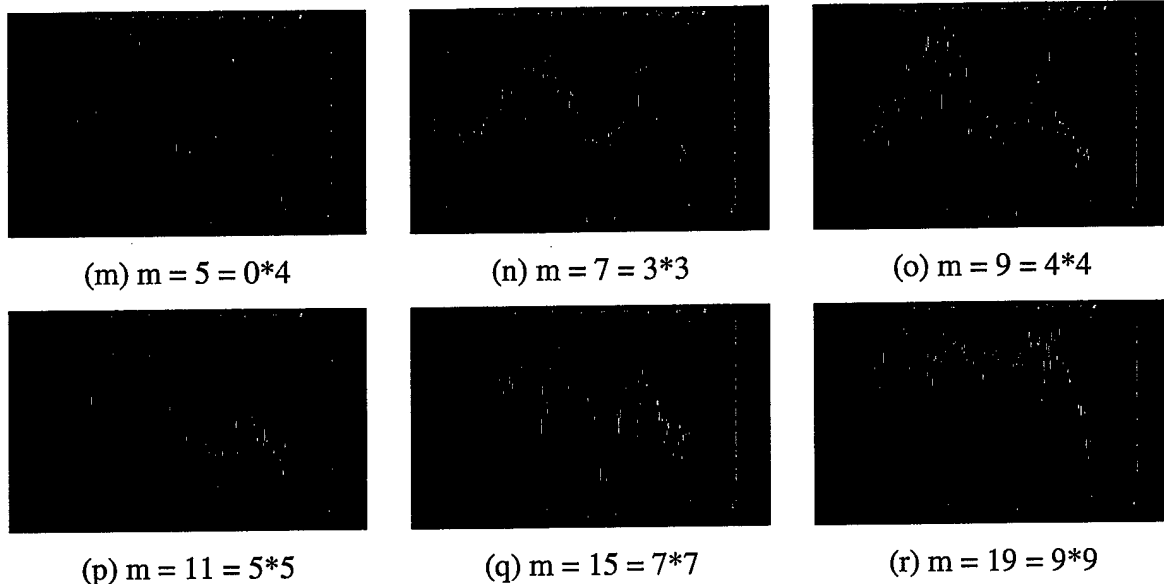


**Figure 3-13. JDL mx1 -Adapted Range Cell #33, Acquisition #9-110 (Channels: 22; Support Cells: -20,+10; Guard Cells:  $\pm 3$ ) (Concluded)**

From the plots in Figure 3-13, it appears that JDL with the DOF 4x1, i.e., 4 degrees of freedom in the Doppler space with the DOF limited to one degree of freedom in the beam space, gives the best performance in terms of clutter suppression and clarity of individual tones.

Now we examine the effect of additional degrees of freedom in the beamspace, with the results being shown in Figure 3-14. With the DOF in Doppler limited to unity, the DOF in the beam space is varied from 2 to 23 and it is found that none of the cases produce an acceptable result.

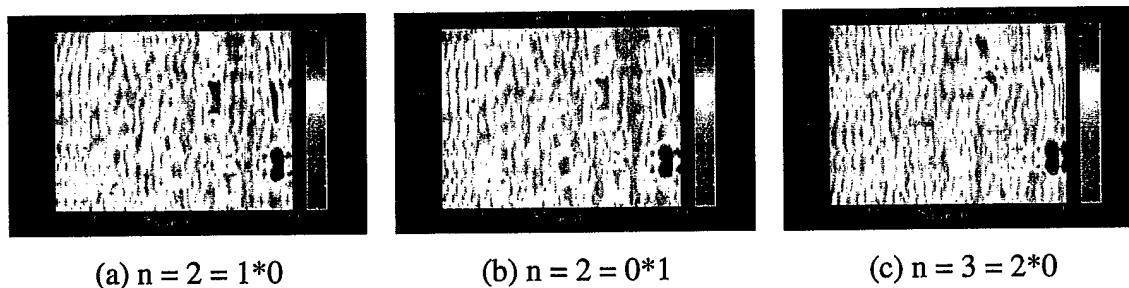


**Figure 3-14. JDL 1xn -Adapted RDI, Acquisition #9-110 (Channels: 22; Support Cells: -20,+10; Guard Cells:  $\pm 3$ )**

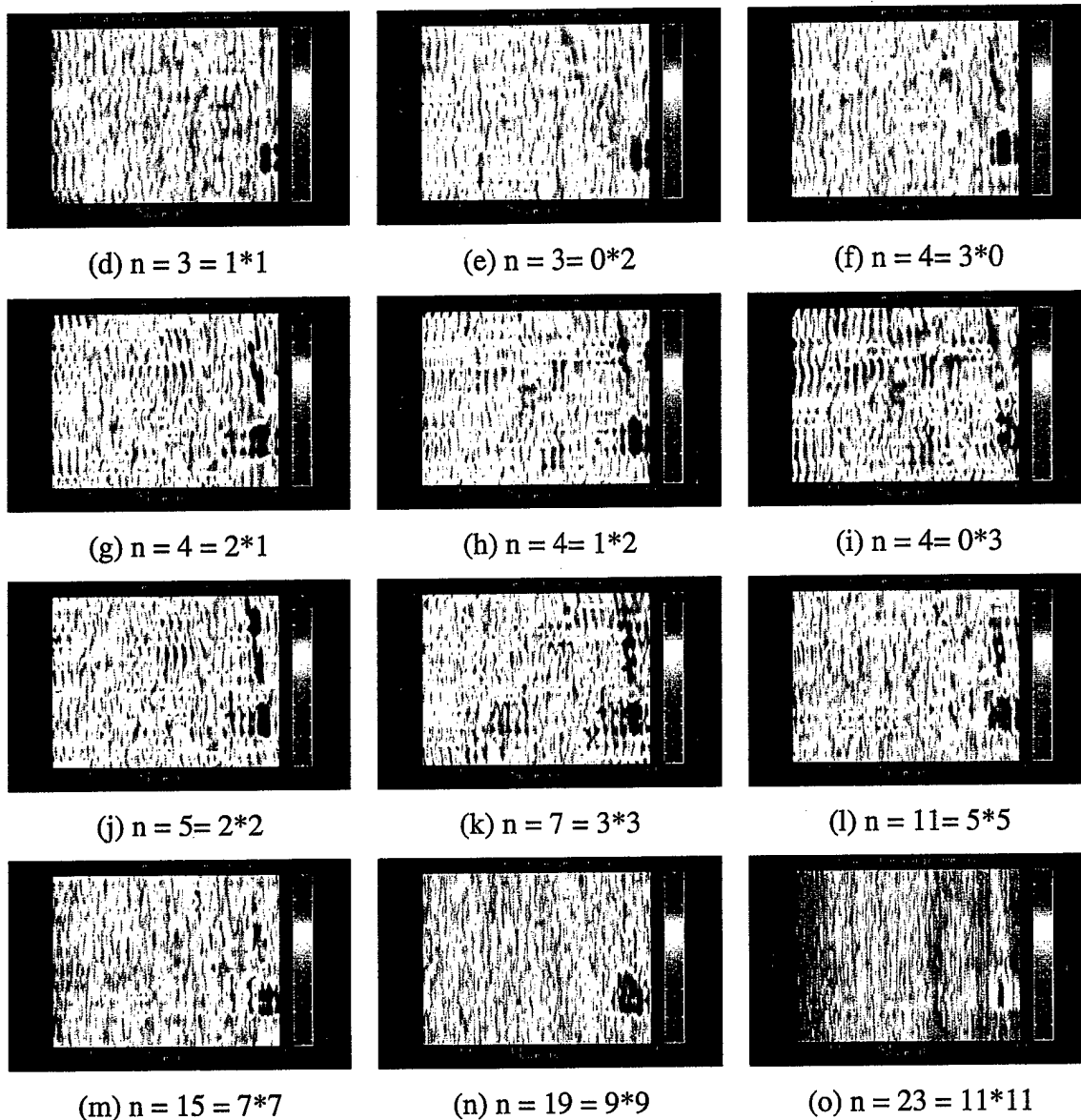
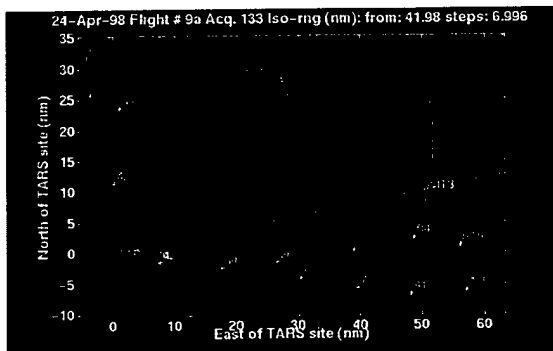


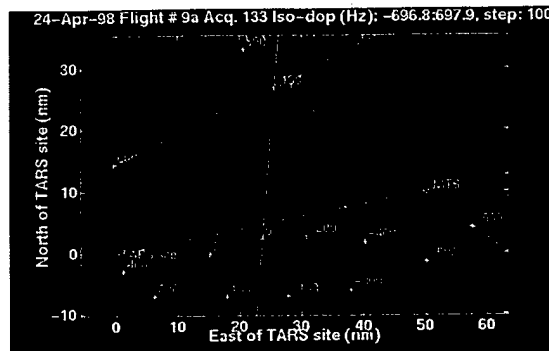
**Figure 3-14. JDL 1xn -Adapted RDI, Acquisition #9-110 (Channels: 22;  
Support Cells: -20,+10; Guard Cells:  $\pm 3$ ) (Concluded)**

### 3.4 Acquisition #9-133

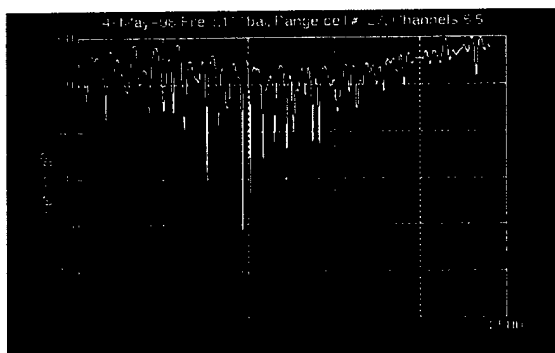
Figure 3-15 shows some of the results of applying STAP algorithms to the acquisition #9-133. While we were quite successful with acquisition #9-110, we were not able to see even the offset MTS tone in acquisition #9-133.



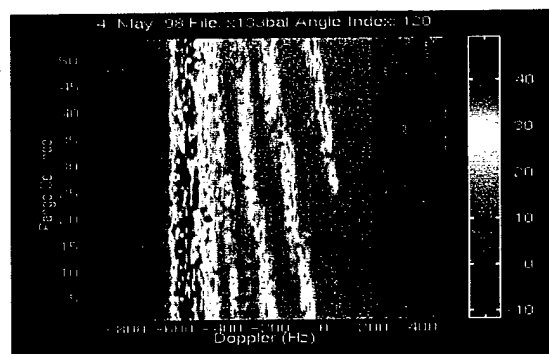
(a) Iso-Bistatic Range Contours



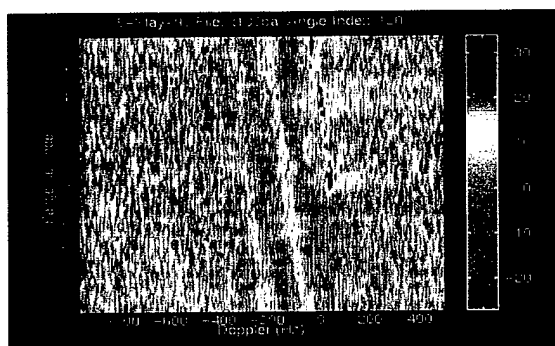
(b) Iso-Bistatic Doppler Contours



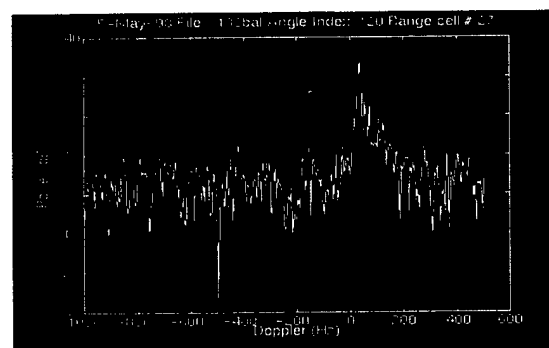
(c) Signal vs Pulse #, Cell #27, Channel #5



(d) Unadapted RDI



(e) JDL 3x3 Adapted Range-Doppler



(f) Cut Through Cell #27 in (e)

**Figure 3-15. Acquisition #9-133**

In this acquisition, the TARS transmitter was on during the whole time of recording and the effective CSR is probably of the order of 20 dB. Unlike acquisition #9-110, we did not have the option of reducing the effective CSR by considering only a portion of the acquisition.

The iso-bistatic range contours clearly show that several foldovers in range are expected and this is clearly seen in the RDI plot. The iso-bistatic Doppler plot indicates that the Doppler shift for the MTS is expected to be about  $-600$  Hz. Thus the  $500$  Hz offset tone should appear at about  $-100$  Hz, but unlike acquisition #9-110, there is no clear indication of this tone in the unadapted RDI plot in this case. Thus there is no indication as to which, in fact, if any, cell contains the MTS signal. However, there is no record that the MTS had stopped transmitting and we have to assume that the signal is present in one of the cells.

The indicated angle index for the MTS in this acquisition was 120 and we applied a JDL  $3 \times 3$  adaptive clutter cancellation algorithm using this index, but the results still did not reveal any of the tone cluster. A strong residue is observed in cell #27, and we show a cut through this cell in 3-15f, but we see no trace of the other tones. Figure 3-15c plots the signal strength versus the pulse number in this cell, and we find that the TARS was on all the time during the recording, probably resulting in a CSR of about  $20$  dB, going by the MTS signal level seen in acquisition #110. At this CSR, the STAP algorithm annihilates the tones along with the clutter.

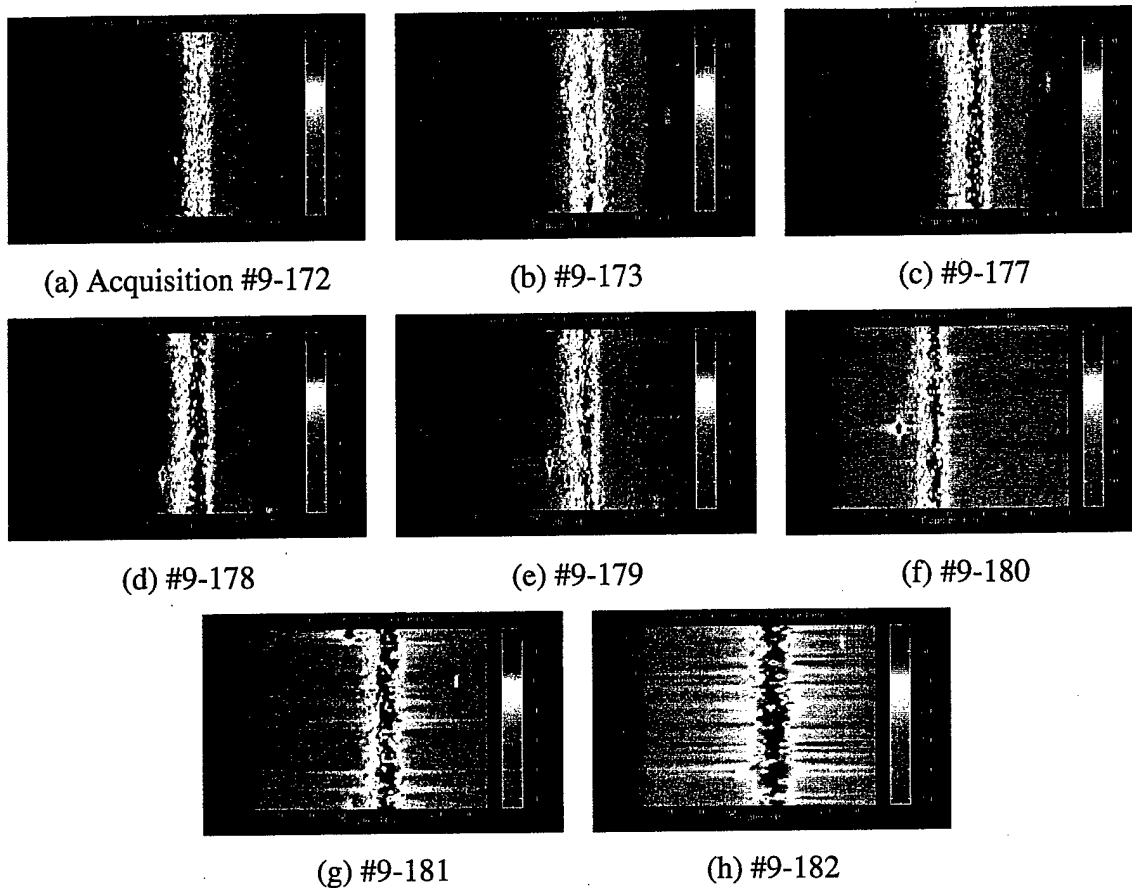
### **3.5 Pseudomonostatic Acquisitions**

From the flight path in Figure 3-2 and the bistatic angles plotted in Figure 3-4c, it appears that the bistatic angle reaches about zero degrees at acquisition 175, and the bistatic angles are fairly small for all the acquisitions between 170 and 180. These are the so-called pseudomonostatic acquisitions. In this subsection, we present some results from these acquisitions.

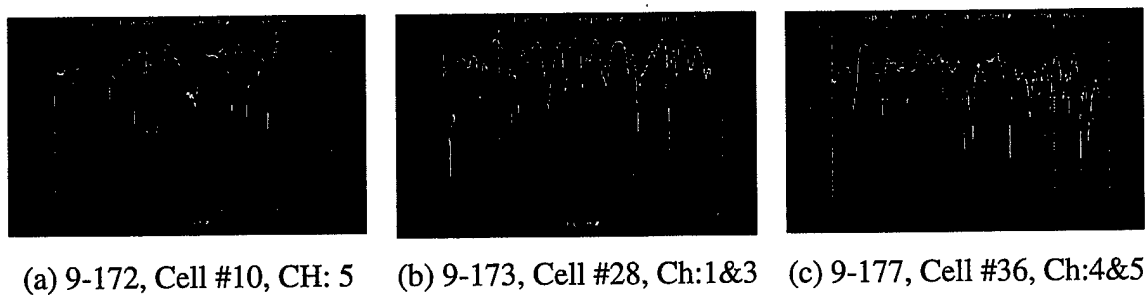
#### **3.5.1 Acquisitions 172, 173, 177-182**

Figure 3-16 shows the unadapted RDI plots for the acquisitions 172, 173, 177-182. In all these acquisitions, the offset MTS tone is clearly visible while the tone cluster is well hidden by the ground clutter. Notice what appears to be a separate, large moving object that appears at a Doppler of about  $-300$  Hz.

Figure 3-17 shows the signal versus pulse for the respective cells containing the MTS tones. The channel numbers are also indicated but the traces are similar for any channel. In acquisitions 172, 173, 177, and 178, the TRS radar is on during the whole recording time, while it is for parts of the time in acquisitions 179-182.



**Figure 3-16. Unadapted RDI Plots for Several Pseudomonostatic Acquisitions**



**Figure 3-17. Signal Versus Pulse Number for the same Pseudomonostatic Acquisitions as in Figure 3-16**

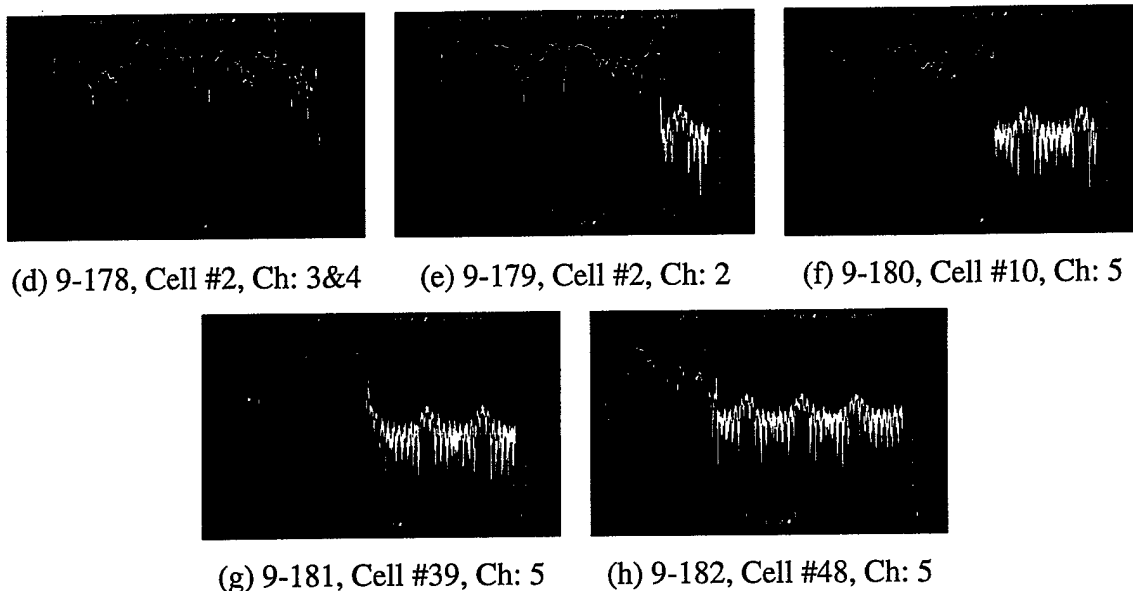


**Figure 3-17. Signal Versus Pulse Number for the same Pseudomonostatic Acquisitions as in Figure 3-16 (Concluded)**

### 3.5.2 Adaptive Processing of Pseudomonostatic Acquisition #9-172

From Figure 3-17, it is clear that in acquisition #9-172, the TARS is on all the time and thus the CSR is expected to be high, and per our experience so far, we do not expect the STAP algorithms to be able to reveal the MTS tone cluster. Nonetheless, we tried the JDL 3x3 and the FTS algorithms, with various angle indexes and the results are presented in Figures 3-18 and 3-19, respectively.

It is seen that neither the JDL nor the FTS algorithms are able to recover the MTS tone-cluster in range cell #10 from the clutter, though the offset tone, at a Doppler of about 350 Hz, is seen at almost all angles of index. It is especially clear at the angle index of 60, which is about the direction of the MTS in this acquisition. The object in range cell 17 and a Doppler of about -200 Hz, seen in the unadapted RDI plots also, is still clearly visible, but there now appears to be a tail to it. It is interesting to conjecture that this represents road traffic, but we do not have enough corroborative information to verify this conjecture at this time.

There is also a strong return in cells 10-12, which was not noticed in the unadapted RDI plots, probably because of the limited dynamic return we had selected to view those plots. In any case, after the clutter suppression, this object is clearly visible.



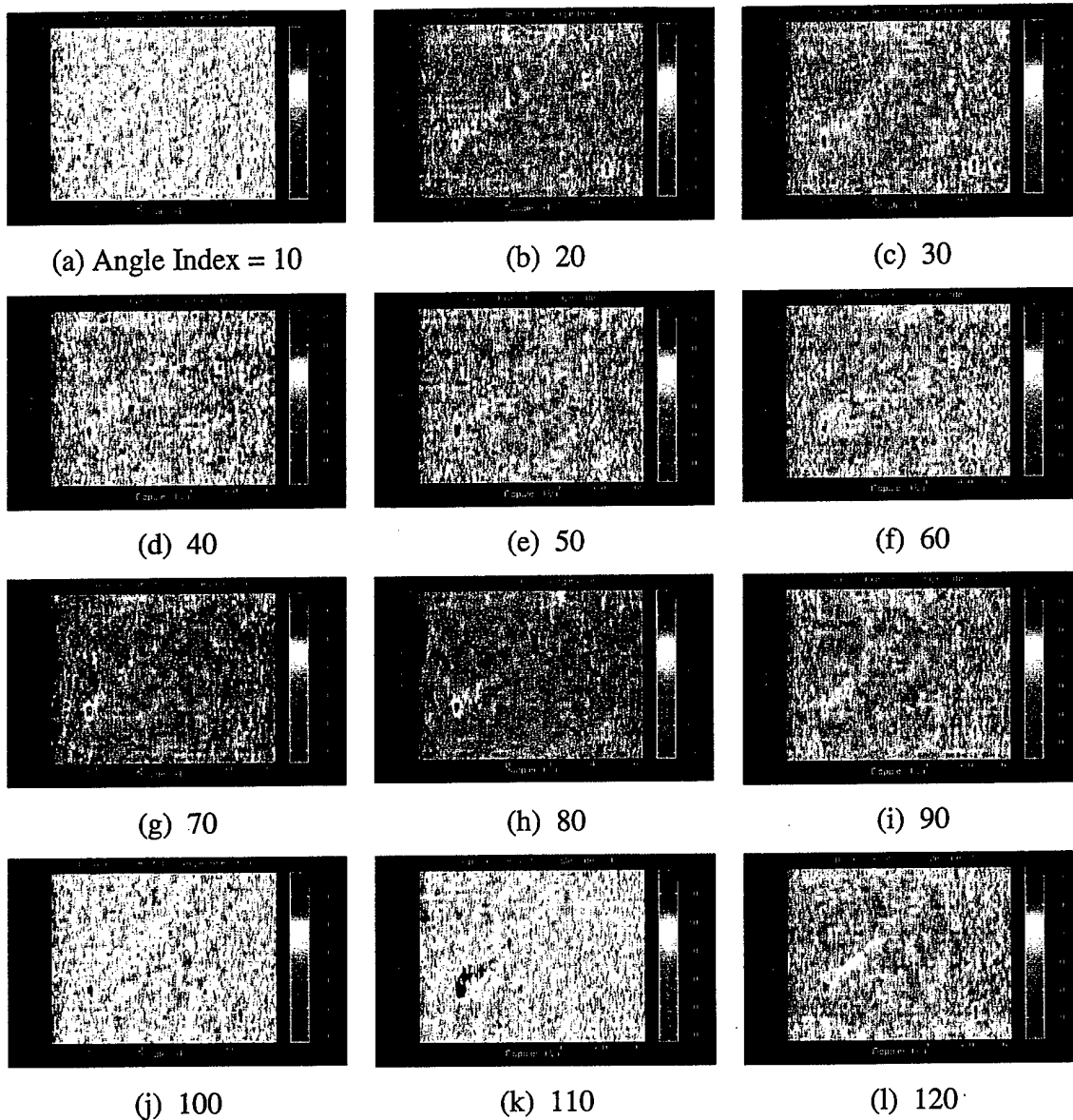


**Figure 3-18. JDL 3x3 -Adapted RDI, Acquisition #9-172 (Channels: 22; Support Cells: -20,+10; Guard Cells:  $\pm 3$ )**

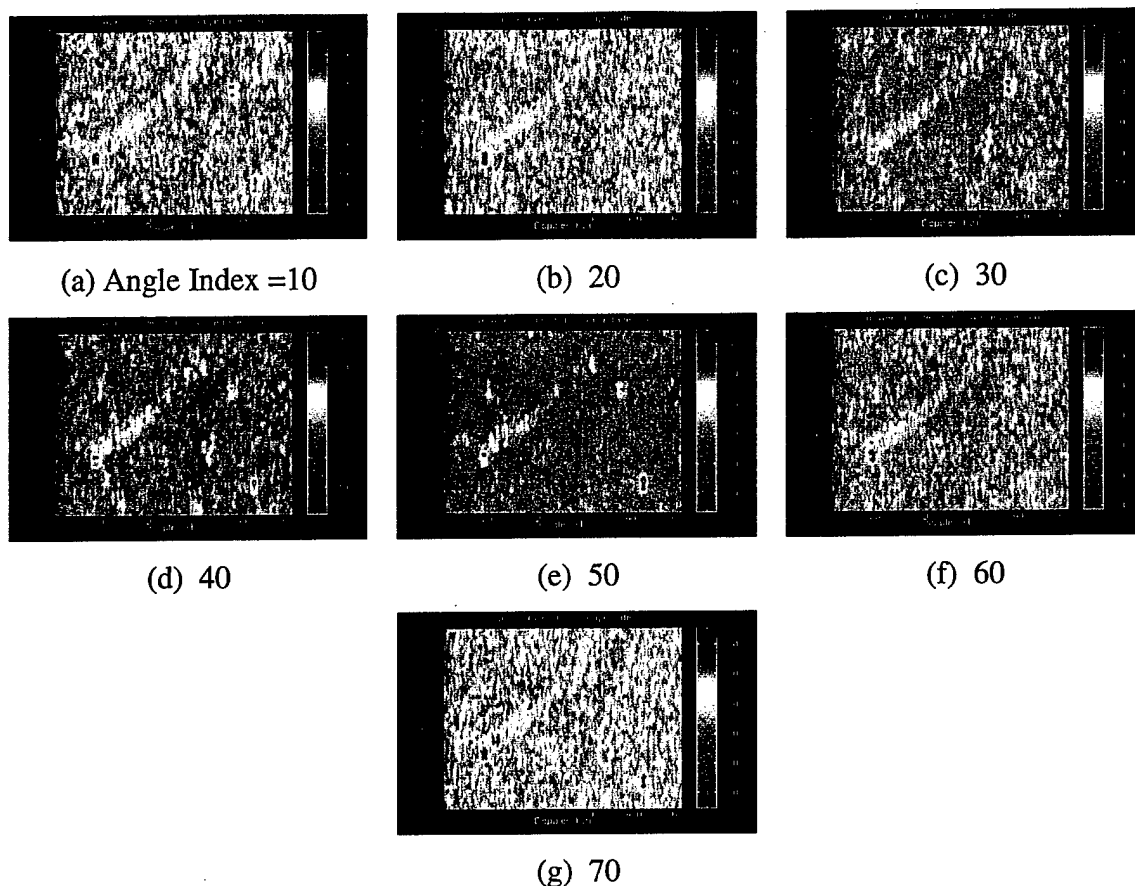


**Figure 3-19. FTS -Adapted RDI, Acquisition #9-172 (Channels: 11;  
Support Cells: -11,+11; Guard Cells:  $\pm 3$ )**

### 3.5.3 Adaptive Processing of Pseudomonostatic Acquisition #9-180

It was seen in Figure 3-17f that in acquisition #9-180, the TARS radar is on for only a fraction of the acquisition, and, therefore, it is possible to control the effective CSR by processing different portions of the acquisition.

Tables 3-5 and 3-6 list some parameters relevant to this acquisition. Note the small bistatic angle.

Figure 3-20 comprises several plots pertaining to acquisition #9-180. Figure 3-20a shows the flight path. Figure 3-20b shows the iso-bistatic range contours, indicating the many range foldovers. Note the small bistatic angle.

**Table 3-6. Flight and Data Collection Parameters on Acquisition #9-180**

Parameter	Value
TARS-BAC Range	27.2 nm
Roll Angle	-0.63°
Pitch Angle	5.2°
Crab Angle	6.5°
Receive Azimuth	270°
PRF	23,148 Hz

**Table 3-7. MTS Parameters on Acquisition #9-180**

Parameter	Value
TARS-MTS Range	51.67 nm
BAC-MTS Range	24.61 nm
Bistatic Range	76.28 nm
Bistatic Angle	4.3°
Azimuth	273.8°
Radial Velocity	-68.85 knots
Doppler Shift	146.4 Hz

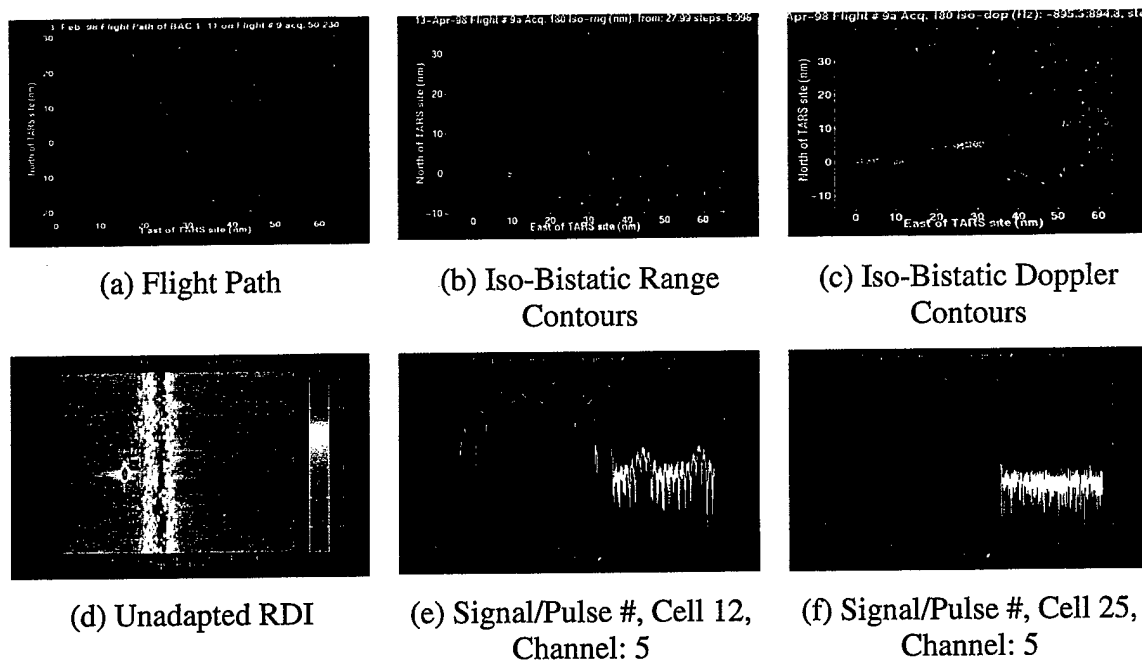
Figure 3-20c shows the iso-bistatic Doppler contours, indicating that the computed MTS Doppler is about 146 Hz. Apparently the recorded crab angle is not quite correct, since the radar data indicates the MTS Doppler to be actually about -150 Hz.

Figure 3-20d shows the unadapted RDI plot using all the pulses and the angle index 65, showing the offset MTS tone in range cell 10-12 and at a Doppler of about 350 Hz, and a strong return in cell 25 and at a Doppler of about -350 Hz.

Figure 3-20e plots the signal versus the pulse number in cell 12 and channel 5. It is seen that the TARS is on for the first 1,500 pulses only; beyond that only the MTS is transmitting. As in other acquisitions, the clutter return is about 20 dB above the MTS signal.

Figure 3-20f plots the signal in cell 25, which contains an object distinct from the ground clutter. There is return from this moving object to about pulse # 1,500, i.e., while the TARS

transmitter is on; beyond that, only receiver noise is recorded in this cell. Comparing this figure with Figure 3-20e, it is observed that the returns from the moving object are about 7 dB stronger than the clutter returns and, further, the MTS signals are also about 7-8 dB stronger than the receiver noise.



**Figure 3-20. Pseudomonostatic Acquisition #9-180**

It is of some interest to see how the RDI plot changes as the receive angle is varied; the illumination is determined by the TARS beam and is fixed for this acquisition. This variation is shown in Figure 3-21. At angle indexes near 65, i.e., broadside, the MTS offset tone is visible. The RDI for this angle is also shown in 3D (Figure 3-21g).

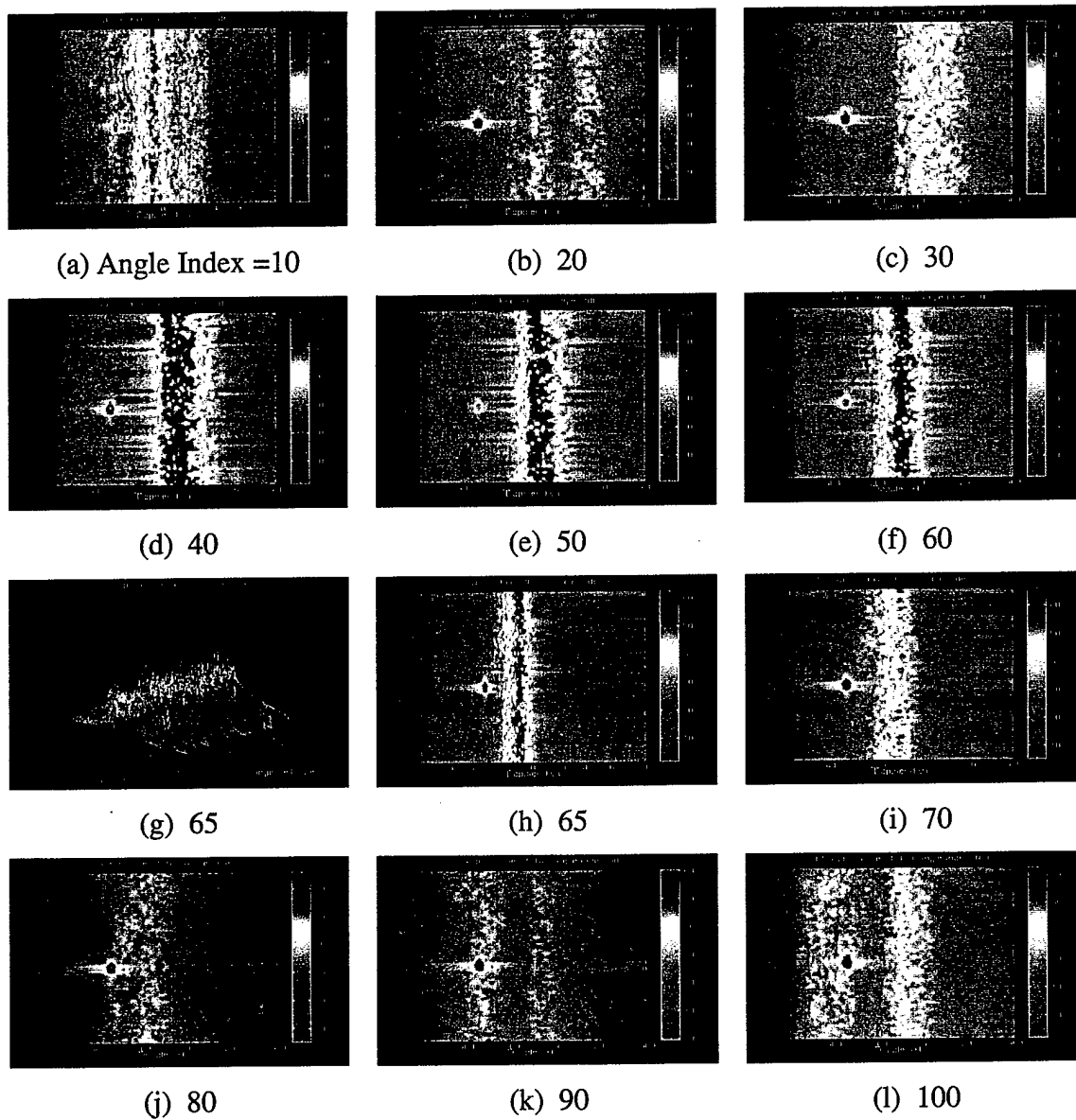


**Figure 3-21. RDI at Various Angle Indexes, Acquisition #9-180**

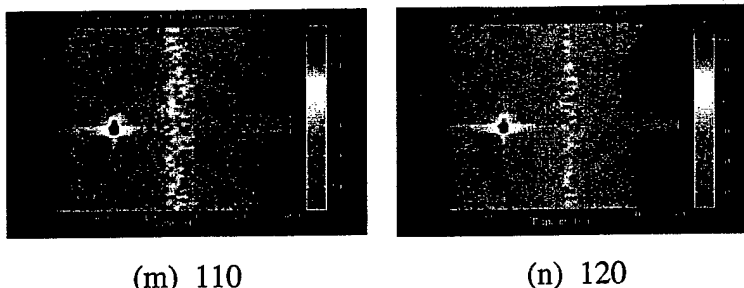


**Figure 3-21. RDI at Various Angle Indexes, Acquisition #9-180 (Concluded)**

At all angle indexes, the strong target in cell 25 is clearly visible, but its true azimuth is not obvious. Whenever the mainlobe or one of the sidelobes of the receive beam coincides with the direction of illumination, the clutter appears strong, while it appears weak whenever a null in the receive beam coincides with this illumination. If we had carefully studied the variation of this signal with the receive beam pointing angle, it would have been possible to estimate the azimuth of the object with respect to the MCARM antenna. With the azimuth estimated, one can compute the expected Doppler of a stationary object at that azimuth. By comparing the observed Doppler with the computed Doppler for a stationary object at that azimuth, one can possibly judge if this is a moving or a stationary object. We have not gone through this exercise here.

Figure 3-22 shows the unadapted and the adapted RDIs as the amount of clutter is varied. The first column shows the unadapted RDI, the middle column the JDL\_3x3-adapted and the last the FTS-adapted RDI, respectively. The results in the first row are for the MTS-only case. Here we have included only pulses numbered higher than 1,500, thus eliminating all clutter returns. Note that this also eliminates any returns from the object in range cell 25. The CSR for this case is 0. The unadapted RDI clearly shows all the MTS tones, and so do the adapted RDIs. Note that we are using only about 900 pulses and thus the frequency resolution is not as high as we can get with all 2,408 pulses. Note also that the unadapted and the JDL-adapted RDIs are plotted over the frequency span of -600 Hz to 400 Hz, while the FTS result is plotted over the span -400 Hz to 600 Hz simply because the results were obtained independently at different times. Both the adapted patterns also retain the strong return in cell #25, but it appears to be smeared in Doppler.

The second row, row b, uses pulses higher than #1,400, resulting in a CSR of approximately 10 dB. The unadapted RDI displays the presence of clutter, but not enough to completely mask the MTS tones. Both the JDL and the FTS algorithms suppress the clutter without destroying the MTS tones.

In row c, pulses higher than #1,300 are used, producing an effective CSR of about 12.6 dB. The unadapted RDI shows that the clutter is strong enough to have almost masked the MTS tones. The JDL-adapted RDI reveals the MTS tones as well as the other large object. The FTS-adapted RDI is able to reveal the MTS offset tone, but not the other tones in

the cluster. The other large object is observable but is completely smeared in Doppler. The results in row d, with a CSR of about 14 dB, are about the same as in row c.

Row e has a CSR of about 15.5 dB. Now even the JDL fails to reveal the MTS cluster of tones, though the offset tone is still clearly visible. The results with a CSR of about 16.4 dB, in row f, are not that much different. The results for the case when all the 2,408 pulses are used, yielding a CSR of about 18 dB, though not shown here, are not much different either.

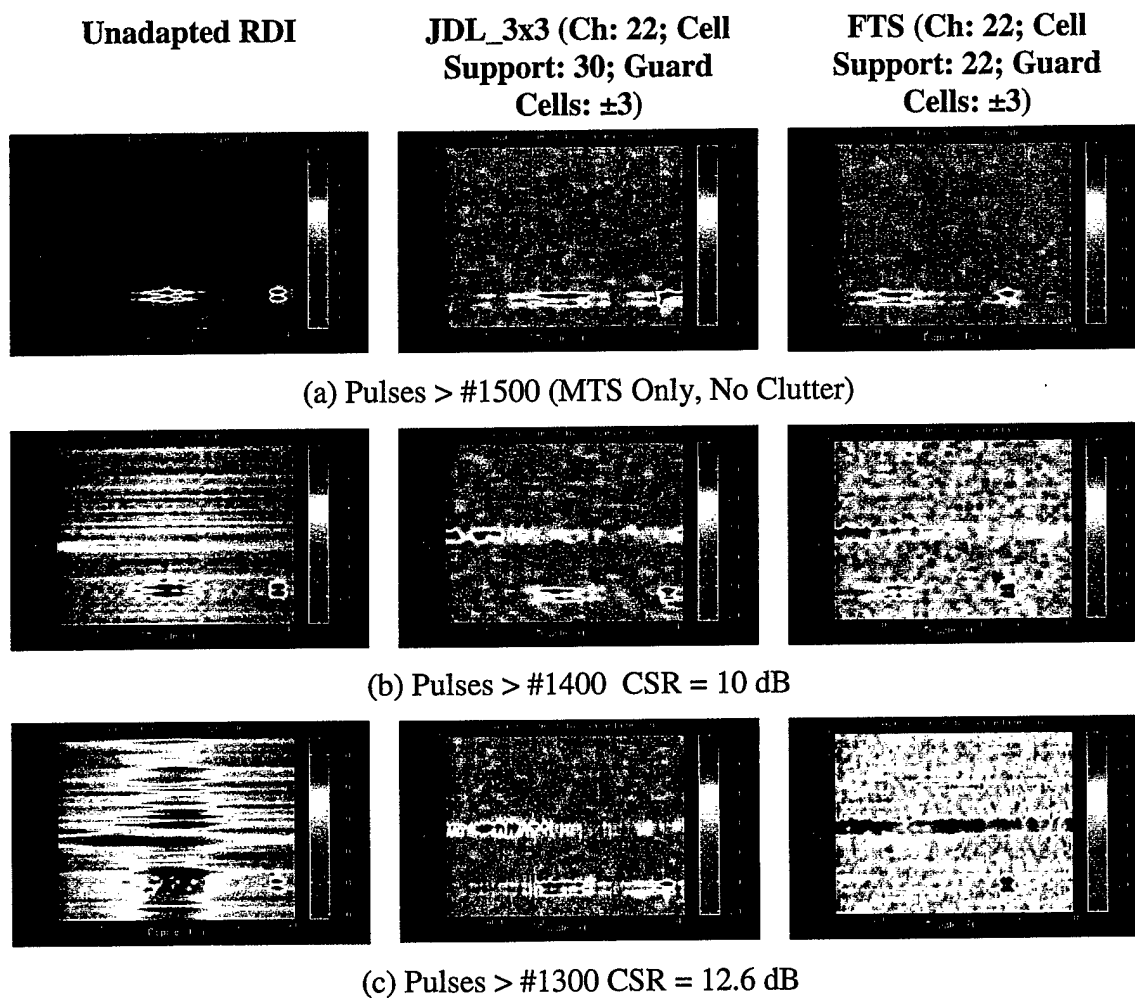
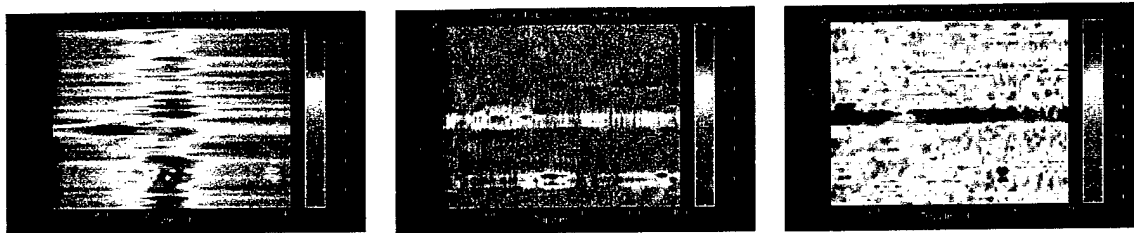
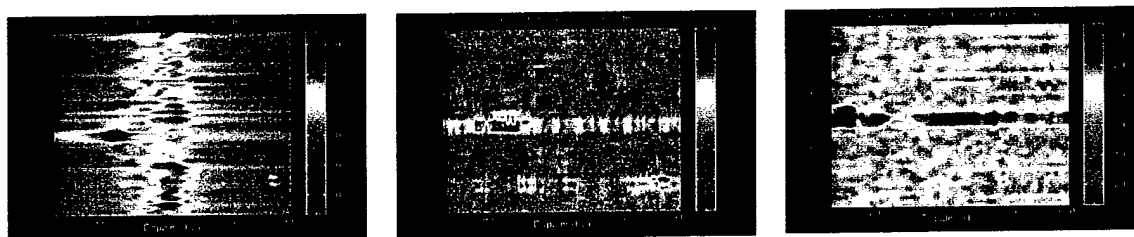


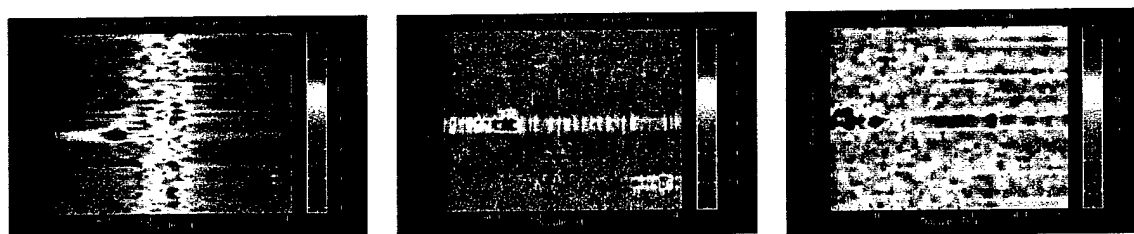
**Figure 3-22. STAP-Processing Acquisition #9-180 with Varying CSRs**



(d) Pulses > #1200 CSR = 14 dB



(e) Pulses > #1000 CSR = 15.5 dB

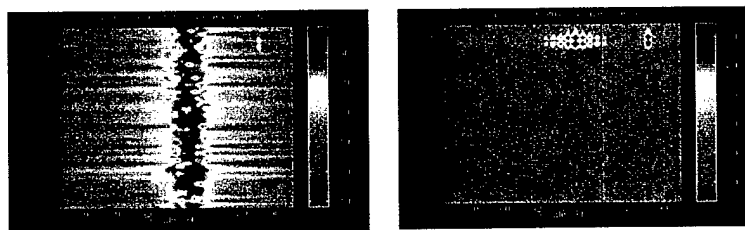


(f) Pulses > #800 CSR = 16.4 dB

**Figure 3-22. STAP-Processing Acquisition #9-180 with Varying CSRs (Concluded)**

### 3.5.4 Adaptive Processing of Pseudomonostatic Acquisition #9-182

Figures 3-23 plots the RDI of acquisition #9-182.



(a) With clutter

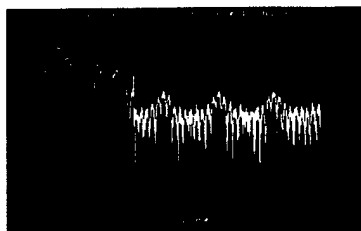
(b) Without clutter

**Figure 3-23. RDI of Pseudomonostatic Acquisition #9-182**

The presence of the line at 0 Doppler frequency in Figure 3-23b is not easily explained.

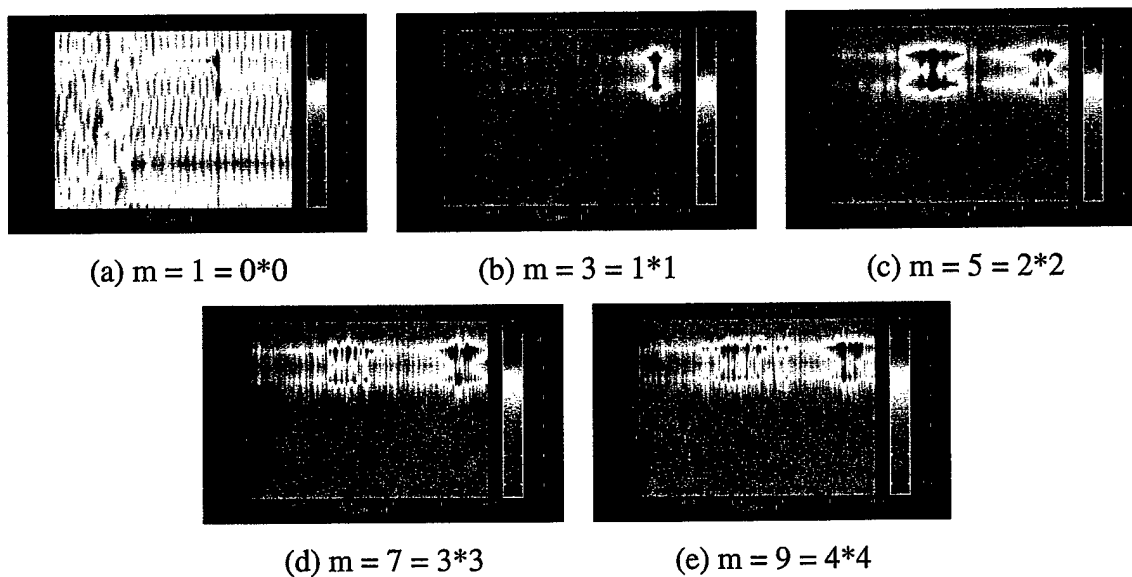


Figure 3-24, plots the signal strength in cell #48. Compared to acquisition #9-180, this has a shorter duration of clutter. As in the other acquisitions, the clutter return is about 20 dB stronger than the MTS signals.



**Figure 3-24. Signal Strength Versus Pulse Number in Pseudomonostatic Acquisition #9-182**

The results of applying the JDL  $(m_1 + 1 + m_2) \times 1$  algorithm to the whole CPI, with various values of  $m_1$  and  $m_2$ , are shown in Figure 3-25. We have not shown a cut through cell #48, but it is apparent that the JDL  $(2 \times 2) \times 1$ , i.e., JDL  $5 \times 1$ , gives the best result.



**Figure 3-25. JDL  $m \times 1$  -Adapted RDI, Acquisition #9-182 (Channels: 22; Support Cells: 20,+10; Guard Cells:  $\pm 3$ )**

The results of applying the JDL  $1 \times (n_1 + 1 + n_2)$  algorithm to the whole CPI, with three values of  $n_1$  and  $n_2$ , are shown in Figure 3-26. Here the DOF in the frequency domain is limited to unity and in all cases, the performance is very poor. Clearly, the ample DOF in the look direction does not compensate for the limited DOF in the frequency domain.

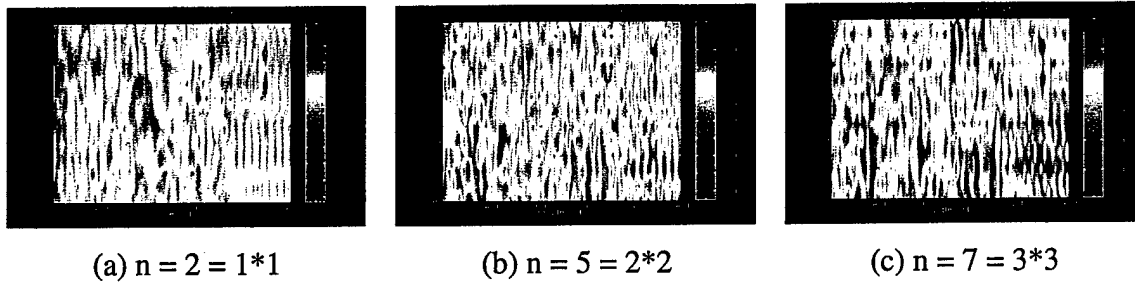


**Figure 3-26. JDL  $1 \times n$  -Adapted RDI, Acquisition #9-182 (Channels: 22; Support Cells: -20,+10; Guard Cells:  $\pm 3$ )**

In Figure 3-27, we compare the results of increasing the DOF in the look direction from 1 to 3 for three different values of DOF in the frequency domain, namely 3, 5 and 7.

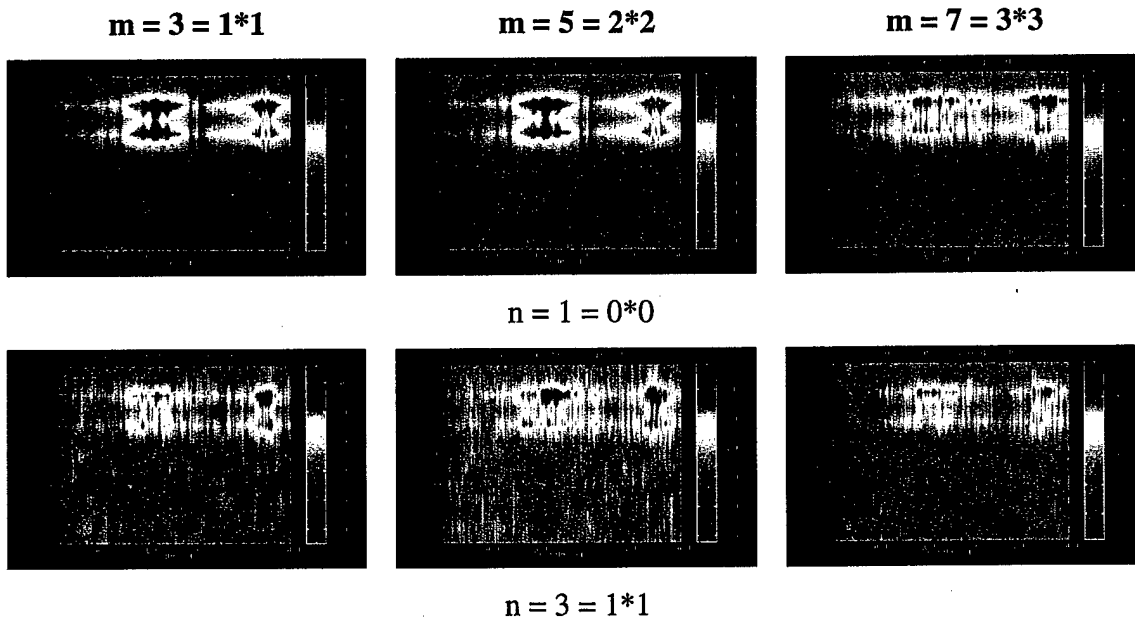


**Figure 3-27. Comparing JDL  $m \times 1$  and JDL  $m \times 3$  -Adapted RDI, Acquisition #9-182 (Channels: 22; Support Cells: -20,+10; Guard Cells:  $\pm 3$ )**

From these results, it appears that the increase in the DOF in the look direction only makes the performance worse! Though we have not verified these results in each and every CPI, it seems obvious that performance is not necessarily improved by arbitrarily increasing the DOF in the frequency and the spatial domains.

### 3.6 Wide-Bistatic-Angle Acquisitions

It is of great interest to see what happens to the bistatic clutter returns at large bistatic angles. Figure 3-28 displays the RDI for acquisition #92, where the bistatic angle is close to  $150^\circ$  using five different look angles.

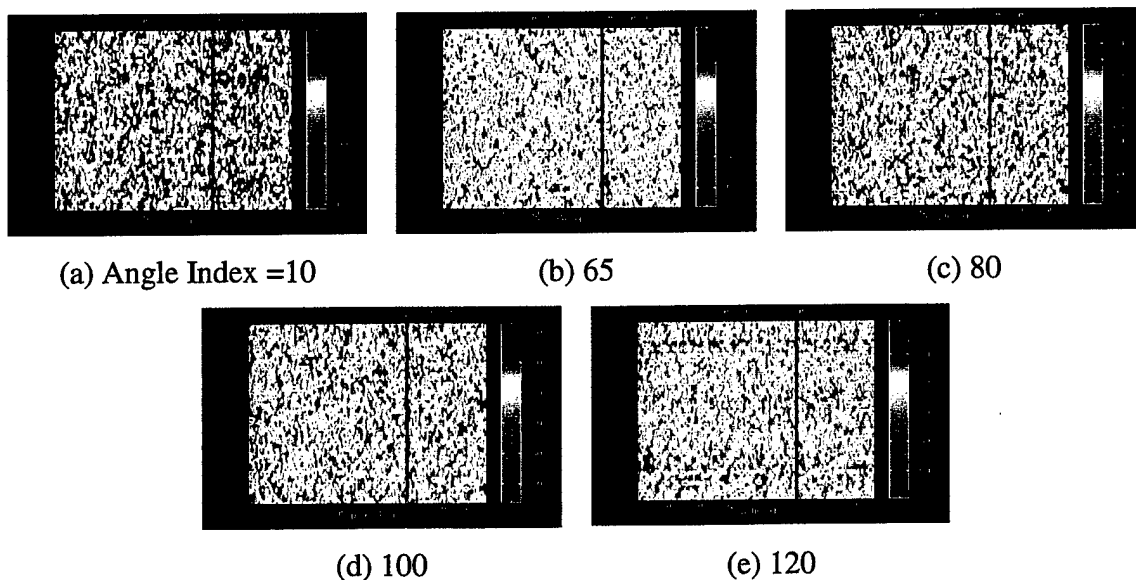


**Figure 3-28. RDI, Wide-Bistatic Angle Acquisition #92**

Figure 3-29 shows the RDI for acquisition 9-93. For some reason, neither of these acquisitions appears to have recorded any clutter or MTS data.

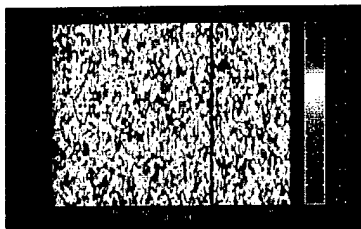


**Figure 3-29. RDI, Wide-Bistatic Angle Acquisition #93 (Angle Index 80)**

The flight path for flight #9 shown in Figure 3-3d indicates that around acquisition #90, the azimuth of the LOS to the MTS is about  $270^\circ$ , i.e., the LOS is almost normal to the antenna. This would indicate that the MTS was clearly visible to the MCARM antenna. The geometry also shows that the antenna is not being directly illuminated by the TARS' main beam when it is passing over the MTS and hence radiating. Thus, conceivably, it was not being saturated by the direct TARS radiation.

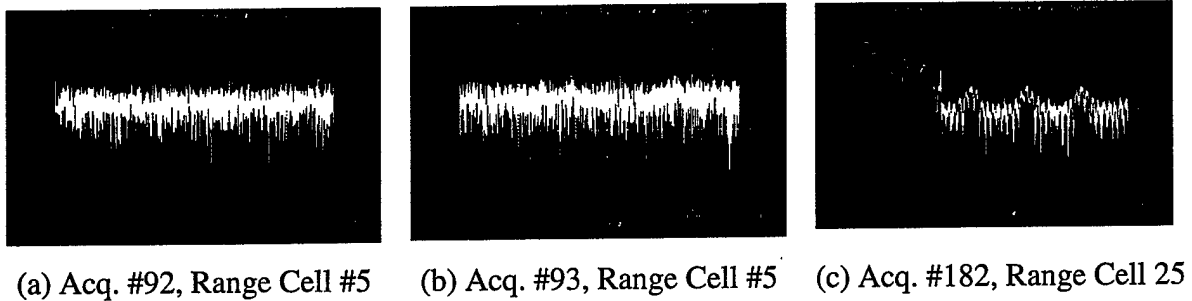
Referring to the flight path shown in Figure 3-2, it is seen that the acquisitions around #90 present a large bistatic angle and this is verified by the plot of the bistatic angle shown in Figure 3-4c. Unfortunately, not all the acquisitions near this region have been reduced and made available in a MATLAB format. We could not, therefore, test other large bistatic angle acquisitions.

Figure 3-30 plots the signal strength versus pulse number for acquisitions #92 and #93, along with that of #182 for a comparison. For the first 2 acquisitions, we have arbitrarily chosen the range cell #5, since there was no indication of any particular cell containing the MTS or any other target.

For acquisition #182, we have chosen cell #48, since this cell clearly contains the MTS signal (see Figure 3-16h). During this acquisition, the TARS radar was on for the first 700 or so pulses, after which it was turned off. During the remainder of the acquisition, only the MTS was on and hence only the MTS signal was recorded. Notice that the clutter return varies between 40-50 dB, while the MTS signal varies between 15-30 dB. Since the beating structure of the multi-tone MTS signal is clearly visible, we can easily conclude that the receiver noise is well below the MTS signal level, possibly at the 10 dB level.

Now, considering the signal plots for the acquisitions #9-92 and #9-93 in Figure 3-30, it appears that throughout these acquisitions, the recorded signal is at a level of about 10 dB (possibly dB<sub>μw</sub>, but the actual unit is not critical for this discussion), with no indication of either a strong clutter return or the characteristic structure of the MTS signals. Clearly, what is displayed is only the receiver noise. It is possible that the initiations of the recording were delayed too long and thus the TARS on-times were missed completely, but then it is not clear how the MTS signal was missed, since it is supposed to have been in a continuous free-

running mode. In any case, these 2 acquisitions did not contain any signals of interest. Since there were not many wide-bistatic angle acquisitions available in the reduced (MATLAB) format, we were unable to determine the effects of the wide bistatic angles on clutter returns and on the signal processing.



**Figure 3-30. Comparing Signal Strength Versus Pulse Number  
in Acquisitions 92, 93 and 182**

## Section 4

### Summary

A major problem faced by airborne radars when looking for low and slow-flying, low-cross-section, airborne targets and slow-moving ground targets is the severe ground clutter and possibly jamming that mask these target returns. The Space-Time Adaptive Processing (STAP) algorithms are a class of adaptive algorithms that make use of the 'space' and the 'time' dimensions simultaneously to largely cancel the clutter without completely canceling the desired signal. Researchers have developed many variations of STAP algorithms and have verified their performance using mainly synthetic data [2, 3, 6, 7, 8, 9, 11].

In 1995-96, the Air Force Research Laboratory, Rome Research Site (AFRL RRS, formerly the Rome Laboratory) collected a large amount of multi-channel, airborne radar measurement (MCARM) data, in both the monostatic and bistatic modes. The purpose was to provide measured data to researchers developing STAP algorithms and also to learn about the nature of monostatic and bistatic clutter. There were a total of 18 data collection flights, 4 of them being for bistatic data, with the rest being for monostatic data. There are literally hundreds of coherent processing intervals (CPI) or acquisitions, with most of them containing a signal from a ground-based, stationary moving target simulator (MTS) that generated multiple tones to represent targets moving at different velocities. On flight #5, a cooperative target aircraft, a Sabreliner, was flown such that the MCARM radar illuminated it and, hopefully, the skin return from this target was recorded on many acquisitions. On several other flights, other targets of opportunity appear.

With a full access to the MCARM database at the AFRL Rome Research Site, this author has attempted to take a comprehensive look at both the monostatic and bistatic clutter data, in an attempt to learn what information the measured data contains. This report is a documentation of that effort.

The MCARM data was collected using a 1 MHz pulse waveform, either chirped or unmodulated. In the former case, pulse compression has to be accomplished as a part of the signal processing. In all cases, the data has been oversampled by a factor of 4; this oversampling is eliminated prior to signal processing. Data was also collected at several PRFs. For example, the monostatic data on flight #5 was collected at a medium PRF of 1,984 Hz using chirp waveforms while the bistatic data on flight #9 was collected at 23,148 Hz using unmodulated pulsed waveform. Of the hundreds of acquisitions recorded on magnetic tapes, several hundred have been reduced to data-cube formats in MATLAB to form the MCARM database at RRS. Due to the limited amount of time and money available for this effort, we have been able to analyze only a limited number of acquisitions.

From the monostatic flight #5, we have analyzed acquisitions #152 and #575. On acquisition #5-152, the MTS signal was partly visible even without any adaptive processing and we have experimented with FTS, EFA and JDL algorithms to determine which of these produce the best clutter suppression and concluded that the FTS seems to perform the best in this particular case. It appears that the FTS algorithm using all 22 channels with a 200-cell support and 6 guard cells produces the best results, the 'best' being judged visually. Previous results relating to this acquisition have been reported by other authors in [4, 12].

Acquisition #5-575 was one of the acquisitions of great interest and much analysis by several investigators because this acquisition, among several hundred others, was supposed to include skin returns from a real, cooperative target, namely the Sabreliner. The location and the velocity of the Sabreliner has been recorded and, thus, its distance, i.e., the range cell, and its Doppler with respect to the BAC 1-11 are easily computed. And yet, we could not see it in the MCARM data, with or without STAP. We also looked at two more acquisitions (not discussed in this report) that were supposed to include the returns from the Sabreliner but were unable to find the target. During these acquisitions the target was at a distance of about 57 nm from the MCARM radar. During the latter part of the flight, i.e., acquisition #850 and beyond, the distance starts to reduce to about 9 nm. Unfortunately, these acquisitions were not available for STAP processing. It would be worthwhile to reduce these acquisitions to the MATLAB format at the earliest opportunity to see if the Sabreliner can be found at least at those close ranges.

From the bistatic flight #9, we have analyzed several acquisitions. Acquisition #9-110, at a bistatic angle of about  $70^\circ$ , was an especially useful CPI to work with since during part of this acquisition, the TARS radar was off, leaving only the MTS signal to be recorded. This allows one to first study the MTS signal in the absence of any clutter and then add different amounts of clutter by including more of the pulses containing clutter. The high PRF bistatic CPIs from flight #9 have only 54 range cells and thus allow only a few STAP algorithms that can work with fewer than 54 support cells. We were able to apply the FTS and JDL algorithms to this acquisition. It was observed that the JDL  $4 \times 1$  (4 degrees of freedom in the Doppler space and only one degree of freedom in the beam space) gives the best performance for this CPI in terms of clutter suppression and clarity of the individual MTS tones.

The acquisition #9-133 was at a bistatic angle of about  $50^\circ$ . Unlike the acquisition #9-110, the TARS was on during the whole duration of the CPI. This prevented a determination of the range cell containing the MTS tones by plotting the signal strength versus the pulse # for any of the cells. Further, the folded-over clutter completely covered the offset tone of the MTS; this prevented the location of the MTS cell in the RDI plot. Neither the FTS nor the JDL algorithm was able to reveal the MTS tone-cluster or the offset tone. Since this acquisition was close enough to the acquisition #9-110, we may assume that in this acquisition, the clutter power level was about 20 dB higher than MTS signal level, as it was

in #9-110. Further, since the TARS was on the whole time, the effective CSR was of the same order. It then appears that when the CSR is about 20 dB or higher, the FTS or JDL are unable to suppress the clutter without destroying the signal too. Much of these results have been reported in references [5, 13, 14, 15, 16].

The bistatic angles were very small for the acquisitions #172-182 on flight 9. These are the so-called pseudo-monostatic acquisitions. All of these acquisitions contained the MTS signal as is indicated by the offset tone appearing in all the RDIs. These acquisitions also seem to contain a return from a large moving object. That it was moving is indicated by the fact that it appeared in a Doppler bin quite distinct from the clutter return.

The TARS was on during the whole duration of acquisition #172 and consequently the effective CSR was probably of the order of 20 dB or more. Neither the FTS nor the JDL algorithm was able to reveal the MTS tone cluster, which is buried in the mainlobe clutter return. For acquisition #9-180, the TARS was on for only a part of the duration of the CPI and in this case the JDL was able to reveal all the MTS tones as well as the other moving target up to an effective CSR of about 15 dB. This is also true of #9-182, but in this case the large moving object observed in #9-180 was not quite apparent. Some of these results have been reported in [17].

The bistatic angles for acquisitions around #90 on flight #9 were close to  $180^\circ$  and these comprise the large bistatic angle acquisitions. It is of great interest to study the bistatic clutter phenomenon at these very large bistatic angles. Unfortunately, not many of the acquisitions in this region have been reduced to the MATLAB format and therefore were available for our analysis. Further, the two acquisitions, #9-92 and #9-93, that were available, seemed to have recorded only receiver noise. It is not clear why they failed to record any clutter return or the MTS signals.

As a continuation of this effort, it would be desirable to reduce some more of the monostatic acquisitions from flight #5 where the cooperative airborne target, the Sabreliner, is at much closer ranges to the MCARM aircraft and then try to find the target in the data. Similarly, more of the bistatic acquisitions around #9-90 should be reduced so that the bistatic clutter phenomenon at large bistatic angles can be more extensively studied.

The monostatic data from flight #5 is at a medium PRF and has a moderate range foldover but almost no Doppler foldover. The bistatic data from flight #9 is at a very high PRF and has more range foldover but no Doppler foldover at all. The data from flight #10 is at a very low PRF, resulting in no range foldover but a significant amount of Doppler foldover. So far, we have not had the opportunity to study this data extensively or apply STAP to it. During the continuation of this effort, attempt will be made to process this data to determine if highly Doppler aliased data presents any peculiarities as far as STAP processing is concerned.



## List of References

1. D. Sloper, D. Fenner, J. Arntz, and E. Fogle, "Multi-Channel Airborne Radar Measurement (MCARM), Bistatic MCARM Flight Test", RL-TR-96-49, Vol II (of four), Final Technical Report, April 1996.
2. J. Ward, "Space-Time Adaptive Processing for Airborne Radar", MIT Lincoln Laboratory Technical Report ESC-TR-94-109, 13 December 1994.
3. H. Wang and L. Cai, "On Adaptive Spatial-temporal Processing for Airborne Surveillance Radar Systems," IEEE Trans. AES Vol. 30, no 3, pp 660-670, July 1994.
4. W. L. Melvin, and M. C. Wicks, "Improving Practical Space-Time Adaptive Radar," Proceedings of the 1997 IEEE National Radar Conference, Syracuse NY, May 1997.
5. P. K. Sanyal, W. L. Melvin, and M. C. Wicks, "Space-Time Adaptive Processing for Advanced Airborne Surveillance (AAS) Bistatic Radar", 43rd Tri-Service Radar Symposium, Boulder, CO, June 1997.
6. A. G. Jaffer, M. H. Baker, W. P. Balance and J. R. Staub, "Adaptive Space-Time Processing Techniques for Airborne Radars", RL-TR-91-162, July 1991
7. R. C. DiPietro, "Extended Factored Space-Time Processing for Airborne Radar", Proc. 26<sup>th</sup> Asilomar Conference, Pacific Grove, CA, pp. 425-430, October 1992.
8. R. S. Blum, et al., "An Analysis of Adaptive DPCA", Proc. IEEE Natl. Radar Conference, Ann Arbor, MI, pp. 303-308, May 1996
9. M. Haimovich, "The Eigencanceler: Adaptive Radar by Eigen-analysis Methods", IEEE Trans. AES, Vol. 32, no. 2, pp. 660-670, April 1996.
10. J. S. Goldstein and I. S. Reed, "Subspace Selection for Partially Adaptive Sensor Array Processing", IEEE Trans. AES, Vol. 33, no. 33, pp. 539-544, April 1997.
11. M. Rangaswamy and J. H. Michels, "A Parametric Multi-Channel Detection Algorithm for Correlated Non-Gaussian Random Processes", IEEE Natl. Radar Conference, Syracuse, NY, May 1997.
12. W. L. Melvin, and B. Himed, "Comparative Analysis of Space-Time Adaptive Algorithms With Measured Airborne Data", presented at the 7th International Conference on Signal Processing Applications & Technology, October 7-10, 1996.
13. P. K. Sanyal, W. L. Melvin, and M. C. Wicks, "Space-Time Adaptive Processing for Advanced Airborne Surveillance (AAS) Bistatic Radar", 43<sup>rd</sup> Tri-Service Radar Symposium, Boulder, CO, June 1997.
14. P. K. Sanyal, "Application of Space-Time Adaptive Processing to MCARM Bistatic Data", MITRE Technical Report, MTR 97B0000068, September 1997.
15. P. K. Sanyal, R. D. Brown, M. O. Little, R. A. Schneible, M. C. Wicks, "Space-Time Adaptive Processing Bistatic Airborne Radar", IEEE Radar Conference, April 1999.

16. R. D. Brown, M. O. Little, R. A. Schneible, M. C. Wicks, P. K. Sanyal, "Application of Space-Time Adaptive Processing (STAP) in Airborne Bistatic Scenarios", Fifth International Conference on Radar Systems, Radar'99, Brest, France, May, 1999.
17. M. O. Little, R. A. Schneible, M. C. Wicks, R. D. Brown, P. K. Sanyal, "The Advanced Airborne Surveillance (AAS) Bistatic Radar and STAP Algorithms for Suppressing Bistatic Clutter", 45th Annual Tri-Service Radar Symposium, Monterey, CA, June, 1999.
18. MATLAB Reference Guide, The Math Works Inc., Natick, MA, 1995.

## Appendix A

# STAP Algorithms

This report contains results of analyzing MCARM data using three STAP algorithms, namely, Factored Time Space (FTS), Extended Factored Approach (EFA), and Joint Domain Localized (JDL). We shall very briefly describe the mechanics of these algorithms without extensive mathematical backgrounds. The reader should consult the listed references for the details.

### A.1 The FTS Algorithm

FTS algorithm is described in the excellent reference on STAP algorithms [1]. The FTS algorithm is not a true 'Space-Time Adaptive' algorithm since the adaptivity is applied only in the element or space domain; no adaptivity is applied to the time domain. Nonetheless, it is traditionally included among STAP algorithms.

For the FTS algorithm, the data was first transformed to the frequency domain. For the monostatic data acquired at a medium PRF of 1,984 Hz, all the Doppler bins were retained. For the bistatic data from flight #9, which was acquired at the high PRF of 23,143 Hz, only the Doppler bins between -800 and +200 Hz were retained, since all the MTS tones lie within this range. This allows us to eliminate more than 95 per cent of the data (only 1,000 Hz out of more than 23 kHz is retained) and unnecessary computation is avoided. Next, adaptivity is applied to the data in the element space.

Now, a frequency-element domain test vector  $X_{k,m}$  for range cell  $k$ , Doppler  $m$  is formed in this fashion:

$$X_{k,m} = [x_{k,m,j}]_{j=1}^{j=n}, \quad n = 11 \text{ or } 22 \text{ for one or two rows} \quad (1)$$

where  $x_{k,m,j}$  is the data sample from the  $k^{\text{th}}$  range cell,  $m^{\text{th}}$  Doppler bin and  $j^{\text{th}}$  element or receiver channel. The expanded form of the vector is given below:

$$X_{k,m} = [x_{k,m,1}, x_{k,m,2}, x_{k,m,3}, \dots, x_{k,m,n}]^T, \quad n = 11 \text{ or } 22 \text{ for 1 or 2 rows} \quad (2)$$

Next,  $N_t$  training data vectors are formed in the same manner as above but from the  $N_t$  range cells surrounding the test cell, excluding the desired number of guard cells on either side of the test vector. When possible, half of the  $N_t$  cells chosen are below (in range) the test

cell and the remaining half above. When nearing the end of the range window, consisting of 630 cells in the monostatic CPIs and 54 range cells in the bistatic CPIs, this division is altered to select as many as possible from the limiting end, with the rest being selected from the remaining data. The average of the outer-product of these training vectors is the sample covariance matrix,  $\hat{R}_{k,m}$ , for the current range cell k and Doppler bin m, i.e.,

$$\hat{R}_{k,m} = \frac{1}{N_t} \sum_{i=1}^{N_t} X_{i,m} X_{i,m}^H \quad i \neq k \text{ or the guard cells} \quad (3)$$

The matrix is of dimension nxn where n is the number of channels, and requires that  $N_t > 2n$  for a reasonable estimate of the covariance matrix.

The adapted signal value  $y_{k,m,l}$  at the test range cell k, test Doppler cell m and a desired test look angle l is then obtained as:

$$y_{k,m,l} = s_l^H \hat{R}_{k,m}^{-1} X_{k,m} \quad (4)$$

where  $s_l$  is the steering vector corresponding to the look angle l and is obtained from the table of measured steering vectors provided by Westinghouse [1]. This is a 11x1 or a 22x1 vector, depending on whether we have used only 1 or both rows of the antenna.

What we plot is the normalized value:

$$\bar{y}_{k,m,l} = \frac{(abs(s_l^H \hat{R}_{k,m}^{-1} X_{k,m}))^2}{s_l^H \hat{R}_{k,m}^{-1} s_l} \quad (5)$$

## A.2 The EFA Algorithm

The EFA algorithm, as the name implies, is an extended version of the FTS algorithm. The extension is provided by considering more than a single Doppler bin and, as such, it results in a true 'Space-Time' algorithm in the element-Doppler space. The results shown in

this report uses the 2<sup>nd</sup> order EFA algorithm. The 2<sup>nd</sup> order EFA algorithm considers 3 Doppler bins.

The 2<sup>nd</sup> order EFA test vector in the frequency-element domain for range cell k, Doppler m and element n is formed in this fashion:

$$X_{EFA,k,m,n} = \left[ x_{k,i,j} \right]_{j=n}^{j=1} \Bigg|_{i=m+1}^{i=m-1} \quad (6)$$

where n is the number of channels used (either 11 or 22). The expanded form of the test vector is as follows:

$$X_{EFA,k,m} = \left[ \begin{array}{c} x_{k,m-1,1}, x_{k,m-1,2}, x_{k,m-1,3}, \dots, x_{k,m-1,n}, x_{k,m,1}, x_{k,m,2}, x_{k,m,3}, \dots, \\ x_{k,m,n}, x_{k,m+1,1}, x_{k,m+1,2}, x_{k,m+1,3}, \dots, x_{k,m+1,n} \end{array} \right]^T \quad (7)$$

The sample covariance matrix,  $\hat{R}_{EFA,k,m}$ , for the current range cell k and Doppler bin m, is computed as before using the equation:

$$\hat{R}_{EFA,k,m} = \frac{1}{N_t} \sum_{i=1}^{N_t} X_{EFA,i,m} X_{EFA,i,m}^H \quad i \neq k \text{ or the guard cells} \quad (8)$$

The matrix is of dimension  $3n \times 3n$ , where n is the number of channels used, and requires that  $N_t > 6n$  for a reasonable estimate of the covariance matrix.

For the desired look angle, the 2<sup>nd</sup> order EFA steering vector is formulated using the MATLAB 'kron' function [18] as follows:

$$\begin{aligned} s_{EFA,i} &= \text{kron}([0,1,0], s_i) \\ &= \begin{bmatrix} n - \text{dimension zero vector} \\ s_i \text{ (n - dimension vector)} \\ n - \text{dimension zero vector} \end{bmatrix} \end{aligned} \quad (9)$$

where  $s_{EFA,i}$  is a  $3n \times 1$  vector.

The adapted signal value  $y_{EFA,k,m,l}$  at the test range cell k, test Doppler cell m and a desired test look angle l is then obtained as:

$$y_{EFA,k,m,l} = s_{EFA,l}^H \hat{R}_{EFA,k,m}^{-1} X_{EFA,k,m} \quad (10)$$

Again as before, what we have plotted is the normalized value of this adapted signal:

$$\bar{y}_{EFA,k,m,l} = \frac{(abs(s_{EFA,l}^H \hat{R}_{EFA,k,m}^{-1} X_{EFA,k,m}))^2}{s_{EFA,l}^H \hat{R}_{EFA,k,m}^{-1} s_{EFA,l}} \quad (11)$$

### A.3 TheJDL mxn Algorithm

The JDL algorithm is a frequency-beam domain algorithm [3]. Therefore, besides transforming the data to the frequency domain as in the FTS and EFA algorithms, we now also transform the data into the beam space using all the measured spatial steering vectors provided by Westinghouse [1].

In the frequency-beam domain, let the target cell be at range k, frequency m' and look direction n'. Note that we had used n to denote the element number; here n' is used to denote the look direction. Let the number of Doppler bins, m, be the sum:

$$m = m_1 + 1 + m_2 \quad (12)$$

where  $m_1$  is the number of Doppler bins ahead of the target Doppler bin m' and  $m_2$  is the number of Doppler bins following the target Doppler bin m' that we want to include in the test vector formulation. Either or both of  $m_1$  and  $m_2$  can be zero.

Similarly, Let the number of look directions, n, be the sum:

$$n = n_1 + 1 + n_2 \quad (13)$$

where  $n_1$  is the number of look directions ahead of the target look direction n' and  $n_2$  is the number of look directions following the target look direction n' that we want to include in the test vector formulation. Either or both of  $n_1$  and  $n_2$  can be zero.

The JDL\_mxn test vector in the frequency-element domain for range cell k, Doppler m' and look direction n' is a mxn1 dimensioned vector and is formed in this fashion:

$$X_{JDL,k,m',n'} = \left[ x_{k,i,j} \right]_{\substack{j=n'-n_1 \\ j=n'+n_2}}^{j=m'-m_1} \quad (14)$$

Note that the test vector is not only a function of m and n but also a function of m<sub>1</sub>, m<sub>2</sub>, n<sub>1</sub>, and n<sub>2</sub>. As such, the subscript on the vector should spell out the values of m<sub>1</sub>, m<sub>2</sub>, n<sub>1</sub>, and n<sub>2</sub>. But for the sake of conserving subscripts, we have not specifically included them in the subscript list here. However, when formulating the vector, this dependence should be kept in mind.

The sample covariance matrix,  $\hat{R}_{JDL,k,m',n'}$ , for the current range cell k, Doppler bin m' and look direction n' is computed as before using Equation 14. The matrix is of dimension mxmxmn and requires that  $N_t > 2mn$  for a reasonable estimate of the covariance matrix.

$$\hat{R}_{JDL,k,m',n'} = \frac{1}{N_t} \sum_{i=1}^{N_t} X_{JDL,i,m',n'} X_{JDL,i,m',n'}^H \quad i \neq k \text{ or the guard cells} \quad (15)$$

The JDL\_mxn steering vector has the form:

$$s_{JDL\_mxn} = \text{kron}([m_1 \text{ zeros}, 1, m_2 \text{ zeros}], [n_1 \text{ zeros}, 1, n_2 \text{ zeros}]) \quad (16)$$

Note that the vector is not only a function of m and n but also a function of m<sub>1</sub>, m<sub>2</sub>, n<sub>1</sub> and n<sub>2</sub>. As such, the steering vector subscripts should include these specific values. But while being mindful of this dependence, we have, as with the test vector, left these specific subscripts out to reduce subscript clutter. For example, if m = 4 with m<sub>1</sub> = 2, m<sub>2</sub> = 1, and n = 3 with n<sub>1</sub> = 1, n<sub>2</sub> = 1, then using Equation 16, the 12x1 steering vector is as follows:

$$\begin{aligned} s_{JDL\_mxn} &= \text{kron}([0,0,1,0],[0,1,0]) \\ &= [0,0,0,0,0,0,1,0,0,0,0] \end{aligned} \quad (17)$$

On the other hand, if  $m=4$  with  $m_1 = 1$ ,  $m_2 = 2$ , and  $n = 3$  with  $n_1 = 2$   $n_2 = 0$ , then using Equation 16, the  $12 \times 1$  steering vector is as follows:

$$\begin{aligned} s_{JDL\_mxn} &= \text{kron}([0,1,0,0],[0,0,1]) \\ &= [0,0,0,0,0,1,0,0,0,0,0,0] \end{aligned} \quad (18)$$

The significance of this steering vector is clear from the following expression:

$$s_{JDL\_4 \times 3}^H X_{JDL,k,m',n'} = x_{k,m',n'} \quad (19)$$

i.e., the unadapted steering vector simply points to the target cell.

The adapted signal value  $y_{JDL,k,m',n'}$  at the test range cell  $k$ , test Doppler cell  $m'$  and a desired test look angle  $n'$  is then obtained as:

$$y_{JDL,k,m',n'} = s_{JDL\_mxn}^H \hat{R}_{JDL\_mxn,k,m',n'}^{-1} X_{JDL\_mxn,k,m',n'} \quad (20)$$

The normalized value used for the plots is calculated as follows:

$$\bar{y}_{JDL,k,m',n'} = \frac{(\text{abs}(y_{JDL,k,m',n'}))^2}{s_{JDL\_mxn}^H \hat{R}_{JDL\_mxn,k,m',n'}^{-1} s_{JDL\_mxn}} \quad (21)$$



## **Distribution List**

### **Internal**

**D010**

E. A. Palo

**D200**

B. A. Deresh

**D400**

W. E. Seivers

**D620**

A. S. Margulies

**D700**

R. T. Carroll

B. A. Deresh

R. L. Fante

J. D. R. Kramer

T. B. Shields

**D710**

B. N. Suresh Babu

R. M. Davis

P. K. Sanyal (5)

N. M. Tomljanovich

L. W. Yoder

**D720**

T. Guella

D. M. Zasada

**D730**

R. C. Pietro

R. P. Perry

L. D. Tromp

**D830**

E. K. Dunn (5)

**R103**

Corporate Library (3)

**Project**

Rome Laboratory

26 Electronic Parkway

Rome, NY 13441-4514

**RL/SNRD**

M. O. Little

**RL/SNRT**

W. J. Baldygo

R. D. Brown

G. J. Genello

J. H. Michels

M. C. Wicks